K^0_s, Λ, and $\bar{\Lambda}$ p_T spectra in pp collisions at $\sqrt{s} = 7$ TeV, measured with the ALICE experiment at LHC

Tuva Richert

August 28, 2011

Abstract

This thesis presents a study of Λ, $\bar{\Lambda}$, and K^0_s particle (generically referred to as V^0 particles) production measured by the ALICE experiment located at LHC, CERN, in proton-proton collisions at a center of mass collision energy of $\sqrt{s} = 7$ TeV. The particles are reconstructed via their V^0 decay topology, which can be done due to the excellent tracking performance of the Time Projection Chamber detector. The V^0 invariant yields, as well as the p_T dependence of the Λ/K^0_s and $\bar{\Lambda}/\Lambda$ ratios, are produced and analyzed. In addition to being one of the first measurements of these particles in pp collisions at this energy, the results are important as a reference for studies of lead-lead collisions, where the yield and ratio dependencies of transverse momentum are expected to change due to a recombination mechanism during the hadronization of the new quark matter state created in heavy ion collisions: the quark gluon plasma.

LUNDS UNIVERSITET

Populärvetenskaplig sammanfattning

Big Bang, *Den Stora Smällen*, är ett begrepp som de flesta av oss känner till; universums födelse som har gett upphov till galaxer, svarta hål, solsystem, planeter – och ja, indirekt till livet och mänskligheten själv. Långt innan allt detta skapades, bara några bråkdelar av en sekund efter Big Bang, fanns inte den vanliga materien som vi är vana vid idag; det fanns inte ens atomer eftersom det inte fanns några protoner och neutroner som kunde bygga upp en atomkärna. Precis efter Big Bang hade universum en enormt hög temperatur, och det var inte förrän universum hade svalnat av som materia kunde bildas.

Men någonting fanns. Vi tror att det under universums tidiga epok – innan materia bildades – existerade *kvark-gluon-plasma* (QGP). Detta är ett tillstånd i vilket hadroners (en typ av partiklar som består av kvarkar, t.ex. protoner och neutroner) inre beståndsdelar – kvarkar och gluoner – kan röra sig fritt, vilket är omöjligt under normala förhållanden, d.v.s. när temperaturen och partikeldensiteten är låg, eftersom den starka kraften som bärs av gluonerna – som påverkar både kvarkarna och gluonerna själva – ökar när partiklarna kommer längre ifrån varandra (i motsatts till den elektromagnetiska eller gravitionella kraften som minskar med ökat avstånd), och minskar alltså när partiklarna är väldigt nära. Detta faktum betyder att kvarkar och gluoner binds samman och bildar partiklar, och om någon omständighet skulle göra att kvarkarna inom en partikel skulle separeras, så ser den starka kraften till att den energi som går åt till att separera kvarkarna istället används till att bilda kvarkar och anti-kvarkar som den separerade kvarken kan bindas till. Alltså, under normala förhållanden kan kvarkar och gluoner aldrig vara fria partiklar.

Med hjälp av kollisioner mellan hadroner kan man dock ändra dessa *normala* förhållanden. Genom att accelerera tunga kärnor till en fart nära ljusets, och sedan kollidera två strålar av sådana partiklar, kan väldigt höga temperaturer (liknande dem vid universums skapelse) och partikel-densiteter bildas. Vid en sådan kollision genomgår vanlig materia en fasövergång till ett tillstånd där kvarkar och gluoner *kan* anses fria eftersom den starka kraften upplevs bli väldigt svag och näst intill slutar verka när kvarkarna och gluonerna befinner sig så nära varandra (kollisionen pressar ihop materien i en mycket liten volym så att partikel-densiteten ökar). Detta är kvark-gluon-plasma.

För att ta reda på *om* QGP har bildats i kollisionen måste man veta vilka partiklar som har skapats av den energi som blir tillgänglig när QGP:n svalnar av och upphör att existera. Vi tror nämligen att det bildas olika mängder av vissa sorters partiklar då plasma har bildats, jämfört med om den inte skulle ha bildats. Detta beror på att det väntas vara olika mängder av olika sorters kvarkar, vilka kombineras ihop till andra partiklar än de som normalt formas. Informationen från kollisioner där QGP inte väntas bildas är mycket viktig eftersom det används som referensdata som andra kollisioner jämförs med.

Med "de som normalt formas" menas här de partiklar som bildas i kollisioner där QGP inte förväntas bildas, t.ex. i kollisioner mellan protoner (som är mycket lättare, och har färre beståndsdelar, jämfört med tunga kärnor). Det är detta som mitt arbete går ut på: att analysera data från högenergetiska proton-proton-kollisioner vid ALICE-experimentet (A Large Ion Collider Experiment) som är placerat vid partikelfysik-labbet CERN, Schweiz, där acceleratorn LHC (Large Hadron Collider) finns. Analysen innebär att – på ett tämligen avancerat sätt – identifiera och bestämma antalet Λ, $\bar{\Lambda}$ och K^0_s som har bildats vid kollisioner och se hur det antalet förändras med partiklarnas rörelsemängd, vilket är viktigt att veta när man sedan ska analysera samma sak från kollisioner då QGP har bildats.

Acknowledgments

I would like to thank my supervisors Peter Christiansen and Anders Oskarsson for being the perfect combination of supervisors; Peter with his great knowledge in programming and Anders with his ability to explain general concepts and detector related technicalities. I thank both for their excellent analyses ideas, help, and support.

Of course, I thank the rest of the Lund ALICE team Evert Stenlund, and previous members Philippe Gros, Alexandru Dobrin, and Lene Bryngemark for sharing their knowledge and helping me a lot. From those in Lund I also thank Bozena Wlosinska for her very helpful administrative work, and for contributing to the very pleasant atmosphere in Lund Experimental High Energy Physics department.

Also, many thanks goes to the ALICE collaboration and the TPC group, especially Antoine Junique and Christian Lippmann who made it possible for me to experience the work on the TPC in the ALICE cavern. This work is for me one of the most exciting things one can possibly do, and one year ago I couldn't even dream about going down there to actually perform important work. I thank them for having me as their colleague, and for trusting me with the responsibility.

Peace and love!
Tuva

Contents

Chapter 1

Introduction

1.1 The aim of the study

In this project data from the ALICE experiment, located at the Large Hadron Collider (LHC) at CERN, is analyzed – especially data from the Time Projection Chamber (TPC) detector, which is one of the central detectors in ALICE. The aim of the analysis is to identify particles which are created in the collision of two high energy proton beams.

The main analysis is to identify Λ, $\bar{\Lambda}$, and K_s^0 particles (with a common name V^0 particle due do the fact that the particle itself is neutral, leaving only a V-shape in the detector from the charged decay particle tracks) which are produced in proton-proton (pp) collision and mainly decays to protons and pions with the following branching ratios, expressing the probability of decaying into these specific charged channels:

$$\Lambda \rightarrow p + \pi^- \text{ BR: } 63.9\% \tag{1.1}$$

$$\bar{\Lambda} \rightarrow \bar{p} + \pi^+ \text{ BR: } 63.9\% \tag{1.2}$$

$$K_s^0 \rightarrow \pi^+ + \pi^- \text{ BR: } 68.6\% \tag{1.3}$$

The results are presented as transverse momentum (p_T) spectra, which indicates how many particles per p_T and rapidity, y, that are produced in a collision, called the *transverse yield*. Transverse momentum spectra of produced particles are the most straightforward way to present new results from a reaction like pp collisions at $\sqrt{s} = 7$ TeV, analyzed here. It is also a very important base line and reference for lead-lead (PbPb) collision data analysis, where the quark matter *Quark Gluon Plasma* (QGP) is thought to be created, and is expected to modify the particle ratios in the hadronization process when the QGP is cooled down – releasing energy to produce particles.

This analysis is driven to answer the following questions:

- How do the V^0 particles – the Λ, $\bar{\Lambda}$, and K_s^0 – spectra look like for proton-proton (pp) collisions at a center of mass energy $\sqrt{s} = 7$ TeV?
- What is the baryon/meson ratio, $\frac{\Lambda}{K_s^0}$ and $\frac{\Lambda+\bar{\Lambda}}{2K_s^0}$, for pp collisions at $\sqrt{s} = 7$ TeV?
- What is the antiparticle/particle ratio, $\frac{\bar{\Lambda}}{\Lambda}$, for pp collisions at $\sqrt{s} = 7$ TeV?
- How do the results compare to expectations?

Since these studies require clean V^0 samples, I develop a method to select V^0 particles with small background (where the background contains a mixture of particles). The method mainly involves identification via their decay vertex and an analysis on various cuts of the characteristics of the daughter particles. The results from this analysis can be used to cross check and refine high transverse momentum particle identification of protons, kaons, and

pions, based on energy loss information from the Time Projection Chamber, and is therefore a strong motivation of doing this study, since clean samples of the V^0 daughter particles (protons and pions) can be obtained.

Experimental physics is not only to analyze acquired data. The actual measurement is of course also an important step. Without high quality measurements, the data analysis become difficult and may even be impossible. Thus, the experimental apparatus has to be maintained at a high level of functionality and calibrated at all times. In addition to data analysis, I have served (after proper training and 2 months experience as a summer student in ALICE 2010) as subsystem shifter for the Time Projection Chamber (TPC), on call expert shifter for the Forward Multiplicity Detector (FMD), and I have also been involved in TPC hardware work, discussed in Sec. 5. The final experimental duty I have had was to serve as Data Quality Monitoring shifter.

1.2 The layout of the thesis

The thesis begins with a description of high energy physics in Chapter 2, where the Standard Model of particle physics is introduced, discussing different particles and how they interact. Also in this chapter the experimental view of particle physics is described by briefly discussing accelerators – especially LHC – and the physics one can study at LHC. Definitions which will be useful in the analysis are defined in Sec. 2.3. Chapter 2 then proceeds with describing quark gluon plasma: how it can be studied and the importance of reference measurements, which is one of the results presented in this thesis.

Chapter 3 presents the ALICE experiment and how a particle track is reconstructed followed by a detailed description of the Time Projection Chamber and its analysis features regarding particle identification in Chapter 4. The experimental part of my project – the electronics work done on the ALICE TPC – is then described in Chapter 5.

The analysis of the Λ, $\bar{\Lambda}$, and K^0_s particles is presented in Chapter 6 where I start with a description of the analysis framework and the data and MC samples used for the analysis. Then, in Sec. 6.3, I proceed with a discussion of how clean particle samples are extracted from the data and MC used by introducing the selection criteria and cuts on some of the variables. The actual analysis method is also presented, followed by a detailed MC study where the correction factors and the stability of the analysis method is checked. In Sec. 6.6, the MC is then compared to the real data.

Chapter 7 presents the data results in the form of p_T spectra and invariant yield ratios, and the results are compared with analysis results from both ALICE and other experiments.

There are a number of acronyms in this thesis which are summarized in Appendix 1, where the reader can have a look if they have forgotten the meaning.

Chapter 2

High Energy Physics

2.1 The Standard Model

The Standard Model (SM) in particle physics describes the elementary particles and their interactions. By formulating the Quantum ElectroDynamics (QED), the electromagnetic and weak force, the *electroweak* force, can be described. In the QED theory the electromagnetic interaction between two electrically charged particles is mediated by exchanging virtual photons. For the strongly interacting matter the force is mediated by gluons. Quantum ChromoDynamics (QCD) theory describes the strong force and how it is mediated. The SM can thereby explain three of the four fundamental forces in nature[1].

2.1.1 Fermions

The fundamental particles which the SM describes can be sorted in either fermions or bosons. The fermions are leptons and quarks, with spin 1/2. There are six known quarks, see Fig. 2.1, with different *flavors*, namely the up (u), down (d), charm (c), strange (s), top (t), and bottom/beauty (b). The u, c, and t quark have electric charge $2/3e$ (where e is the charge of the electron), while d, s, and b have charge $-1/3e$.

The leptons are also listed in Fig. 2.1. The charged leptons with charge $-e$ are the electron (e^-), muon (μ^-), and tau (τ^-). The corresponding neutrinos are the electron neutrino (ν_e), muon neutrino (ν_μ), and tau neutrino (ν_τ), which are almost massless. All fermions have an antiparticle which possesses the same properties as the corresponding particle, but opposite quantum numbers (e.g. charge).

In addition to the electrical charge, the quarks also carry color charge (red, green, and blue). Since color charge is a QCD property and electrical charge is a QED property, the quarks can interact through electromagnetic, weak, and strong interactions. The electrically charged leptons can interact electromagnetically and weakly, and the neutral leptons can only interact weakly, but leptons do not interact with the strong interaction.

2.1.2 Hadrons

The QCD theory does not allow quarks to be free due to their color charge; they need to form colorless states called hadrons. To be colorless (or *color singlets*), the hadrons must consist of either three quarks (or three anti-quarks) with the colors blue, green, and red, or a quark-antiquark pair with color and anticolor[2]. The hadron state with a group of three bound quarks is called a baryon (e.g. the proton with the quark content uud), and the state containing a bound quark-antiquark pair is called a meson (e.g. the pion with the quark content $u\bar{d}$). In both the meson and baryon case, the quarks are confined by gluons, which

[1] The fourth force, gravity, is not included in the SM.

[2] blue+green+red=white, and color+anticolor=white, where white is considered to be neutral.

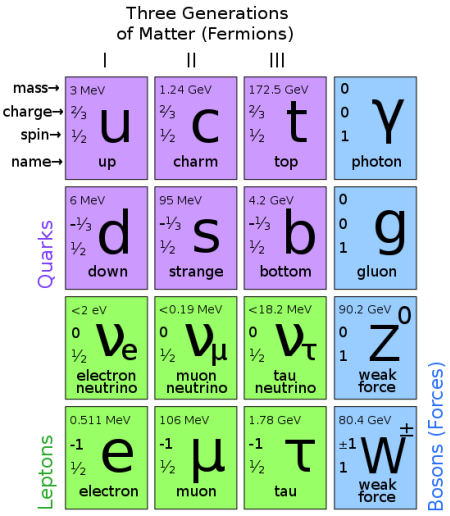

Figure 2.1: The fermions (quarks and leptons) and bosons in the Standard Model of particle physics [20]. There are three *families* of quarks: $\binom{u}{d}$, $\binom{c}{s}$, and $\binom{t}{b}$ (purple), and three families of leptons: $\binom{\nu_e}{e}$, $\binom{\nu_\mu}{\mu}$, and $\binom{\nu_\tau}{\tau}$ (green). The bosons (blue) are the force mediators: the neutral γ for the electromagnetic, the colored g for the strong, and $W^{\pm}$, Z^0 for the weak force. Figure taken from [21].

are bosons. The mass of a hadron is much larger than the bare mass of quarks building up the hadron.

2.1.3 Gauge bosons

The gauge bosons are the particles that mediate the different forces between fermions (listed in Fig. 2.1), by exchange of bosons between the fermions. A boson can be exchanged only if it obeys the uncertainty principle (these are called *virtual* bosons), stating that within a certain time period, Δt (the lifetime of the virtual boson), the exchange particle with (rest) energy $E = mc^2$, where m is the mass of the boson, can exist if

$$\Delta E \Delta t \approx mc^2 \Delta t > \frac{\hbar}{2} \tag{2.1}$$

Since Δt is the lifetime, the range of the force, R_F, carried by this particle can be calculated by

$$R_F \approx c\Delta t \approx \frac{\hbar}{2mc} \tag{2.2}$$

i.e. it is proportional to the inverse mass. Virtual photons mediate the electromagnetic force. These are massless and hence the range of the force is infinite. Three particles mediate the weak force; the $W^{\pm}$ with electrical charge $+e/-e$ and a mass of 80.4 GeV$/c^2$, and the neutral Z^0 with mass 90.2 GeV$/c^2$. Since they are heavy, the range will be relatively small, $\sim 10^{-3}$ fm.

There exist eight gluons which carry the strong force. The gluons are – like the quarks – color charged. This leads to an important property: a gluon can couple to other gluons. The self-coupling property is responsible for the fact that the quarks are confined within hadrons, for their asymptotical freedom, see Sec. 2.4.3, and for the fact that the force has very short range (~ 1 fm) even though it is massless. Unlike the electromagnetic force, which decreases with increasing distance, the strong force decreases at small distances; the strong potential goes like $V(r) \propto 1/r$ and thus the force is proportional to

$$F(r) = \frac{dV}{dr} \propto 1/r^2, \tag{2.3}$$

but it behaves as a linear rise at large distances. This explains the confinement, since the quarks cannot escape the hadron due to the increasing strong force, and it also explains the asymptotic freedom based on the argument that the quarks will be less affected by the strong force at close distances, e.g. in a very dense environment, see Sec. 2.4.3.

2.2 Experimental High Energy Physics

To discover new physics, one must explore the high energy region by colliding particles or nuclei. With high enough energy (TeV scale) these collisions can produce rare (or theoretically predicted) particles or matter states such as the Higgs particle, SUSY particles, or QGP.

To reach energies in the TeV scale, the particles need to be accelerated by multiple passages in the accelerators' varying electric field. This can be done by a circular accelerator (such as LHC) due to the fact that the bunches can circulate many times. For a linear collider, however, the energy reached cannot be as high since the particle bunches pass the electric fields only once.

In a circular collider the particles colliding can not be too light in order not to loose energy in the form of synchrotron radiation. The amount of energy lost, ΔE, by a relativistic particle of mass m is given by [16]:

$$\Delta E \propto \frac{E^4}{\rho m^4} \tag{2.4}$$

where E is the energy of the particle and ρ is the radius of curvature. This means that, for relativistic particles, the energy loss by synchrotron radiation is proportional to $1/m^4$ [16]. So in order to reach the highest energies in a circular collider, the use of heavy particles, like protons, is thereby necessary. The colliding particles has an internal structure in the form of elementary particles which causes one problem: a parton-parton collision will rarely have a *large* fraction of the total energy – making it difficult to distinguish those who *do* have a high energy from the soft collision background. But the choice of a circular heavy particle collider is based on the reachable energy which is necessary to discover new physics.

In a linear collider, energy cannot be lost by synchrotron radiation since the acceleration path of the particles is not curved, hence lighter particles e.g. electrons can be accelerated. These cannot reach as high energy as the circular colliders, but the signals will be cleaner than for heavy particle collisions since electrons are elementary (they do not have an internal structure). These machines are therefore suitable for precision measurements, preferably *after* the new discoveries are done.

2.2.1 Large Hadron Collider

In a circular collider the particles orbiting have a momenta given by the following relation [16]

$$p = 0.2976\rho B \tag{2.5}$$

where p is the particle momentum (in GeV/c), B is the magnitude of the magnetic field (given in Tesla), and ρ is radius of curvature of the particle. This can be understood by formulating the equations of motion (with the Lorentz force perpendicular to the direction of motion, resulting in no work on the particle) [16]:

$$\frac{d\bar{p}}{dt} = e\bar{v} \times \bar{B} \text{ and } \frac{dE}{dt} = 0 \tag{2.6}$$

where $\bar{p}$ is the momentum vector and $\bar{v}$ is the velocity vector of the particle. Since $p = \gamma mv$, the first equation can be written as

$$\gamma m \frac{d\bar{v}}{dt} = e\bar{v} \times \bar{B} \tag{2.7}$$

and since no work on the particle is performed by the force, the magnitude of the velocity, v, and $\gamma(v)$ is constant, reducing Eq. 2.7 to $\gamma mv^2/\rho = evB$ (for a circular orbit), which leads to

$$pc = ec\rho B \text{ Joule } = 4.8 \cdot 10^{11} \rho B \text{ Joule } = 0.2976\rho B \text{ GeV} \tag{2.8}$$

which hence gives the result in Eq. 2.5.

From this equation it is seen that, for the colliding particles to have a high energy (large momentum), the radius of the accelerator needs to be large since the magnetic field strength is limited[3].

The Lage Hadron Collider (LHC) at CERN, Geneva, see Fig. 2.2, can accelerate protons to the current energy of 3.5 TeV per beam. The radius is 4 km, and the circumference is 27 km. The design luminosity is $L = 10^{34}\ cm^{-2}s^{-1}$, which is a measure of how many collisions that can be produced per second[4].

In Fig. 2.2 the indication "Linac" shows where the acceleration process starts. The beam from the linac is injected to the PSB (Proton Synchrotron Booster), where its energy is enhanced. The beam then goes through the PS (Proton Synchrotron) and then into the SPS (Super Proton Synchrotron) where the energy is increased further. Then the beams are injected to LHC.

There are four beam intersection points, where the particle beams collide, at LHC where the ALICE, ATLAS, LHC-b, and CMS experiments are located.

[3] The largest attainable field over a large region is about 10 T [16].

[4] *Integrated* luminosity gives the total number of collisions produced.

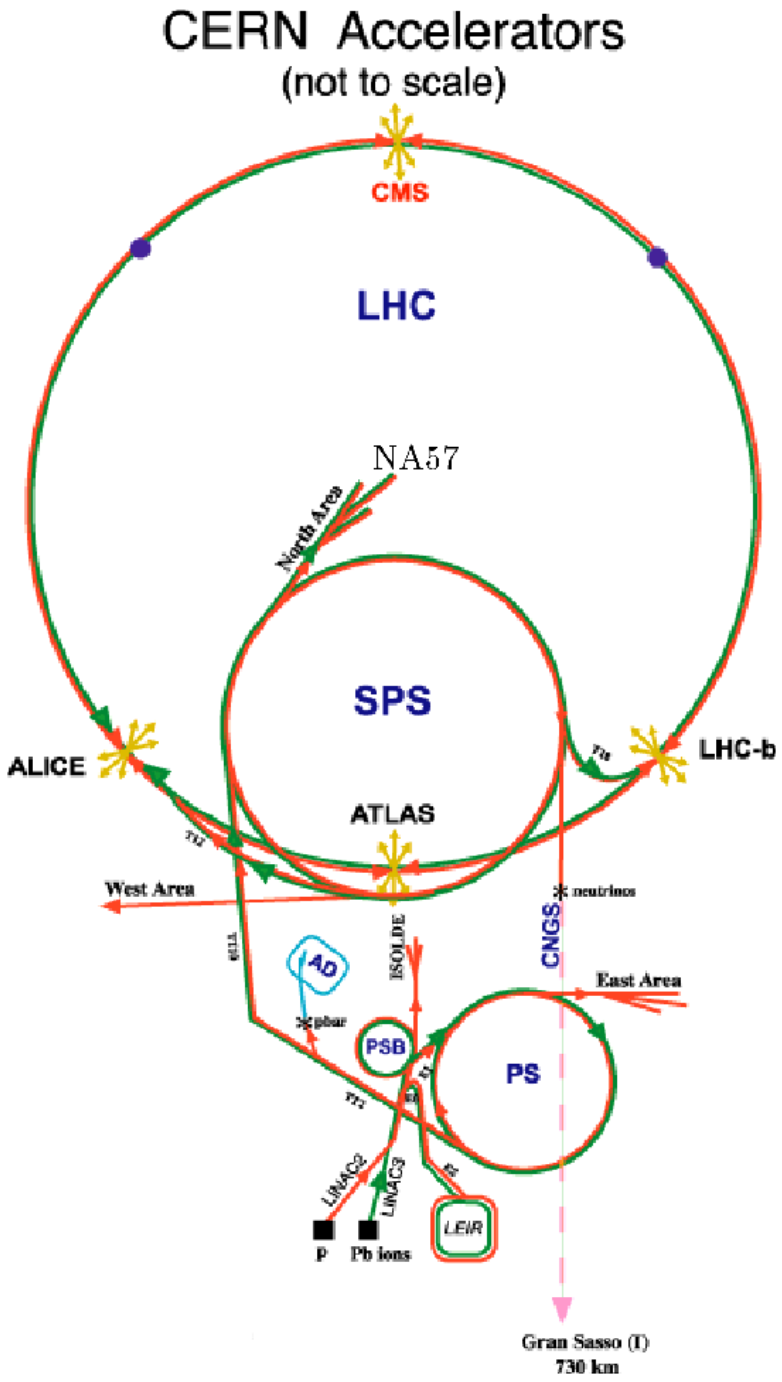

Figure 2.2: A schematic diagram of the CERN accelerators and injectors (not scaled). The acceleration starts at the linacs, are then injected to the PSB, PS, and SPS before the beams reach LHC. LHC can currently reach a center of mass energy of 7 TeV for pp collisions, and for ions it is 2.76 TeV/nucleon. The four experiments ALICE, ATLAS, CMS, and LHC-b are marked with a yellow star, indicating the collision points. Figure taken from [15].

2.2.2 The physics at LHC

The four main experiments at LHC: ATLAS, ALICE, CMS, and LHC-b, are built to study different phenomena arising from particle collisions. The ALICE is the only experiment built for heavy ion physics. The other three study mainly pp collisions with the goal of discovering predicted particles such as: the Higgs particle, which is missing to completely confirm the Standard Model and the fact that some particles have mass; SUSY particles which is a model beyond SM – predicting that every particle in the SM have a heavier SUper SYmmetric particle (which are forming the dark matter in the universe). These are phenomena that require the highest possible energies and luminosities, since the particles are expected to have high masses and therefor suitable for pp collisions.

Since this thesis focuses on analyzing data from the ALICE experiment at CERN, it is important to stress what kind of physics this experiment is built for. ALICE is not suitable for the Higgs search or the search for SUSY particles, but ALICE can – with pp data – confirm the SM at low p_T as a complementary detector to ATLAS and CMS. Another, more important, application for taking pp data with ALICE is to have reference data to compare PbPb results with, since ALICE is dedicated to heavy ions physics, i.e. it is optimized for collisions of heavy ions (AA collisions), namely lead ions.

Before one can draw conclusions from the heavy ion analysis results, it is important to have the reference values to compare with. Simulations and Monte Carlo studies give good reference values and are crucial to have. But also, as mentioned, data from collisions between protons provide good reference data since these processes are relatively well understood, and any deviation is worth studying further. A theory called perturbative Quantum ChromoDynamics (pQCD) describes the hadron production by hard parton-parton scattering (large momentum transfers) – and their fragmentation – at high transverse momenta[5] in high energy pp collisions [5]. Since the QCD model describes pp collisions well, we can use this model to predict scenarios in a collision with more particles involved, such as heavy ion collisions.

The purpose of heavy ion physics is to understand macroscopic phenomena which arise from the microscopic laws of elementary particle physics [4]. This is done by characterizing the properties of very hot and dense nuclear matter which can be created with heavy ion collisions. In such collisions, a huge amount of energy is released and the state of ordinary matter is believed (theories predict) to undergo a phase transformation to a very hot and dense state which is called a quark gluon plasma (QGP), in which the quarks – in comparison with ordinary hadron matter – are considered as free quarks, see Sec. 2.4. It would be a great success to detect signs and evidence that this plasma actually is created in such events, since this would develop existing theories of the state of the early universe on a macroscopic scale.

[5]Soft interactions dominate at low momentum, and can be understood by thermal models [5].

2.3 Definitions

2.3.1 The transverse and longitudinal momentum

In order to continue, some concepts need to be introduced. The first concept is the transverse and longitudinal momentum of a particle, the p_T and p_L. To define p_T and p_L a coordinate system is needed: in ALICE, the z-axis is along the beam direction, and the x-axis is perpendicular to the beam horizontally, see Fig. 3.1(a). p_T and p_L are then defined as follows

$$p_T = \sqrt{p_x^2 + p_y^2} \tag{2.9}$$

and

$$p_L = p_z \tag{2.10}$$

where p_x, p_y, and p_z are the x, y, and z components of the momentum vector.

Both p_T and p_L will be used in the analysis, and particularly p_T since initially the $p_T = 0$, and so the p_T has to be built up in the collision, i.e. this is where the physics is; the incoming kinetic energy is transformed to particles and their p_T. The transverse momentum is boost invariant, i.e. it is the same in all reference systems moving along the z direction.

2.3.2 The invariant mass

Another quantity which will be useful in this analysis is the invariant mass, which, for a particle decay, is defined as [16]

$$m_{V^0} = \sqrt{(E_1 + E_2)^2 - (\vec{p_1} + \vec{p_2})^2} \tag{2.11}$$

where E is the energy and $\vec{p}$ is the momentum of the two daughter particles in the decay. So by using the energy and momentum from the two daughter particles in a decay, the mass of the mother particle can be determined.

The masses of the particles analyzed in this thesis is presented in Table 2.1.

Table 2.1: Masses

Particle	**Mass (GeV/c^2)**
$\pi^{\pm}$	0.139570
p	0.938272
Λ	1.115683
K_s^0	0.497614

2.3.3 Pseudorapidity and rapidity

The dimensionless quantity *pseudorapidity* is a measure of the angle the particle from a collision is emitted. It is defined by

$$\eta = -ln(tan\frac{\theta}{2}) \tag{2.12}$$

where θ is the angle to the beam axis with $\theta = 0$ along the beam direction. This means that $\eta = 0$ perpendicular to the beam axis, see Fig. 2.3.

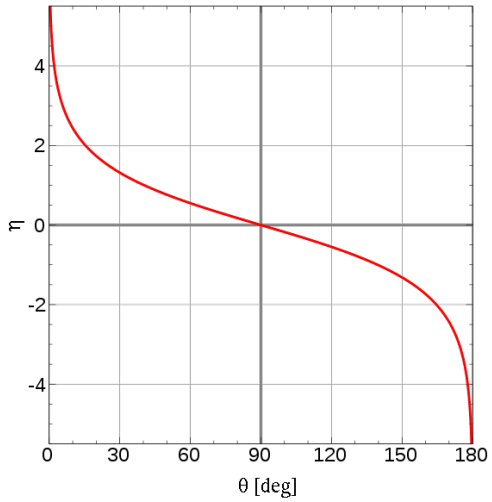

Figure 2.3: Pseudorapidity, η, as a function of the angle to the beam axis, θ, where $\theta = 0$ is in the beam direction. $\eta = 0$ perpendicular to the beam.

To calculate the boost invariant *rapidity*, y, of a particle, the particle needs to be identified first[6], since the energy and momentum of the particle are needed for the calculation [4]:

$$y = \frac{1}{2}ln\left(\frac{E + p_L}{E - p_L}\right) \tag{2.13}$$

where E is the total energy and p_L is the longitudinal momentum defined above. If a particle is created with $y = 0$ it implies that the particle is created in the center, if $y > 0$ it has been created in the forward region, and if $y < 0$ it has been created in the backward region of the collision in the rapidity space [15].[7]

When the transverse momentum of a particle is much larger than its mass (i.e. for high p_T particles), the rapidity can be approximated with the pseudo-rapidity.

[6]The particle species does not need to be known to determine the pseudorapidity.

[7]Having a boost invariant variable like this, one can compare fixed target experiments with collider experiments.

2.4 Quark Matter – The Quark Gluon Plasma

Amazingly, by creating – and studying – different phases of matter on a microscopic scale, one can draw conclusions of the performance and properties of the early universe on a macroscopic scale. The goal of the lead ion program at CERN is to recreate – on a very small scale in the lab environment – the state of matter as it was in the very early moments of the universe. One believe that this so called *quark matter* state differs from our ordinary nuclear (hadron) matter as it is built up by colored partons experiencing the strong force directly and not by color neutral nucleons which interact only with the external remnant of the strong force, namely the nuclear force. Scientists believe that nuclear matter could not have existed in the early universe due to its extremely hot and dense conditions; the quarks and gluons were free particles instead of bound to nucleons. Hence, a study of QGP is also a study of the strong force which binds quarks and gluons together. This is of great importance in our understanding of the fundamental forces, and how they are connected – and a strong motivation for LHC and its heavy ion program.

2.4.1 Confinement

As mentioned, the gluons are responsible for the strong force between the quarks. The potential between two quarks can be approximated as [15]

$$V_s(r) \approx -\frac{\alpha_s}{r} + kr \tag{2.14}$$

where α_s is the strong coupling constant describing the strength of the coupling, k is the string tension (see below), and r is the distance between the quarks. At small distances between the quarks, the first term dominates and the potential is inversely proportional to the distance, i.e. the potential energy decreases with decreasing r (and hence also the force), just as the Coulomb potential $V_{EM} = -\alpha_{EM}/r$, where α_{EM} is the electromagnetic coupling constant. But unlike the electromagnetic potential, the strong potential energy increases for increasing r – and the force is constant – since the second term in Eq. 2.14 starts to dominate. This is used by the *Lund string model*, saying that two quarks at large distance creates a color string consisting of several gluons between them, with a stored energy of kr [15]. As r increases, it is at some point more energetically favorable to create a quark-antiquark pair of the string – making the two initial quarks form two mesons. This is color confinement, i.e. the quark potential increases linearly with distance due to the color charge so that the quarks cannot be separated.

2.4.2 Phase transition to a deconfined state

In highly relativistic energy collisions of heavy ions, a fireball is created which expands under its own pressure and is cooled down under hadronization. Collisions of this type are characterized by high temperature and pressure, and in these conditions QCD predicts that matter which interacts strongly will undergo a phase transition to a deconfined state, the Quark Gluon Plasma (QGP).

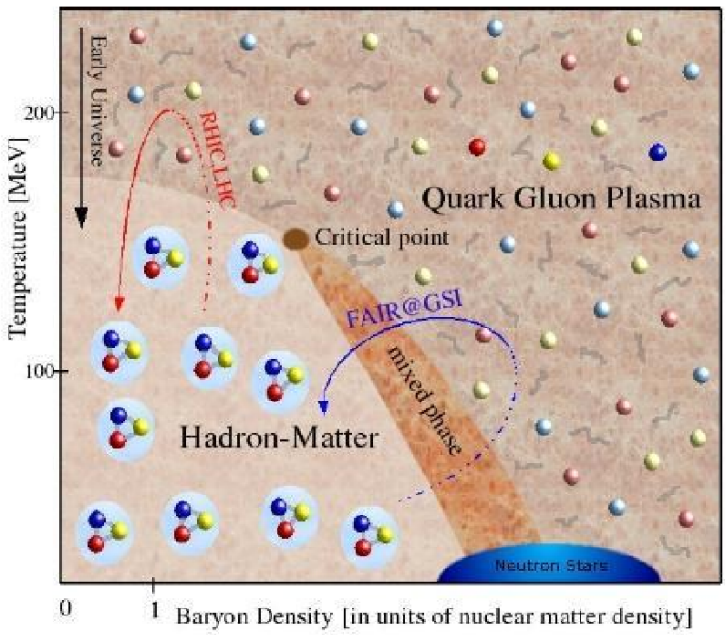

Figure 2.4: The QCD phase diagram [19]: temperature versus the net baryon density. At low temperatures and low baryon densities the phase is ordinary hadron-matter, and at high temperatures and/or high baryon density the matter enters the QGP phase. The diagram also indicates how the early universe evolved through the phases, where the neutron stars are located, and the time evolution of matter during a heavy ion collision.

A schematic view of the QCD phase diagram can be seen in Fig. 2.4 where the temperature is plotted versus the net quark (baryon) density[8] (the number of quarks minus the number of antiquarks per unit volume [15]) . At low temperatures and low baryon densities the phase is ordinary hadron matter. Above the phase boundary in the diagram – at high temperatures and/or high baryon density – the QGP phase should exist.

To make a phase transition from ordinary hadron matter to quark matter, critical values for the temperature and baryon density (compare with temperature and pressure in the water phase diagram) must be reached, see again Fig. 2.4. The critical point indicates that the transition to QGP is different to the "left" (at lower density and higher temperatures) and to the "right" (at higher density and lower temperatures) respect to this point. To the "right" of the critical point the phase transition is of first order, i.e. it is a smooth change between the two phases [12, 15] in which a mixture of both nucleons and plasma exists, while for the transition to the "left" of the critical point it is a second order phase transition with a more distinct boundary. This, however, is not yet experimentally proven.

In the schematic figure 2.4, other important regions are marked, e.g. the arrow indicating how the early universe[9] evolved through a phase of QGP from very high temperature (and low density) to a lower temperature when the universe cooled down and hadronized. An-

[8]Called the *baryon chemical potential*, μ.

[9]Some μs [15] after the Big Bang, scientists believe that the universe consisted of deconfined quarks, antiquarks and gluons.

other region in the diagram is the region where neutron stars form, where QGP is believed to occur due to the very dense, but cold, environment.

The time evolution of matter during a heavy ion collision can be described by a loop in the phase transition diagram, indicated by the red arrow. If the state created by a collision crosses the critical line, the QGP should exist for a short time period and then cool down under expansion, resulting in a reentering into the hadronic phase.

2.4.3 Deconfinement

As mentioned earlier, the quarks and gluons form colorless states as hadrons below the line in the phase diagram. In the new phase – the quark gluon plasma – the degrees of freedom of the quarks and gluons is much higher [10] than if the constituents were bound to hadrons. In other words, the plasma consists of free quarks and gluons. They are free in the sense that, above the critical temperature, the creation of quark-antiquark pairs increases and they will be separated with a small distance due to the high pressure. The strong force between the quarks decrease with decreasing distance[10] and hence the partons act like quarks and gluons which do not belong to a specific hadron, i.e. the QGP is a state with *deconfined*, but yet strongly interacting, matter [15]. At this point, the partons are expected to be *asymptotically free*: the color charges are screened by other color charges (due to fermionic fluctuations which produces loops of other color charges), and the interaction potential decreases exponentially after a distance larger than that of the length which the color charges screen out the color field, i.e. the Debye radius, r_{debye}. The interaction potential is hence

$$V(r) = \frac{e^{\frac{-r}{r_{debye}}}}{r} \tag{2.15}$$

This leads to the fact that potential hadrons, whose radius would be larger than r_{debye}, cannot bind together. In the QGP, where the density of partons is very high, r_{debye} is small, and the quarks and gluons are not bound to a specific hadron.

2.5 Signs of QGP

In the LHC energy range, presently at $\sqrt{s} = 7$ TeV for pp collisions and $\sqrt{s_{NN}} = 2.76$ TeV per nucleon in PbPb collisions, observables such as particle yield ratios and the slope of the hadron transverse momentum distributions are different for pp than in PbPb collisions, i.e. PbPb collisions are not only a superposition of pp collisions. To be able to discuss the changes in the observables in more detail, some variables need to be defined.

2.5.1 The nuclear modification factor

The nucleons that participate in a PbPb collision, and suffer a scattering, will produce colored partons which evolve into color strings that fragments (the Lund string model) to the

[10] See Sec. 2.4.1

hadrons which are detected. The total number of created particles is approximately proportional to the number of participants. This is true for normal processes at low p_T and is called participant scaling. Every participant nucleon can however collide with several nucleons in other nuclei. The total number of nucleon-nucleon (NN) collisions is the number of binary collisions, N_{bin}.

Rare processes, like hard scattering, giving high p_T particles or production of heavy flavor, require large momentum transfer in the individual NN collision. Any of the N_{bin} collisions can produce this, as each one of them is expected to have most of the full incoming energy available, since a soft collision that may have happened do not change the remaining energy very much and happen at a much longer time scale. It is very unlikely that a nucleon will experience two hard scatterings in a nuclear collision.

In a pp collision, there are two participants and one binary collision. The expected total multiplicity, which is dominated by soft processes in a nucleus-nucleus collision, is thus a factor $N_{part}/2$ larger[11] in PbPb collisions than in a pp collision at the same energy per nucleon. The production of high p_T particles in a heavy AA collision is expected to be the factor N_{bin} larger than in corresponding pp collision if no nuclear effect other than the superposition of pp collisions were present:

$$yield_{AA}(p_T) = N_{bin} \cdot yield_{pp}(p_T) \tag{2.16}$$

We therefore construct

$$R_{AA} = \frac{yield_{AA}(p_T)}{N_{bin} \cdot yield_{pp}(p_T)} \tag{2.17}$$

where R_{AA} is the nuclear modification factor. This implies that, if there are no medium induced modifications, i.e. if there are no initial- or final state effects that modify the yield, then R_{AA} should be equal to 1 at high-p_T where hard scattering dominates and binary scaling is expected. If the ratio, R_{AA}, is not equal to 1 at high p_T, this indicates that the presence of the nucleus has modified the production in some way, and that heavy ion collisions are not a simple scale up of pp collisions. Measurements of R_{AA} is a method to deduce the effects of the medium, where pp measurements work as a reference. Therefore, abnormalities in the ratio can be a sign of QGP and can be explained by e.g. recombination and jet quenching.

The results in this thesis will be the pp reference for Λ, $\bar{\Lambda}$, and K^0_s in future R_{AA} analyses of PbPb collisions.

2.5.2 Jet quenching

Fig. 2.5 shows the R_{AA} for central (i.e. when the nuclei overlap is large) PbPb collisions at $\sqrt{s}_{NN} = 2.76$ TeV in ALICE, and central AuAu collisions at $\sqrt{s}_{NN} = 200$ GeV at RHIC. The value of R_{AA} is much below 1 for all p_T bins. This can now be interpreted as a medium induced effect of the particle production. One of these interpretations is the jet quenching theory, explained in the following.

A jet is a stream of high p_T particles formed when a parton scatters off another parton with high momentum transfer. Jets are often initially formed in pairs, emerging back to back.

[11] N_{bin} or N_{part} can be determined using different models, e.g. the *Glauber* model.

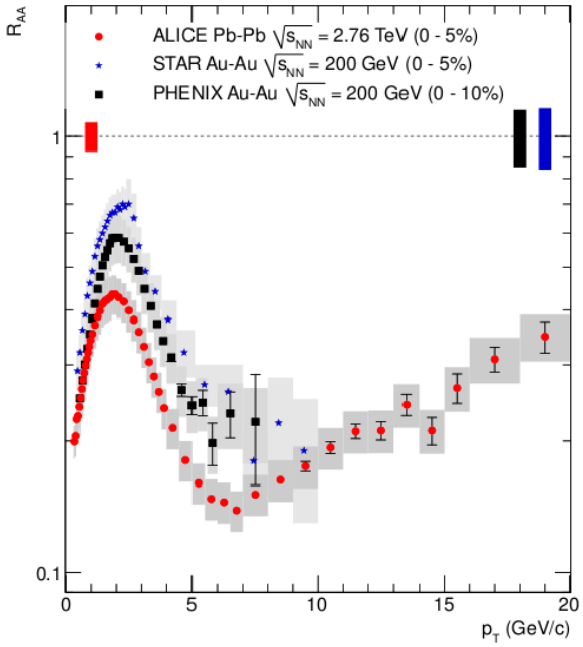

Figure 2.5: R_{AA} in ALICE for PbPb at $\sqrt{s_{NN}} = 2.76$ TeV, compared to the values obtained with AuAu at $\sqrt{s_{NN}} = 200$ GeV at RHIC [12].

In pp collisions, both of the two jets are observed, while in PbPb collisions, one of the two jets is often quenched; the jet has lost a significantly amount of energy on the way out from the created medium, indicating intense interaction by the scattered quark with the medium, which differs from the interactions that jets undergo in pp collisions due to the color medium. This scenario appears if the parton scattering occurs near the edge of the system since one of the jets then needs to travel a long distance through the medium, while the other does not.

The two jets are, though, more often formed in the center of the system, resulting in two quenched jets. This leads to less production of high p_T particles, explaining the suppression seen in the R_{AA} spectra, like the one shown in Fig. 2.5, where the measurements are done for central collisions. Jet quenching is considered as an evidence for QGP.

2.5.3 Recombination

The ratio Λ/K_s^0 or p/π in heavy ion collisions has been studied by e.g. the STAR experiment at RHIC (Relativistic Heavy Ion Collider at Brookhaven National Lab). An observation from these analyses is that the ratios are different than the ratios in pp collisions (which is studied here); baryons appear to be produced more easily than mesons at intermediate p_T[12] [14] in AA collisions, and that the magnitude of the baryon enhancement increases with the collision centrality, see e.g. Fig. 2.6 where the black (central AuAu collisions) and open pink (pp collisions) circles are interesting in this context. A related observation is that the p_T spectra for baryons are shifted to higher p_T by the production "kick" of the baryons.

[12] $p_T \sim 2 - 4$ GeV/c

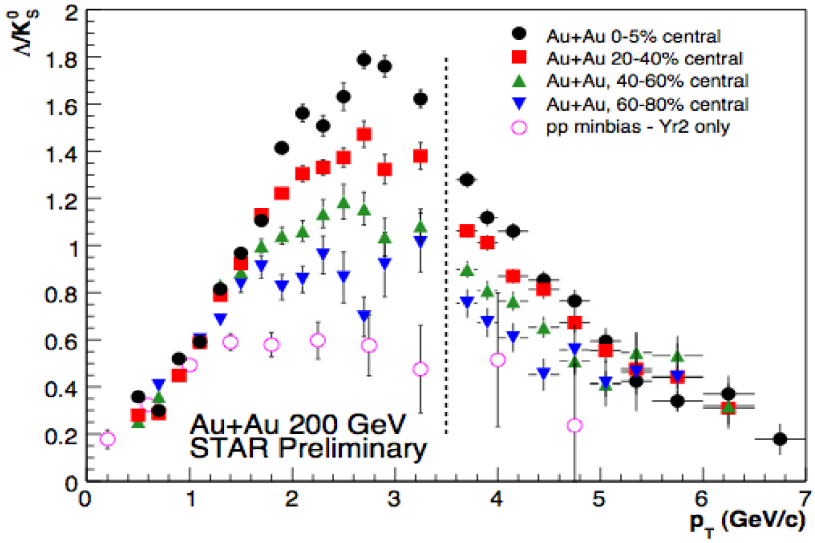

Figure 2.6: Λ/K^0_S from STAR data, AuAu collision at $\sqrt{s} = 200$ GeV. [17].

A model called the *recombination model*, discussed in the following, has been proposed to explain this. When the QGP is in its hadronization phase, i.e. when it is cooled down under expansion, the intuitive picture of this process is parton fragmentation (described by e.g. the Lund string model, see Sec. 2.5.1) which is the case when a hard (high p_T) parton hadronizes. But the recombination model is more likely in AA collisions at high energies since there are more soft (low p_T) partons in an AA collision than in the other types of collisions [4]. In other words, there are more quarks that are close in both coordinate and momentum space, i.e. they are close in *phase space*. Then, at some intermediate p_T, recombination could contribute significantly to the yield since it might be more easy for soft deconfined quarks to recombine to a intermediate p_T particle, than for a higher momentum quark to fragment.

In recombination processes, more intermediate p_T protons than pions are created during the hadronization; the protons get a bigger "kick". This is the case since – for "free" quarks – it is easier for three quarks (forming baryons), like the uud quarks in the proton or the uds of the Λ, to recombine, than a quark and an antiquark (forming a meson) that e.g. the pion consists of $(u\bar{d})$ or the $s\bar{u}$ of the K^0_S. This is an effect arising from the fact that partons are closer in a phase space where the momentum is low, than for a higher momentum phase space (since soft parton production dominates in AA collisions), see Fig. 2.7, which implies that there is a limit in p_T where recombination processes dominate over fragmentation processes. Therefore, three quarks with momentum lower than this limit will produce a particle with higher momentum, $p^p_T = 3 \cdot p^q_t$, than the momentum of a meson formed by a quark-antiquark pair, $p^p_T = 2 \cdot p^q_t$. This results in enhanced intermediate p_T baryons compared to mesons with the same p_T since, to form particles with the same momenta, the baryon constituents needed less p_T (where there is more quarks due to the fact that there is more partons in lower momentum phase space) than the meson constituents (i.e. in a p_T range where there are less quarks in the phase space region representing this momenta), see Fig. 2.7.

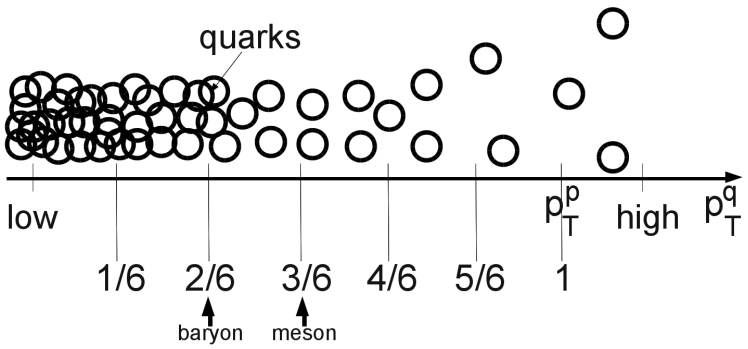

Figure 2.7: A schematic figure over the explanation of the enhanced baryon yield compared to mesons: it is easier for three quarks to recombine to an intermediate p_T particle, than a quark-antiquark pair to a particle of the same p_T since partons are closer in a low momentum phase space (baryons require lower momentum of its quarks due to the fact that they are three – which is more than the quarks of the meson), than for a higher momentum phase space (in which the quarks of the meson needs to be since they are only two), resulting in enhanced intermediate/high p_T baryons compared to mesons with the same p_T.

2.5.4 Strangeness enhancement

Strange hadrons contain at least one strange quark or anti-quark, for example the Λ or K. As the strange quark is heavier than the up and down quarks, the production of strange hadrons is less than the production of hadrons containing up and down quarks [9]. This is however true only for pp collisions. It is observed that the number of strange particles is increasing in AA collisions, when QGP is expected. Due to the fact that strange quark production increases in AA collisions compared to pp collisions, it is seen as an indication of QGP formation [9]. Strangeness enhancement is explained by the following: in a QGP the mass of a quark drops to its bare mass since it is not longer bound within a hadron. A strange quark bare mass is $\sim$ 150 MeV, while the temperature of the medium is $\sim$ 200 MeV and contains many deconfined gluons which can produce strange quarks via gluon fusion ($gg \rightarrow s\bar{s}$), since this is now energetically allowed and the dominant process for strange quark production [15].

Also, the *Fermi sea* of u and d quarks is expected to be filled quickly in a QGP since u and d quarks – which are fermions obeying the Pauli principle – are produced in large numbers, and it is therefore more energetically favorable for the gluon fusion to produce heavier quarks, such as $s\bar{s}$ pairs, which can form hadrons containing strange quarks. Due to enhanced strange production in the QGP, the number of strange hadrons formed by recombination of quarks is also enhanced compared to the strange hadron production in collisions where QGP is not formed [15].

In the analysis part of this thesis, strange hadrons are analyzed as a referens for later AA analyses, but also because the pp aspect of strange particle production is interesting in itself.

Chapter 3

The ALICE experiment at LHC

ALICE – with a length of 26 m, a height of 16 m, and a total weight of around 10000 t [4] – is a general heavy ion purpose experiment which measures hadrons, leptons and photons at mid-rapidity, and muons at large rapidity. ALICE is designed to be able to handle charged particle *multiplicities*, $\frac{dN_{ch}}{d\eta}$, of 8000 where the expected value for this quantity (model dependent) is 2000-6000 in heavy ion collisions. ALICE is optimized to measure the particle momentum, p, and the specific energy loss, $\frac{dE}{dx}$, the time of flight information, and the transition and Cherenkoc radiation, to be able to perform particle identification (PID) – for most tracks PID is performed event by event. When combining the different information about the particles created in a collision, ALICE can provide PID over the transverse momentum range 0.1 GeV/c < p_T < 20 GeV/c or higher in some cases.

3.1 The detectors

The ALICE experiment consists of several detectors with different functionalities. The forward spectrometer measures muons, from which heavy flavor, mainly J/ψ are reconstructed. The central barrel detectors are located inside the L3-solenoid (providing a magnetic field up to 0.5 T [4]) and cover $|\eta| < 0.9$. They measure hadrons, electrons, and photons. The ALICE-detectors will be briefly introduced in the following.

3.1.1 The Inner Tracking System (ITS)

The Inner Tracking System is a silicon tracker located in the central barrel, closest to the beam axis. It consists of six cylindrical layers of silicon detectors [7]. The purpose of the ITS is to provide high resolution space points to trace the tracks back from the TPC to the interaction vertex. It reconstructs the primary vertex with a resolution of $\sim 100\mu m$ [4]. It is also optimized for finding secondary vertices, and measures the energy loss and multiplicity, $\frac{dN}{d\eta}$.

Since it is the closest detector to the beam pipe, the very low momentum particles ($<$ 200 MeV/c) do not travel a longer distance than the boundaries of the ITS, since they are deflected too much by the magnetic field, or they decay before reaching the TPC. The ITS can reconstruct some of these particles that never reach the TPC.

3.1.2 The Time Projection Chamber (TPC)

This is the main detector used in this analysis and it will be described in detail in Sec. 4.

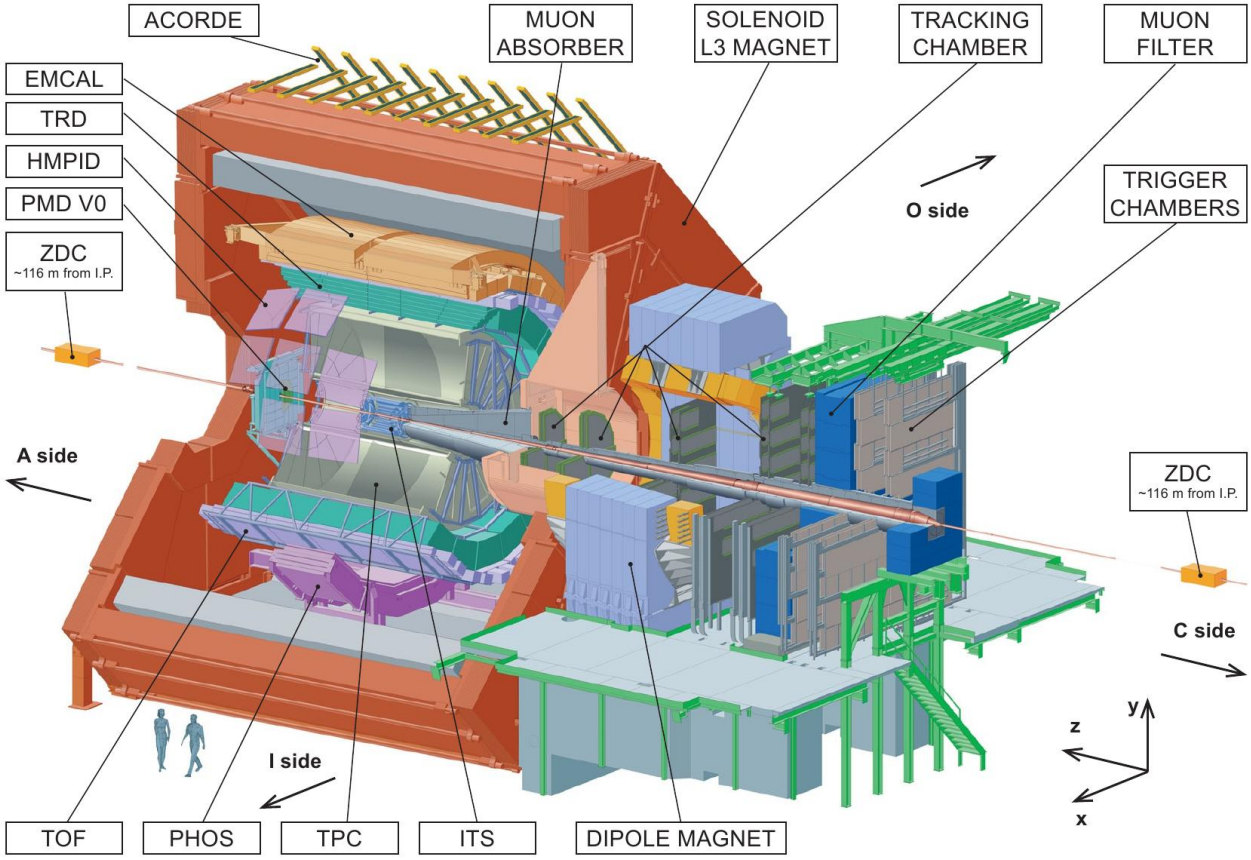

(a) Schematic view of the ALICE experiment with all its detectors [1].

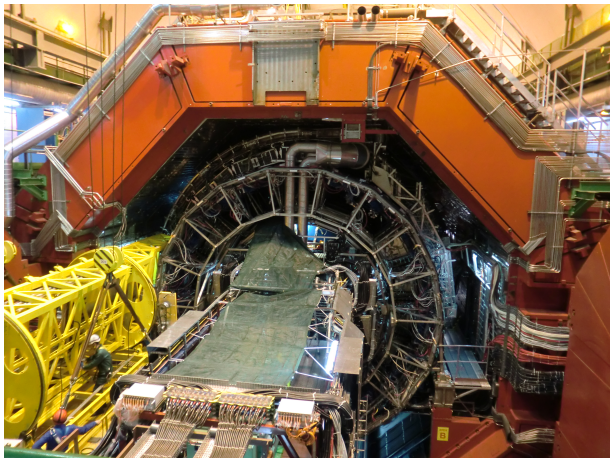

(b) A photo of the A-side of the ALICE detector complex at Point 2 of LHC.

Figure 3.1: The ALICE experiment which consists of several detectors in the forward region and in the center located inside the magnet. ALICE can measure hadrons, electrons, muons, and photons.

3.1.3 The Transition Radiation Detector (TRD)

In the Transition Radiation Detector, a charged particle passes many times between two media with different dielectric constants. This give rise to transition radiation (X-ray photons) detected in multi wire proportional chambers.

The purpose of detecting the transition radiation is to distinguish electrons from pions with momenta above 1 GeV/c. It also contributes to the tracking and can provide a trigger signal for high momentum particles [4].

3.1.4 The Time-Of-Flight (TOF) detector

The Time-Of-Flight detector is located in a cylindrical shell and consists of 18 sectors with 5 modules each with Multi-gap Resistive Plate Chambers (MRPCs) [4]. There is also a central anode and pick up pads. When a particle enters the gas gaps in the MRPC, it ionizes the gas and produces charge clusters which start avalanche multiplication. The time resolution of the TOF is 100 ps. The signal is then the sum of all avalanches. The signals from the TOF is the difference in time of flight for particles with the same momentum but different mass. Hence, by knowing the collision time, the velocity of the particles can be determined and since the arrival time and the momentum is measured, the track path length can be calculated. With this information, the mass of the particles can be determined, which hence allows PID in the low momentum range ($p < 3$ GeV/c) [4].

3.1.5 The High-Momentum Particle Identification Detector (HMPID)

The purpose of the High-Momentum Particle Identification Detector is to measure and identify hadrons at p_T around 1 GeV/c. This is done by measuring the Cherenkov radiation – which is emitted in a cone with an angle depending on the particles velocity – from the particle traversing a dielectric medium with a speed greater than the speed of light. The correlation between the cone angle and the momentum allows for PID [4]. The HMPID covers only a small azimuthal acceptance.

3.1.6 The Electromagnetic Calorimeter (EMCal)

The EMCal consists of a lead scintillator sampling calorimeter [4], and it provides discrimination of electrons from hadrons. The main purpose of the EMCal is to measure the energy from neutral particles for jet reconstruction. It can also measure high energy photons from which π^0 and η can be reconstructed. These are the hadrons that can be identified up to the highest p_T and are important to study the jet quenching effect. Another important observable is the thermal photon production from the QGP and the direct high p_T photons which traverse the QGP with only electromagnetic interaction.

3.1.7 The muon arm

There are a number of forward detectors in ALICE. For example the muon spectrometer which measure muons with absorbers and tracking and triggering chambers surrounded by a dipole magnet. The muons are measured to reconstruct J/ψ particles.

3.1.8 The global detectors

Other forward detectors, such as the FMD, T0, and V0, are used for triggering purposes.

The FMD (Forward Multiplicity Detector) measures the charged particle multiplicity, $dN/d\eta$, and determines the reaction plane [4]. This is done by several arrays of silicon strip detectors.

The V0 detector is two scintillator hodoscopes located upstream and downstream of the vertex. It is used for triggering as well as centrality and luminosity estimations, and in addition it removes beam-gas interaction background [5].

The T0 measures the real time of the collision and determines the vertex position with coarse resolution for online purposes.

3.2 Track reconstruction

To reconstruct charged particle tracks in the ALICE detectors, a tracking procedure based on the *Kalman filter* is used. This method selects a track candidate from the information given at a previous point in the iteration, explained below.

Before the tracking procedure can start, all charge clusters have to be found. In e.g. the TPC, the cluster finder algorithm loops over pads and time bins for all pad rows (all silicon sensors in the ITS) and searches for the local charge maxima in pad and time, and assigns a 5×5 bin region in time and pad direction around the maximum. The coordinates of the cluster is then calculated as the center of gravity of the cluster [5].

Now the tracking can start. First, a so called *seed* is found in the TPC as an initial approximation of the track position. The seed is a pair of clusters in two outer TPC pad rows (separated by a few rows) with track parameters which allow the track to be projected to the primary vertex position calculated from the clusters reconstructed in the inner SPD layers of the ITS [4, 5]. There is also a seed finding algorithm where this requirement does not have to be fulfilled, e.g. for V^0 decay particles which should not point back to the primary vertex.

When the seed is found an estimate of the track p_T is done, and the *state vector* parameters are calculated from the seed (no details about how the parameters are calculated is mentioned here, instead see reference [4]). The state vector is used to find the next cluster in the track, if there is any, as it can predict the direction of the track from the previously found clusters, i.e. the Kalman filter starts with the seed and its few parameters, and then associates new track points with the help of the parameters by estimating the state vector and predicts the next coordinate [4]. After a successfully found cluster, the parameters are updated accordingly and hence becomes more accurate with large number of clusters assigned to the track.

The tracking begins from the outer point in the seed which is located at the outer radius of the TPC, and then proceeds towards the inner limit of the TPC where then the tracking algorithm assigns reconstructed ITS clusters to the TPC track [4]. Here, a standalone ITS tracking procedure is applied to find the tracks missed by the TPC by considering the remaining clusters in the ITS. This is done from the primary vertex to the outer part of the TPC. The tracks are then extrapolated to the TRD, TOF, HMPID, PHOS, and EMCal detectors. To finish the

tracking, the tracks are refitted with the Kalman filter from the outer detectors to the primary vertex (or to the innermost possible radius, in the case of a secondary track) [4].

In Fig. 3.2, an event display is shown where the tracks found by the tracking algorithm can be seen.

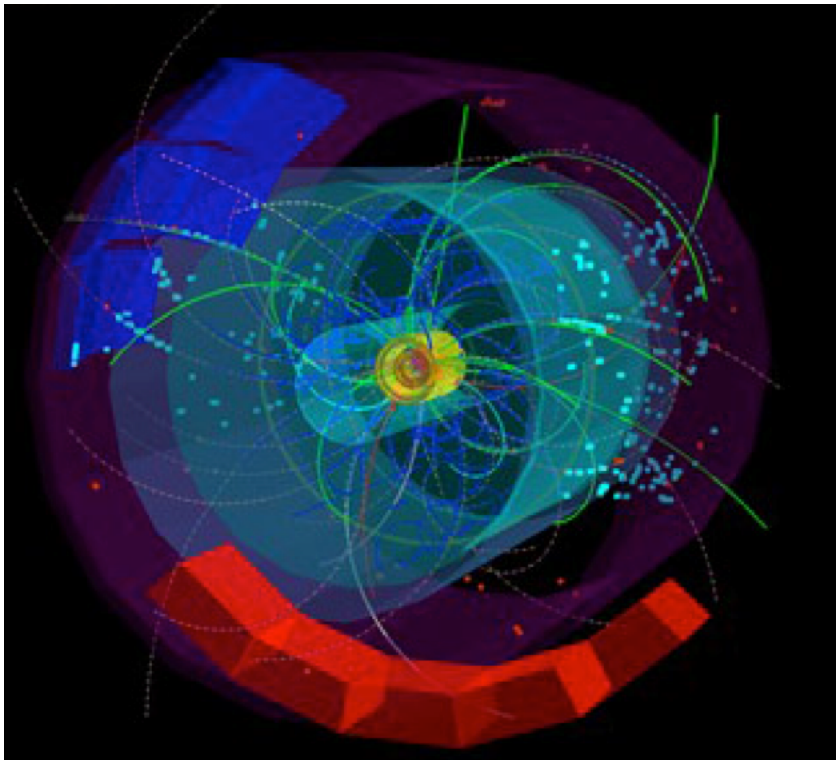

Figure 3.2: Reconstructed tracks in the TPC, ITS, and other subdetectors for a pp collision at 7 TeV [18].

Chapter 4

The Time Projection Chamber (TPC)

4.1 The working principle

The Time Projection Chamber (TPC) is the main tracking detector in the ALICE experiment due to its large acceptance; it covers 2π in azimuthal angle and the pseudorapidity region $|\eta| < 0.9$ (the polar angle) for the full track length [7]. Its tasks are to record the track trajectory in three dimensions of the charged particles traversing the detector, to measure the particle momentum and its energy loss to be able to perform PID (in the range 0.1-20 GeV/c). These goals are reachable by the TPC structure described below.

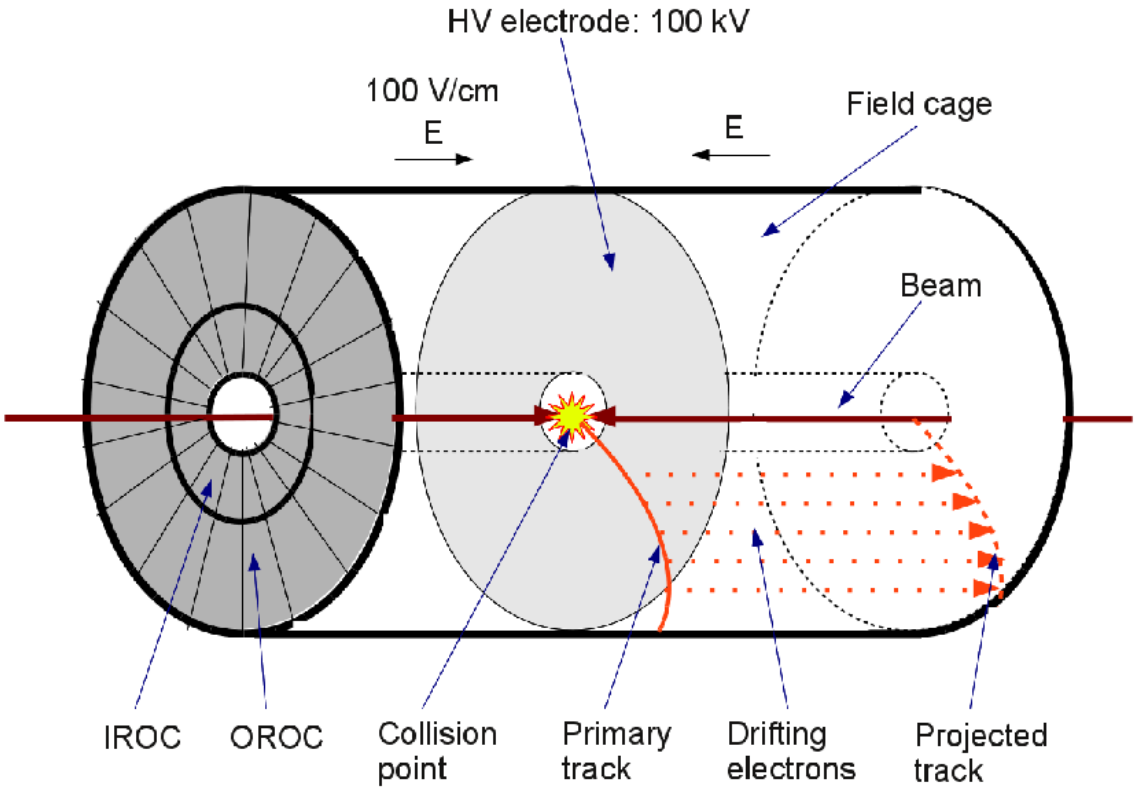

Figure 4.1: The cylinder shaped TPC. The chamber is filled with a gas, and a central cathode divides the drift region in two halves, providing a uniform electric field parallel to the magnetic field. Wire chambers (IROC and OROC) and read out electronics are located at the ends.

The TPC is a cylinder shaped chamber with an outer diameter of 5.56 m (inner radius of ~80 cm, and outer radius of ~280 cm) and a length of 5.1 m in the beam direction [7]. The chamber is filled with a $Ne - CO_2 - N_2$ gas, which is the detector medium. A central cathode membrane divides the TPC drift region in two equally large, symmetric halves, see Fig. 4.1.

The central cathode provides a uniform electric drift field of 100 V/cm, directed along the cylinder axis, parallel to the magnetic field provided by the L3 solenoid magnet surrounding the TPC. The wire chambers and the read out electronics are located at the ends of the cylinder.

When a charged particle from a collision (a primary particle) is entering the TPC gas volume, called the *drift region* (the field cage), it will ionize the gas (and hence loose energy) creating electron-ion pairs along its trajectory. Due to the applied magnetic field, the primary particle will bend off in a trajectory where the curvature is determined by the momentum (defined by Eq. 2.5) of the particle. The electrons produced along the path of the primary particle will drift towards the endcaps of the TPC, and thus projecting the particle's trajectory on the read out chambers, see Fig. 4.1. The maximal drift time of the electrons is 92 μs [7]. A gas *amplification* system at the ends of the TPC is made of Multi Wire Proportional chambers which provide strong electric fields around very thin anode wires, under which the incoming electrons are accelerated and hence ionizing the gas further, forming an avalanche of ions inducing charge clusters on the cathode plane due to the movement of the positive ions, see Fig. 4.2. The nominal gain in the ALICE-TPC is 7000-8000 [1]. The location of the clusters can be measured by segmenting the cathode plane into small electrodes, or *pads*.

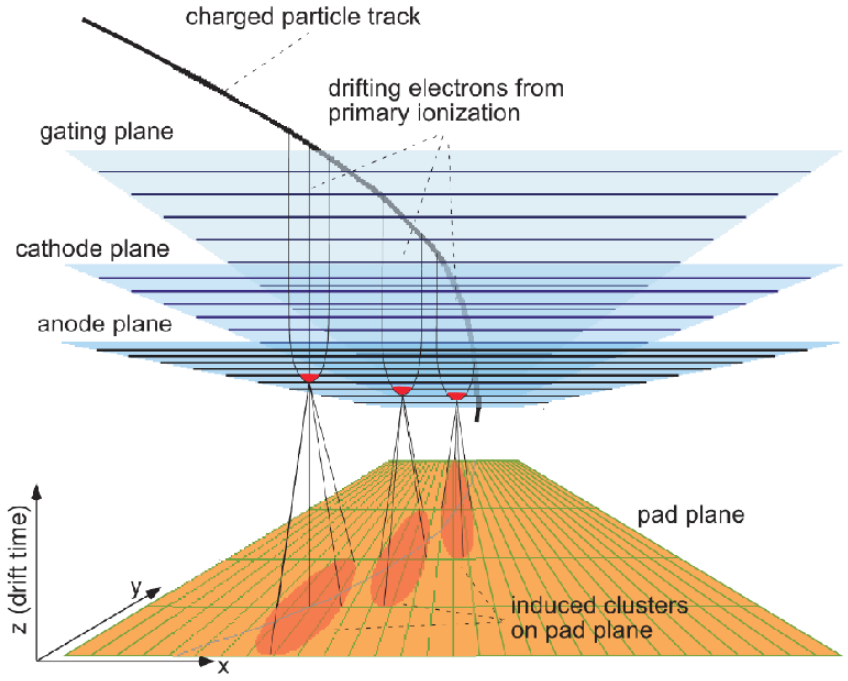

Figure 4.2: The TPC wire planes [1]. When a particle enters TPC and ionizes the gas the electrons drift towards the endcaps, projecting the particle's trajectory. The gas amplification system provides a strong electric field around the anode wires, under which the electrons ionize the gas further, forming an avalanche at a location which can be measured since the positive ions from the avalanche induce signals on the pads. In this way a track can be reconstructed

The two-dimensional location of the track can therefore be obtained by knowing the coordinates and the geometry of the pads, and the signal amplitude on each pad. The third dimension is derived by measuring the drift time of the ionization electrons to reach the anode wires and convert this to a distance by knowing the drift velocity of the gas. In the ALICE-TPC, the drift velocity in the gas ($Ne - CO_2 - N_2$ [1]) is 2.65 cm/µs [1]. From a large number of measured points on a trajectory, the track of the traversing particle can be reconstructed.

The position resolution in the drift direction is 1100 - 1250 µm [7], and, as can be seen in Fig. 4.3, the space point resolution in pad row direction (with TPC coordinates: y, or $r\phi$) is 300-500μm for high p_T tracks, with a low pad inclination angle, α, i.e. the crossing angle of the track with respect to the TPC chamber.

In Fig. 4.4 the p_T resolution with maximum number of samples is seen, with a value of 1% for momenta of 1 GeV/c and 7% for momenta of 10 GeV/c [8].

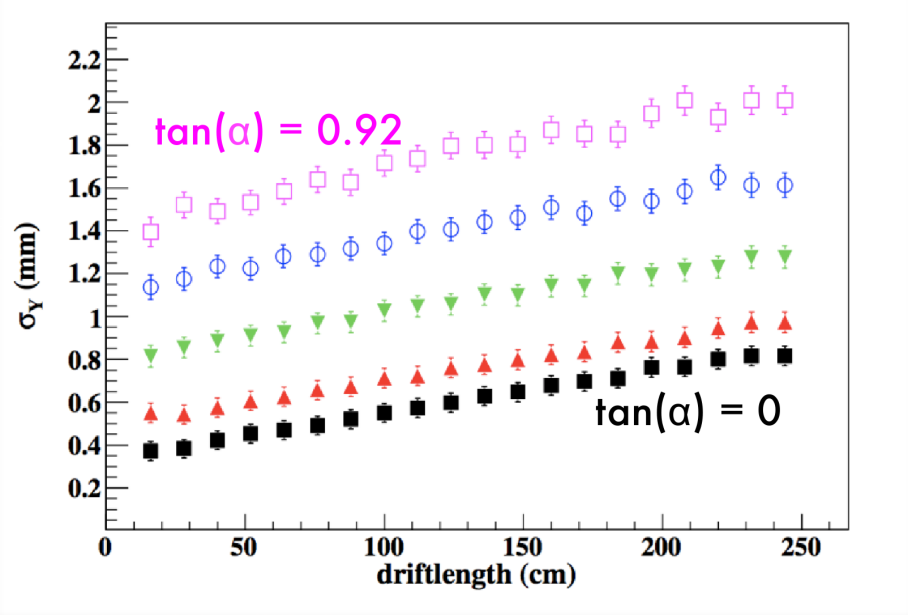

Figure 4.3: Space point resolution in pad row direction (in TPC coordinates: y) as a function of drift length and different pad inclination angle, α, showing a value of 300-500μm for high p_T tracks with a low inclination angle [1, 18].

[1] 85.7%-9.5%-4.8%

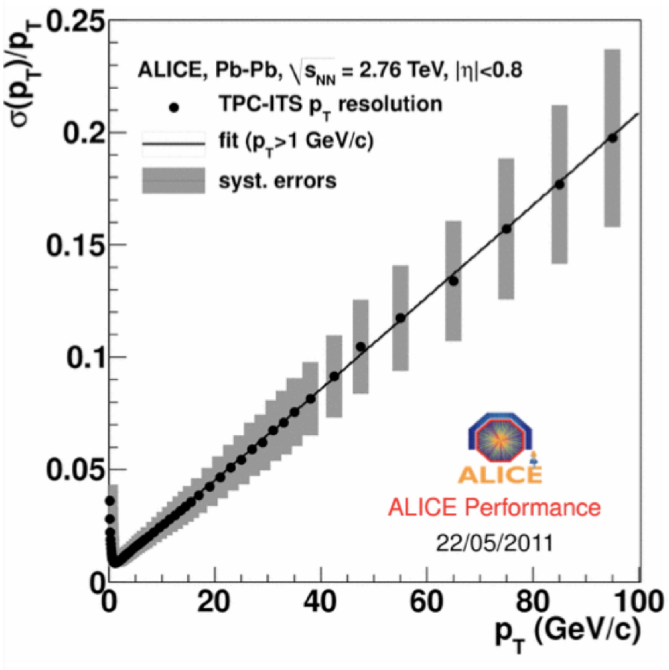

Figure 4.4: Transverse momentum resolution with maximum number of samples in a PbPb collision (maximum number of samples) [18].

4.2 To read out an event

4.2.1 The readout chambers

The readout chambers are composed of 18 trapezoidal sectors, each covering 20° in azimuth. The sectors are divided into an inner and outer readout chamber (IROC and OROC). There are three wire planes, namely:

1. The gating grid plane, which is *open* when all wires are at the same potential, then electrons can drift from the drift region to the amplification region. Open mode is determined by a trigger from other detectors in ALICE. In *closed* mode, the gating grid is biased with a bipolar field $U_G = 70 \pm 90$ V. This prevents electrons from drifting into the amplification region and stop ions created in the avalanche process from drifting back into the drift region [1].

2. The cathode wire plane (ground potential) which separates the drift volume from the amplification region. The cathode wires collect the ions produced in the amplification.

3. The anode wire plane ($V_A = 1450$ V for both IROC and OROC) whih is responsible for the amplification.

The final readout plane is a padplane at ground potential located 3 mm (OROC) or 2 mm (IROC) from the anode wire plane, see Fig. 4.2. The inner and the outer ROC consist of totally 159 radial pad rows (a track can then have a maximum of 159 clusters). The ions produced in the avalanche process induce a signal (current) on the pads, and the pads are

then read out separately. How large the signal on a pad is, depends on the charge in the avalanche and the distance from pad to avalanche.

Table 4.1: Pad sizes

Pad size (mm^2)	**Chamber**	**Number of rows**
4×7.5	IROC	63
6×10	inner OROC	64
6×15	outer OROC	32

Table 4.2: Wire properties

	Anode wires		**Cathode wires**		**Gating grid wires**	
	OROC	**IROC**	**OROC**	**IROC**	**OROC**	**IROC**
Distance from pad plane (mm)	3	2	6	4	9	7
Number of wires	456	200	457	201	912	400
Pitch (mm)	2.5	2.5	2.5	2.5	1.25	1.25
Diameter (μm)	20	20	75	75	75	75
Material	Au plated W		Cu-Be (98%-2%)		Cu-Be (98%-2%)	
Density (g/cm^3)	19.25		8.80		8.80	
Tension (N)	0.45		1.2	0.6	1.2	0.6
Min. length (cm)	45	27	45	27	45	27
Max. length (cm)	84	44	84	44	84	44

4.2.2 The trigger

If a certain requirement – based on physics interest – of an event is fulfilled, the ALICE trigger system (CTP - Central Trigger Processor) starts, and a decision whether to keep the event or not is made. The trigger system is divided into three levels: the first decision is made at 1.2 μs after the event (this is L0) and is based on information in the form of electronic signals. L0 opens the gate of the TPC. The second level, L1, accepts or rejects the event 7.7 μs after the interaction time at which time the sampling of the signal waveform starts. The sampling measures the voltage at 10MHz sampling rate. If the event is rejected, the trigger sequence is finished, otherwise the third level trigger, L2, kicks in after 100 μs (corresponding to the TPC drift time) which completes the sequence. L2 rejects or accepts the event, and in case of acceptance, the event is transferred from the data buffers to the DAQ where further trigger decisions are made in the HLT, the High Level Trigger system, where track information can be used for further filtering before data is written to disc.

4.2.3 The read out electronics

The positive charge in the avalanche created locally around the anode wires will induce charge in the pad plane, proportional to the original charge released by the particle ionization. To convert the induced charge into analyzable data, the pads are connected to read out electronics. Each pad is connected to a connector on a kapton cable which transfers the signal to an FEC (Front End Card). The signal processing chain is pipelined within one single channel, but 16 channels in parallel in the PASA and ALTRO chip.

The charge induced on the pads is read out in the following way, referring to Fig. 4.5. The preamplifier/shaper chip (PASA) on the FEC first converts (and amplifies) the charge induced on each pad to a voltage proportional to the charge with the preamplifier. The total conversion gain after both the preamplifier and the shaper is 6 ADC counts/fC [1], i.e. the amplification converts a signal of 1000 electrons into one ADC channel. The charge induced on a pad has a specific time distribution with a tail due to the slow drifting ions. To extract the necessary information about the signal (amplitude and time of occurance), the signal is shaped to a differential Semi-Gaussian signal with a shaping time of 190ns

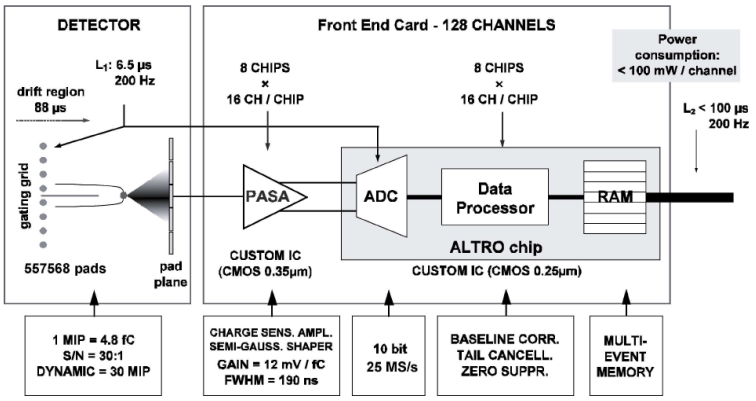

Figure 4.5: A block scheme over the TPC front end electronics [1]. The pads are connected to the read out electronics which first transfers the signal to the FEC's where the PASA converts the current to a voltage pulse proportional to initial charge which is shaped. The analog signal reaches the ALTRO which digitizes it with an ADC, corrects the baseline, performs tail cancellation and zero suppression. The FEC's are read out via a data bus controlled by a Readout Control Unit (RCU).

The analog signal then reaches the ALTRO (ALice Tpc Read Out) chip which digitizes the signal with an ADC (Analog to Digital Converter) by measuring the signal amplitude with 10 bit resolution in 1000 samples spaced by 100ns. Thus the measurement prevails over 100 microseconds, i.e. the total drift time for the last arriving (longest drift length) electrons from an event. The ALTRO then performs baseline correction, tail cancellation, i.e. suppresses the long pulse tail (due to drifting ions) which improves separation for multiple clusters in the time direction of a channel. A second baseline correction is done before the zero suppression. With zero suppression, data that do not fulfill the requirements for the definition of a pulse are discarded. This minimizes the load on the RCU and the data transfer and storage capability needed. After zero suppression, the signals are buffered while waiting for L2 trigger decision on whether to keep the data or not.

The FECs are read out via a 40 bit wide data bus controlled by an RCU (Readout Control Unit) that transfers the digital data for each time sample and each pad to the DAQ and the HLT [1].

4.3 The TPC signal

4.3.1 Energy loss and the Bethe-Bloch formula

When a charged particle enters the TPC drift region, it will loose energy by ionizing the gas atoms along its path in the TPC. The Bethe-Bloch formula describes the mean energy loss per unit path length [4]

$$-\left\langle \frac{dE}{dx} \right\rangle = Kq^2 \frac{Z}{A} \cdot \frac{1}{\beta^2} \left(\frac{1}{2} ln \frac{2m_e c^2 \beta^2 \gamma^2 T_{max}}{I^2} - \beta^2 - \frac{\delta(\beta\gamma)}{2} \right) \tag{4.1}$$

where the constant $K = 4\pi N_A r_e^2 m_e c^2$, and here r_e and m_e are the classical radius and mass of the electron. N_A is the Avogadro's number, Z is the atomic number and A the atomic mass of the material (the TPC gas, in this case), q is the electric charge of the particle, $\beta = v/c$ which is the velocity of the particle traversing the gas, $\gamma = 1/\sqrt{1-\beta^2}$, I the mean ionization potential of the material, $\delta(\beta\gamma)$ is a density effect correction, relevant for particles with $\beta\gamma = p/m >> 3$, see Ref. [4] for further discussion of this term. T_{max} is the maximum kinetic energy that can be given to a free electron in a single collision, given by [4]

$$T_{max} = \frac{2m_e c^2 \beta^2 \gamma^2}{1 + 2\gamma m_e/m + (m_e/m)^2} \tag{4.2}$$

for a particle of mass m. This expression becomes $T_{max} = 2m_e c^2 \beta^2 \gamma^2$ for a particle with its mass much greater than the electron mass.

The Bethe-Bloch formula can give a complex first impression, but, as a matter of fact, for all practical purposes, the dE/dx given by Eq. 4.1 depends only on $\beta\gamma = p/m$. Now consider Fig. 4.6, where each dot in the correlation plot corresponds to a particle whose energy loss and momentum are measured. The different particles follow different correlation bands. At low momentum, i.e. at low $\beta\gamma$, the energy loss is dominated by the $1/\beta^2$ factor since it is steeply decreasing with increasing momentum until a minimum is reached at $\beta \sim 0.97$ [4]. In this region, the particles are called *minimum ionizing particles* (MIP's). Above this region, when the momentum increases further, $1/\beta^2 \approx 1$ and thereby constant. This makes the energy loss grows as $ln(\beta\gamma)$ since T_{max} increases as $\beta^2\gamma^2$ due to large energy transfers to a few electrons. This region is the *relativistic rise*, which will be discussed further in the analysis. Particles are identified by determining what band they belong to, see Fig. 4.6.

For low p_T, the identification is easy since the bands are well separated, and unique identification on a track-by-track basis is straightforward [7].

The band of electrons limits the particle identification with dE/dx and momentum. If electrons are identified by other means, like Cherenkov, transition radiation, or calorimeter response, they can be removed from this identification plot, and then PID can go further up in momentum. The region of minimal ionization, i.e. up to 2 GeV/c, is more or less impossible for PID with dE/dx. There PID is done by time of flight measurements. The difference in mass between muons and pions is small, and thus PID between them is normally difficult. A TPC with its excellent PID has some chance to separate them in the low momentum region. Normally, one will have to correct for such admixture by simulations, since muons mostly

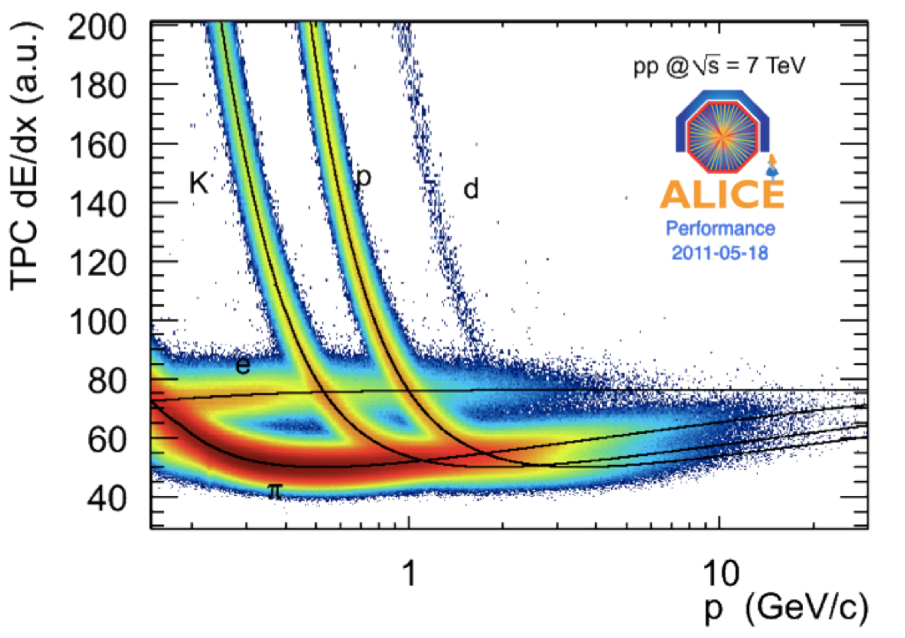

Figure 4.6: The Bethe-Bloch curves for different particle species where the energy loss per unit path length, dE/dx, is plotted versus momentum, p. This figure is from pp collisions at 7 TeV obtained with the TPC [18]. The particles follow different correlation bands.

are decay products from pions and kaons. When we talk about PID by dE/dx, we normally mean charged hadron PID while electrons and muons are identified by other means.

At higher p_T, at the relativistic rise, the PID is possible but difficult since the particle bands overlap. However, statistical PID (which does not allow to know the identity of individual particles) is still possible, and in Sec. 4.4, the PID procedure is described for this momentum range.

4.3.2 The signal representing $< dE/dx >$

The energy loss is a statistical process which is described by a Landau distribution. The $< dE/dx >$ as obtained from the Bethe-Bloch formula represents the average of the Landau distribution. The advantage of a TPC is that a large number of dE/dx values (ideally 159) are measured. The average energy deposit is highly affected by the long tail towards higher energy losses [11]; the Landau distribution. The TPC signal is instead calculated as the truncated mean of all cluster charges (the dE/dx signals, from now on called $< dE/dx >_{tr}$ where tr stands for *truncated*), where 60% of the lowest charges of the dE/dx samples are used (i.e. of the whole track). Thus the tail region, which adds large fluctuations to the $< dE/dx >$ – since it is made up of contributions from rare ionization events with large energy transfer to an electron – is omitted from the average.

4.4 PID on the relativistic rise based on the dE/dx information

There exists several ways of obtaining the p_T-spectra, the particle ratio and the R_{AA}. For my Λ and K_s^0 (particles that decay before reaching the TPC) analysis I use the information from the invariant mass distribution for particle identification. This is an example of statistical identification since it can be used to determine the integrated yield of the mother particles, but it can not, with certainty (at least when the background is large), point out which reconstructed decay corresponds to a mother particle and which is just the result of a combinatorial chance. This is explained later. Here follows instead a short description of the general Lund group working procedure to obtain pion, kaon and proton spectra.

The TPC $< dE/dx >_{tr}$ information allows PID track by track at low transverse momentum, typically below 1 GeV/c. To construct a p_T spectrum at higher ranges of p_T, and to be able to construct the fraction of pions or the quantity $\pi/(\pi + K + p)$ for recombination analyses, the yields of each particle type are vital information. Since the separation between particles is not clean on the relativistic rise of the Bethe-Bloch formula (where p_T is above 3 GeV/c), the yields have to be extracted statistically. This is done by first calibrating the $< dE/dx >_{tr}$ for high p_T by determining the $\beta\gamma$ dependence, and the sigma of $< dE/dx >_{tr}$ by extrapolating the sigma for the MIPs[2] since the $< dE/dx >_{tr}$ is not dependent of the momentum here, and a clean pion sample can be found. Then, the $< dE/dx >_{tr}$ distribution for each p_T bin is fitted with the sum of three (or four, if the electrons are included) Gaussians – one for each particle type (π, K, and p). The fitting is done for the p_T-bins which are used as bins in the p_T histogram. As the $< dE/dx >_{tr}$ background is negligible, the integrals of the Gaussians give the number of identified raw counts [7], see Fig. 4.7.

A Gaussian has three free parameters namely the width (describing the resolution), the mean and the yield. The total number of parameters for three Gaussian are hence 9. The PID analysis is therefore more reliable if as many of these parameters as possible are constrained. The sigma (width) is extracted from the data (see above) and then the mean can be calculated from the Bethe-Bloch, and the width can be constrained and fixed - that is 6 of the 9 parameters.

From the particle yields of the fits in different p_T bins, a p_T-spectrum can be constructed, see Fig. 4.8(a). The ultimate goal is to construct p_T spectra of pions, kaons, and protons in this momentum region. So far only the pion yields can be extracted reliably. The fraction of pions among all the charged particles can be obtained, see Fig. 4.8(b), even though the ratio between the protons and pions is the true interesting results.

The results from these studies are reported elsewhere [4, 13, 12]. But the results from this analysis can be cross checked and perhaps refined using the clean pion and proton samples from Λ and K_s^0 decays. If a clean sample of protons and pions can be obtained, a similar dE/dx analysis can be done with this data sample to verify the shape, mean and width of the π and $p < dE/dx >_{tr}$ distributions.

[2] $0.4 < p < 0.6$ GeV/c and $40 < dE/dx < 60$

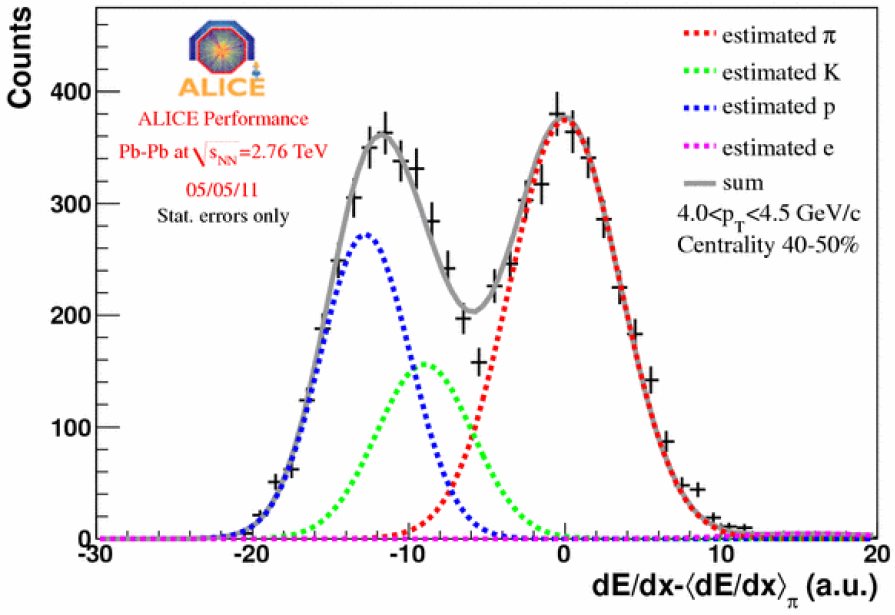

Figure 4.7: $< dE/dx >_{tr} - < dE/dx >^{\pi}_{tr}$ and the fits for $4.0 < p_T < 4.5$ GeV/c, in pp collisions with $\sqrt{s} = 7$ TeV.

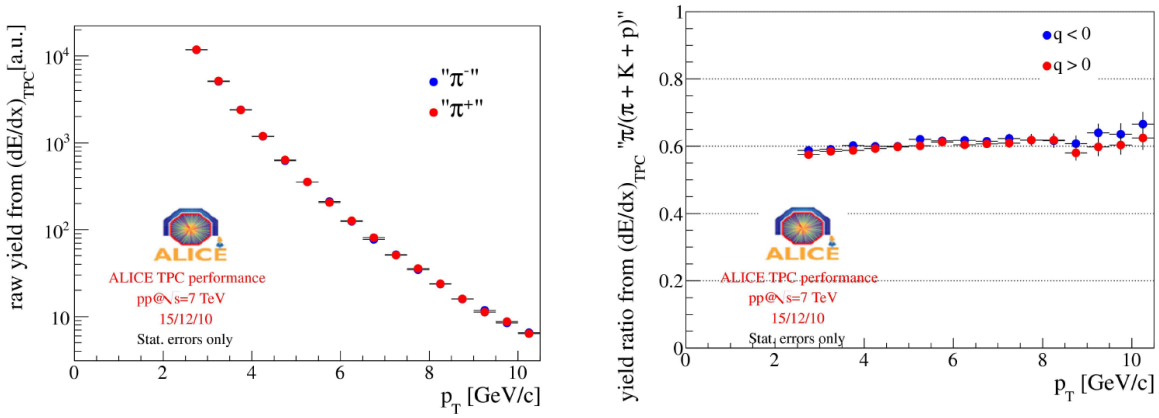

(a) The p_T spectra for charged pions.

(b) The ratio $\pi/(\pi + p + K)$.

Figure 4.8: The results from the dE/dx PID method.

4.4.1 Energy loss resolution

The dE/dx resolution is crucial for the PID, since this parameter sets the limit for how well you can separate the specific energy loss for the particles in different regions of momentum (or transverse momentum). In a dE/dx region where the different particle species overlap, i.e. at high p_T, the energy loss resolution is an important parameter to the identification process.

The energy loss resolution is a measure of how well determined the energy loss for a specific particle can be, and hence how well separated they are from other particles when PID is done. The energy loss resolution for the number of clusters of the track is seen in Fig. 4.9 [18]. When the track has a maximum number of clusters (159), the resolution is the best: $\sim$ 5%, which is better than the design value of $\sim$ 5.5% [8]. When averaged over all reconstructed tracks, this resolution is about 6.5% [8].

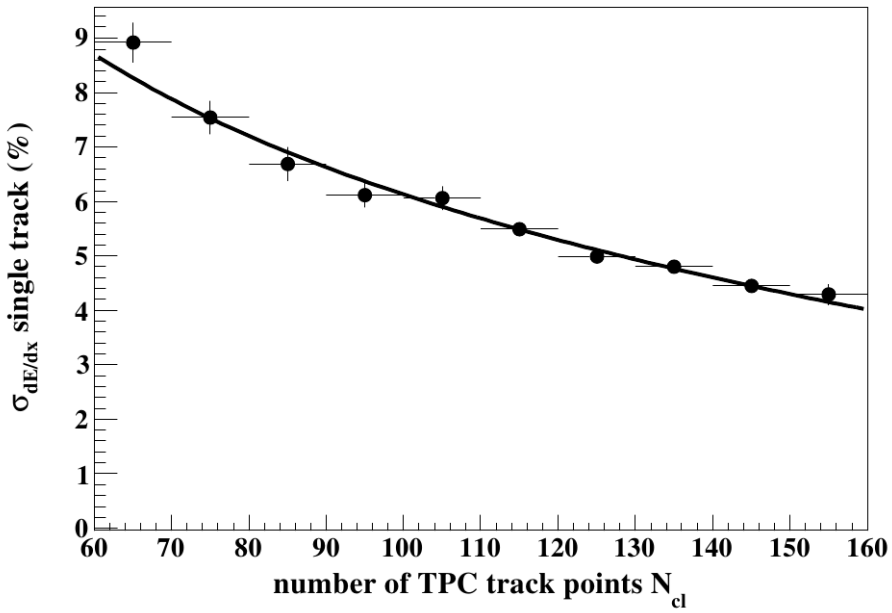

Figure 4.9: Dependence of the energy loss resolution on the number of clusters along the track, measured with cosmic tracks. [1].

Chapter 5

The practical part: FEC replacement and data taking

This thesis is in experimental physics, and laboratory work is an important part of my masters work which is hard to describe in the actual thesis. Working in a big experiment like ALICE means that I profit from the work of many others, like those designing and building the experimental setup, people who have built the analysis software package, and others who maintain, operate and calibrate detectors so that each detector gives properly calibrated information about each particle hit. Every collaboration analyzing data is expected to contribute to the "collective effort" by participating in such work. Often this work cannot be directly identified to the actual data in your own analysis as it may have been acquired during years of data taking.

I had the opportunity to be a CERN summer student in 2010 as a member of the TPC group in the ALICE experiment. This gave me good hands on experience with ALICE in general and the TPC in particular, which has given me the competence to contribute on several part of the experimental work. I have, during the course of the thesis, had the following tasks.

- TPC shifter during 2 weeks in October 2010.
- DQM shifter during one week in May 2011. This is one position in the 5 person shift crew, responsible for monitoring the quality of data taken by all detectors in ALICE and to take action (normally contacting the on call expert) in case data do not fullfil the quality criteria.
- FMD "on call subsystem expert" in two weeks of July 2011. This means to serve the shift crew with expertise help 24h per day in case problems arise with the FMD detector which the shift crew cannot solve. The FMD is a smaller detector than the TPC and the expert competence can be acquired by special training.
- In addition, I have been one of three persons trained and qualified to do actual repair work on the TPC electronics. This means to work inside the L3 magnet, which requires special training: confined space, working at heights and radiation protection. Such repair work took place for 3 weeks in the winter shutdown and during some of the technical stops since then. The repair work has been particularly interesting and I will describe it further.

5.1 TPC high voltage trips

When LHC started to run at higher intensities and luminosities, the TPC was triggered (gate open) at a higher rate (400-1000 Hz). At this rate, the HV trips started to occur frequently (several times per week, sometimes several per day).

Any gas filled avalanche detector (like the MWPC) has a certain risk that an unusually large avalanche develops into a spark when the gain is set at a high value, such that minimum ionizing particles shall be detected. Sometimes, highly ionizing particles may give too large avalanches which may develop into a spark causing the HV to trip because of the current limitation. So HV trips are normally occurring in MWPCs at some rate, which is dependent on the rate of particles traversing the detector. The problematic consequence here is that, with too large a probability, a HV-trip has lead to a damaged front end card (FEC) which in turn means 128 dead channels.

Since sparks are expected to happen, the readout electronics is equipped with input protection which shall protect the circuit. It is thus believed that the damage to front end electronics is caused by the HV trip itself – and not from the spark as such.

A HV trip happens when the current from the high voltage supply to the ROCs is above a certain threshold ($\sim$200 μA). If the threshold limit is exceeded, the power supply ramps down ($\sim$1 kV/s) to ensure safe operation. The ramping down of the HV induces a large negative current at the charge amplifiers which leads to a large negative voltage at the input transistor and a large voltage ($\sim$ kV) across the feedback transistor. The circuit at the PASA input can therefore be damaged.

The input protection circuit of the amplifier should protect for this, but if the current through the protection diodes becomes too large, they themselves can become damaged and permanent short circuits to ground (or supply voltage) instead of the temporary short circuits which they are supposed to be when acting as protection.

This happened only during colliding beams. 20% of the trips occurred when the gating grid was closed (i.e. while not triggering), and the remaining 80% when the gating grid was opened (i.e. triggering).

The actual reason for an FEC to get damaged is heavily discussed during the weekly TPC meetings. The HV trips themselves depend on voltage and amount of current causing a so called *streamer*. A wide opinion is that the FEC is broken due to the current streamer, but it is still under investigations. The required charge to kill an electronic channel would also cause a tripping chamber. A filter is mounted on the HV supply that almost prevents chamber trips. A run with reduced gain was used to experimenting with these filters in order to understand the trips, and the results was that using a voltage 50 V below the normal value, there was no problem. For streamer production there are thresholds which depend on voltage and deposited charge, and 50 V is also the threshold for streamer production and therefore argues that a trip is due to streamers. A trip does not have to cause a damaged card, but in some cases they do. The question still remains if the streamers occur due to the number of bunches in the beams, or the interaction rate – or both. Another question to be answered is how the FEC is damaged by the HV trips. Nevertheless, the broken FECs has to be replaced.

5.2 Activities during shutdown - FEC replacement

The 18 sectors are divided in an outer (OROC) and inner (IROC) read out chamber. The IROC and OROC each consists of three *partitions*, i.e. FEC rows read out by the RCU, with 18, 20, or 25 FEC in each partition (depending on the radial position of the partition). The partitions are divided into two branches.

Figure 5.1: Photos taken at P2 on the A-side of the ALICE-TPC during the FEC replacements: The IROC sectors on the A-side of the TPC with the cooling tubes, and low voltage supply for the FEC's.

Before an FEC can be replaced, the front end electronics (low voltage cables to the FEC's, the RCU with the fiber optics, and the busses) and the cooling of the FEE must be removed. Since lack of space, all FEC's on one side of the broken FEC on the branch must also be removed. One FEC has 6 kapton cables which connect to the FEC with a so called ZIF connector (Zero Input Force) and closed with a *lock* – approximately 1-2 mm wide, and another connector on the pad plane. To remove a card from the row of FEC's, the lock on the pad plane connector must be opened by a custom made tool which, basically, is a long hook. To help the eyesight (since it is very difficult to see the lock itself), we used a small camera on a long wire which could be placed near the lock.

When the broken FEC in a row is replaced, the FEC needs to be put back in place again; the kapton cable is placed in the lock and the lock is closed. To check that kapton cables are connected correctly, a test is performed by reading out an individual FEC with a portable DAQ system, replacing the RCU and the main ALICE DAQ. Test pulses sent to the wires in the chambers are read out, thus verifying the integrity of the connection. The data are monitored on a PC and the test shows if the kapton cable is connected to the pin in the

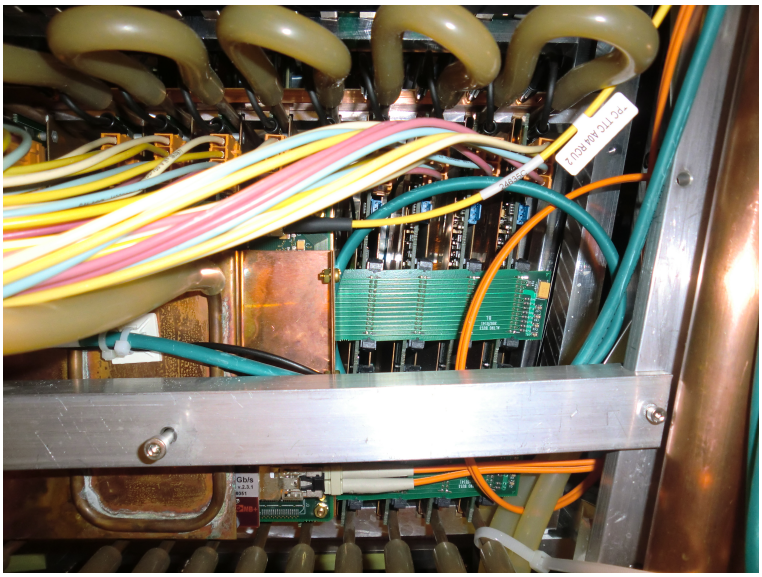

(a) The FEC's in one branch with the RCU connected to the buses.

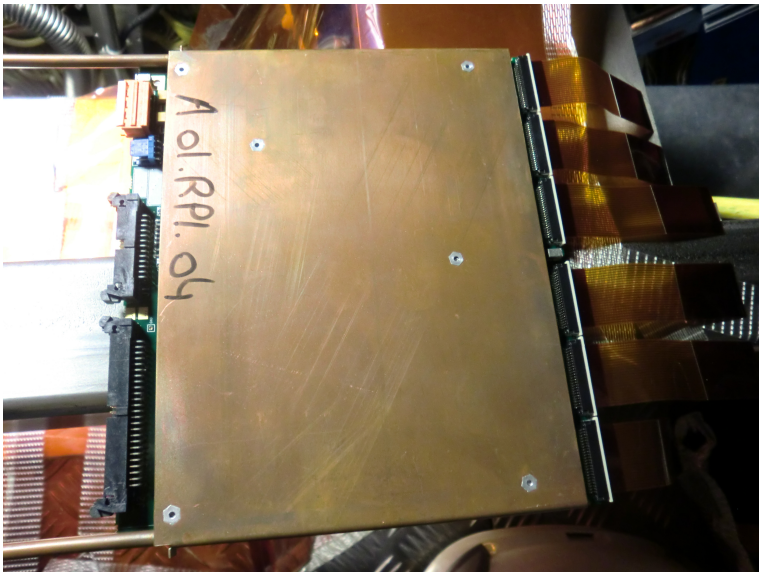

(b) One FEC with its copper cooling plate protection and connectors to the kapton cables. This particular one is from the sector 1 in the A-side (A01), readout partition 1 (RP1), card number 04.

Figure 5.2: Photos taken at P2 on the A-side of the ALICE-TPC during the FEC replacements.

connector to the padplane.

It is important to mention here that the time it takes to replace one FEC in an average difficult position (e.g. in the middle of a partition on a sector where the working position of your body is relatively free, and the safety harness does not disturb the motion of your arms too much) is long: it can take 1-2 days for one person performing all the preparing work of the sector, the FEC replacement itself, and the finishing work with putting back all services again and making the quality checks – and even 3 days for an FEC in the most difficult position. It is therefore extremely important that the problem with damaged cards is a priority of the TPC group, and that it is solved as soon as possible.

The work done at the last technical stop during July (which I also participated in), focused on a new idea regarding how to solve the problem with damaged FEC's, and to protect the FEE. The strategy was to reduce the stored energy by reducing the number of capacitors between wire and ground in the HV distribution box [18], seen in Fig. 5.3. This is done since it is believed that when the capacitor is discharged too fast after a spark, and all current flows directly to the FEC's. The impact on the performance is small due to the fact that the only effect is a negativly induced pulse to the surrounding wires, which is easily handled.

To reach the HV box, the whole FEC partition needed to be removed. This was done to 3 partitions during the last technical stop.

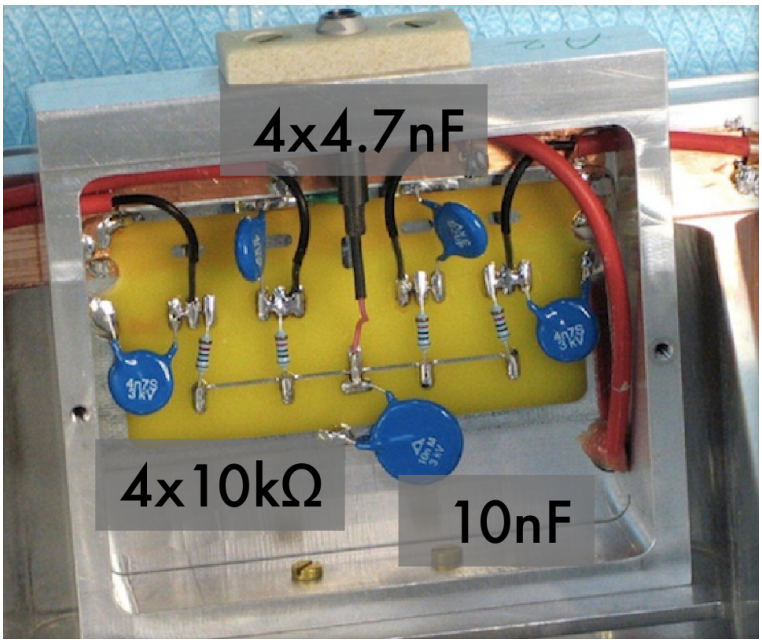

Figure 5.3: The HV distribution box with the capacitors. The four 4.7 nF capacitors are those which are removed[18]

Chapter 6

Analysis: K^0_S, Λ, and $\bar{\Lambda}$ spectra

This analysis is about identifying Λ, $\bar{\Lambda}$, and K^0_s from pp collision data, and to construct the p_T-spectra for these particles. The motivation of this study is to investigate the high p_T range, where pQCD holds. The fact that these V^0 particles are strange particles is of great interest when studying recombination and strangeness enhancement theories in PbPb collisions. When doing that, it is necessary to have baseline data from pp collisions where these effects is not expected to appear.

The method is to fit the invariant mass distributions of the V^0 particles, which is a statistical identification, to obtain the number of particles per p_T bin. To demonstrate that the method works, and to determine the correction factors, a MC study is carried out first. Then the method is applied to real data and V^0 PID is carried out after optimizing the method with various cuts and corrections.

6.1 ROOT - The analysis framework

To perform a stable analysis which can handle a large amount of data, the choice of analysis framework is important. In this analysis ROOT is used as the basic framework.

ROOT is an object-orientated offline computing framework written in C++. It was developed at CERN to handle high energy physics data, and it is a *framework* in the sense that it provides the user with plenty of high energy physics tools, like histograms and pre-defined fitting functions. The purpose of ROOT (or AliRoot specifically for ALICE data and simulations) is not only to handle Monte Carlo simulations, track reconstruction and data analysis with data from all experiments, and both types of collisions (pp and PbPb), but also to handle a large amount of data in an effective way. a common analysis framework is of course mandatory in a large collaboration, so that software routines can be shared, maintained, and certified.

One useful way of handling and storing data, which is used in this analysis, is to build a so called *tree*. A tree saves the objects, or variables, in a collective and structured (hierarchal) way in a ROOT file, i.e. each object is not written individually - which reduces the data volume and increases the access speed significantly.

6.2 Data

The input to the analysis is the data. There are two types of analyzable data: the Event Summary Data (ESD) and the Analysis Object Data (AOD). When the raw data are reconstructed, the output is so called ESD. The processing to ESD includes finding the position of the primary vertex, the reconstructed charged particle tracks, and the secondary vertex candidates [4]. When some global analysis cuts are taken into account, the data are marked as AOD. In this report, only ESD data are analyzed.

6.2.1 7 TeV Data

The data used in this analysis are from LHC10d (a certain period of LHC data taking, where LHC10d indicated that the runs are taken in 2010 at $\sqrt{s} = 7$ TeV). The input to the analysis is three runs from this period[1], with a total number of events of 7 530 921.

6.2.2 Monte Carlo Data

To be able to compare real data with something similar but generated in a controlled way, one uses *simulated data* generated via Monte Carlo (MC) event generators [4]. The MC generator produces the same particles as expected from a real collision, with the same properties (such as momentum, charge, and decay chain). The event generator describes the physics to the best of our present knowledge. Hopefully this is realistic for the large majority of the particles. The results of new predictions can be embedded in the event generator result.

The produced particles are propagated through the detectors ("tuned" in the same way as in the real detectors) by the detector simulation program GEANT, and will give hits[2] which are stored as raw data. The MC data are then treated in the exact same way as real data with the only difference that the particle types can be "revealed" after an analysis is done to compare the results. This is used to calculate correction factors for inefficiency, geometrical acceptance and other experimental shortcomings. Prior to an experimental study, in particular if it will require large amounts of the collaboration resources, one must demonstrate with simulations that the project is possible to pursue. The detector simulations in high energy physics experiments describe the detector response to a good precision.

The MC data used in this analysis are three runs[3] from LHC10d with matching conditions as for the real data, generated by PYTHIA, with a total number of events of 9 615 078.

In the following text the naming convention described here is used:

- Data: the real data from pp collisions (in the figures called DT).
- TRUTH$_{gen}$: the data from the *generator* level of the MC data production, i.e. where all initial properties of the particles are known (PID, momentum etc.).
- TRUTH$_{det}$: the MC data after the TRUTH$_{gen}$ particles have been propagated through the detector, i.e. where all properties of the particles are still known, but have now been changed since the detector is affecting the particle properties.
- MC: the MC data when treated as real data, i.e. after reconstruction.
- Corrections are normally MC/TRUTH$_{gen}$.

[1] Run 126425, 126432, 126437

[2] Energy deposition at a given point and time [4].

[3] Run 002, 003, and 004

6.3 V^0 candidate selection

The decay vertex of a V^0 particle has a V shape (hence the name), and the decay particles are bent into opposite directions by the magnets since the V^0 particle is neutral and thus the decay products have opposite charge [6]. The V^0 particles are identified by reconstructing the secondary vertex caused by their decay products. To distinguish whether a particle close to the secondary vertex is a true daughter particle from the V^0 weak decay, the particle needs to fulfill some requirements to be selected as a true daughter particle associated with that particular V^0 particle.

To reconstruct a V^0 particle, a so called V^0 finder algorithm is used to reconstruct the secondary vertex. On top of this, several other cuts are done to be able to have a clean sample of V^0 particles. The analysis of the cut optimization is described in this section, as well as the effect of the cuts on the invariant mass distribution.

6.3.1 The V^0 finder

There are two V^0 finder algorithms: the offline and the online. The online V^0 finder operates on the fly, i.e. during the track finding. It checks the likelihood of having a V^0 when adding clusters to a track. The online V^0 finder has the advantage that all the reconstruction information is available when making the decision if it is a V^0 or not, while the advantage of the offline V^0 finder is that it can be run over the data several times, is reproducible, and it knows all tracks.

The offline V^0 finder is the one used in this analysis and it is implemented after the track finding algorithm. It combines two tracks depending on the vertex topology criteria, the Distance of Closest Approach of the secondary tracks (DCA_s).

The V^0 finder selects the V^0 particles before an analysis is made. It starts by selecting secondary tracks, i.e. tracks with a large distance of closest approach with respect to the primary vertex (DCA_p) [5, 8], see Fig. 6.1. Here, all combinations of oppositely charged secondary tracks are considered. The daughter tracks are accepted if the daughters' $DCA_s <$ 0.5 cm, see Fig. 6.1. Since the tracks are reconstructed with an uncertainty in position, the DCA_s will have a finite length, i.e. in a reconstruction with no uncertainty this length would be 0, but due to the uncertainty, the DCA_s is larger than 0.

This figure also shows variables which are useful to introduce before the next sections, e.g. the pointing angle between the reconstructed V^0 momentum vector and the extrapolated V^0 line of flight before the decay.

6.3.2 Further selection criteria

Only events with the z vertex (the distance between the primary vertex position and the nominal collision point) less than 10 cm [8] are considered in order to minimize the amount of tracks at the edge of the TPC detection volume which can effect the efficiency negatively. Additional, a phi cut is applied to remove inefficient areas near the TPC sector edges. A track is required to have at least $|\eta| < 0.8$, which is the acceptancy value. This makes the track have the whole projected length in the TPC and, again, the risk of efficiency loss due

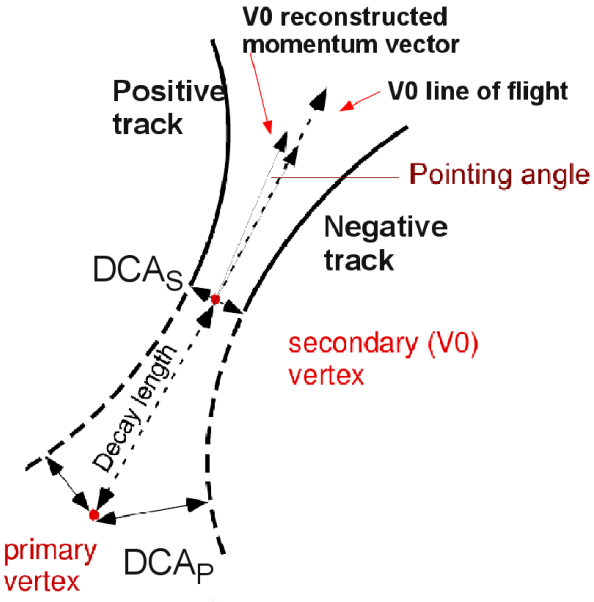

Figure 6.1: V^0 vertex topology where DCA, pointing angle and the primary vertex are shown.

to detector boundaries are minimized. A track should also have at the minimum 70 clusters, a reasonable χ^2 per cluster in the track fitting, and at least two hits in the ITS (with one of these hits in the SPD).

In general, as few cuts as possible is a good idea since cuts can induce a bias and the physics results can be affected in the end. An example of a cut which induces bias is described in Sec. 6.3.6.

6.3.3 V^0 reconstruction

After the V^0 finding process and the additional cuts, the identification of the V^0 particles starts, i.e. which of the V^0 particles are Λ's, $\bar{\Lambda}$'s, and K^0_s's. This is described in the following.

The momentum vector components of each daughter particle are known (from the tracking), i.e. $p_x^{+/-}$, $p_y^{+/-}$, and $p_z^{+/-}$ (where + indicates the positively charged daughter particle, and - is the negatively charged daughter). The momentum components of the V^0 particle can then be obtained by

$$p_i^{V^0} = p_i^+ + p_i^- \tag{6.1}$$

where i can be either the x, y, or z component of the momentum vector.

Masses are then assumed for the daughters of the V^0 particles (in e.g. the Λ case a proton and negative pion is assumed, see Eq. 6.4), and the energy of the daughters, $E^{+/-}$, can be obtained, i.e. the whole 4-vector ($E^{+/-}$, $p_x^{+/-}$, $p_y^{+/-}$, $p_z^{+/-}$). The energy of the V^0 particle can be calculated by

$$E^{V^0} = E^+ + E^- \tag{6.2}$$

From this, the invariant mass of the V^0 particle can be calculated with

$$m_{V^0} = \sqrt{(E_1 + E_2)^2 - (\vec{p_1} + \vec{p_2})^2} \tag{6.3}$$

The different variables for the V^0 particles are sorted in a tree structure where, for each V^0 particle, the mass difference can be obtained, defined by

$$\Delta m_\Lambda = (m_{V^0} \text{ assuming } p + \pi^-) - (m_\Lambda^{PDG}) \tag{6.4}$$

$$\Delta m_{\bar{\Lambda}} = (m_{V^0} \text{ assuming } \bar{p} + \pi^+) - (m_{\bar{\Lambda}}^{PDG}) \tag{6.5}$$

$$\Delta m_{K_s^0} = (m_{V^0} \text{ assuming } \pi^+ + \pi^-) - (m_{K_s^0}^{PDG}) \tag{6.6}$$

where m^{PDG} is the mass of the particle as stated in the Particle Data Group (PDG), and the m_{V^0} is the invariant mass.

After these calculations have been performed, the invariant mass distribution of the V^0 particles have a background, see Fig. 6.2(a) and 6.2(b) where the invariant mass distribution for Λ and K_s^0 is shown[4]. The background consists of other V^0's that gets similar masses due to accidental V^0 topology, seen in Fig. 6.2(c) where the $\Delta m_{K_s^0}$ is plotted versus Δm_Λ to demonstrate that the regions overlap. Other sources to the background is tracks that are wrongly associated, i.e. do not point to vertex, and tracks that are not V^0's.

In order to do Λ, $\bar{\Lambda}$, and K_s^0 p_T-spectra, the background in the invariant mass distribution needs to be understood and reduced. The background for Λ and $\bar{\Lambda}$ is larger than the background of K_s^0, seen in 6.2. It, however, turns out that similar cuts can be made for these three different particles. Later in this section, these cuts are explained in detail.

6.3.4 Data tree

The available information in the data tree for each particle is, among others, the variables (note that some of these are not explained yet, but will be in the following analysis):

- Mass related: Δm_Λ, $\Delta m_{\bar{\Lambda}}$, $\Delta m_{K_s^0}$, and Δm_γ, where for Δm_γ two electrons are assumed.
- Momentum related: p and p_T of the V^0 particle, and p, p_T and p_T^{Arm} for the daughter particles.
- Topology related: α, decay radius, decay length, and $cos($ pointing angle$)$ for the V^0 particle, and distance of closest approach of the daughter particles.
- Detector related: number of clusters and dE/dx of the daughter particles.
- Angle related: ϕ and η for both mother and daughter particles.
- Monte Carlo related: PID for TRUTH$_{det}$

[4]The invariant mass distribution for $\bar{\Lambda}$ is similar to the Λ distribution

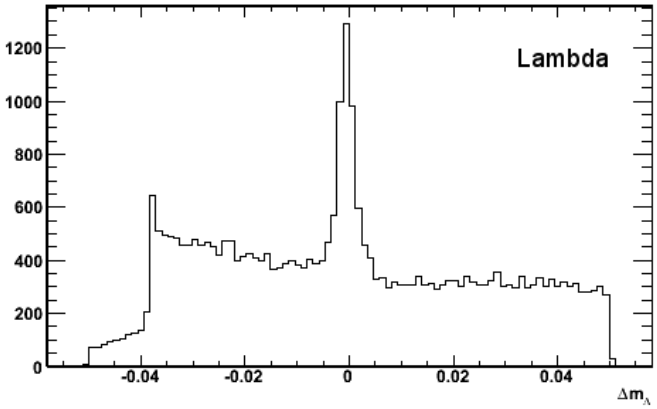

(a) Δm_{Λ} distribution from data showing a peak centered at 0 and a relatively large background.

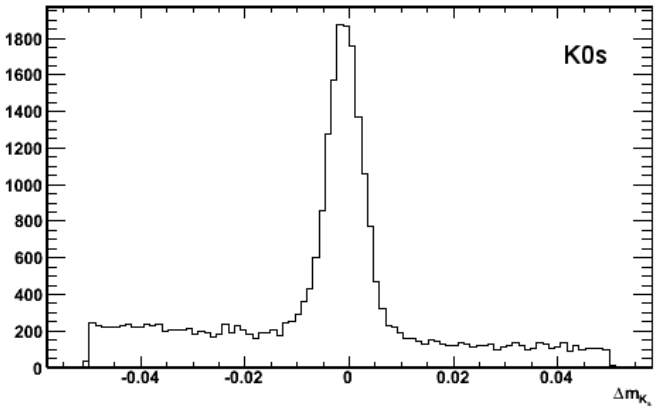

(b) $\Delta m_{K_s^0}$ distribution from data with a peak at 0 and a background smaller than the Λ background.

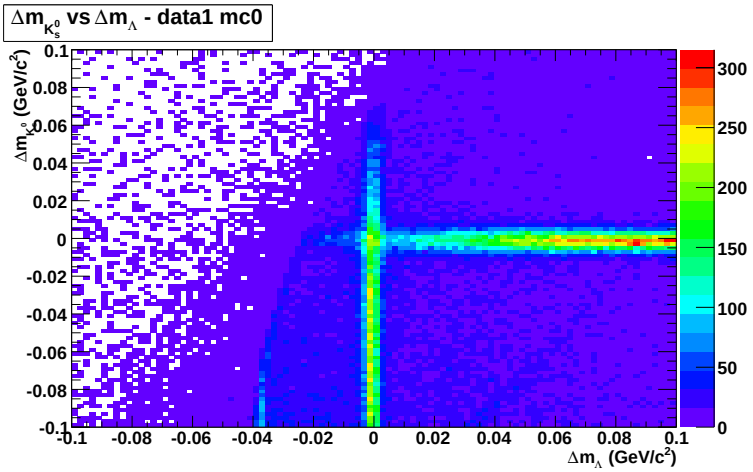

(c) $\Delta m_{K_s^0}$ versus Δm_{Λ} for data demonstrates that the background consists of other V^0's that gets similar masses since the regions overlap.

Figure 6.2: Invariant mass background when no cuts are applied, data.

6.3.5 The mass cut

In the analysis, Λ is required to have $|\Delta m_\Lambda| < 10\,\mathrm{MeV}/c^2$ and $|\Delta m_{K_s^0}| > 10\,\mathrm{MeV}/c^2$, while for the K_s^0 the mass cut is $|\Delta m_{K_s^0}| < 10\,\mathrm{MeV}/c^2$ and $|\Delta m_\Lambda| > 10\,\mathrm{MeV}/c^2$, i.e. the particle not considered should be at least $10\,\mathrm{MeV}/c^2$ away from the particle that is considered. These are from now on referred to as *exclusive mass cut*, whereas another cut that will also be made later is the *inclusive mass cut*, where only the inclusive part of the previous described cut is considered, e.g. $|\Delta m_\Lambda| < 10\,\mathrm{MeV}/c^2$ for selecting Λ's.

In Fig. 6.4(a) Δm_γ is plotted for TRUTH_{det} Λ's with the Λ inclusive mass cut ($\Delta m_\Lambda < 10\,\mathrm{MeV}/c^2$) together with the *real* Δm_γ distribution, where two TRUTH_{det} electrons are recombined (conversion electrons). In this figure it is hence seen that there is a region, $\Delta m_\gamma < 100\,\mathrm{MeV}/c^2$, where conversion electrons can be identified as Λ. Therefore, a cut is also made for the Δm_γ, where $\Delta m_\gamma > 100\,\mathrm{MeV}/c^2$. Fig. 6.4(b) shows that the conversion electrons that are identified as K_s^0 is well separated from the TRUTH_{det} K_s^0.

In Fig. 6.2(c) the $\Delta m_{K_s^0}$ is plotted versus Δm_Λ to demonstrate that the regions indeed overlap and a cut is necessary. In Fig. 6.3, the same plot is shown, but now with the cuts for selecting Λ, and the background is significantly reduced seen by the fact that most of the high density K_s^0 (the horizontal area) and conversion electrons (the edge of the high density particle region) areas are removed. These cuts are chosen to maximize the statistics and purity (to minimize the background).

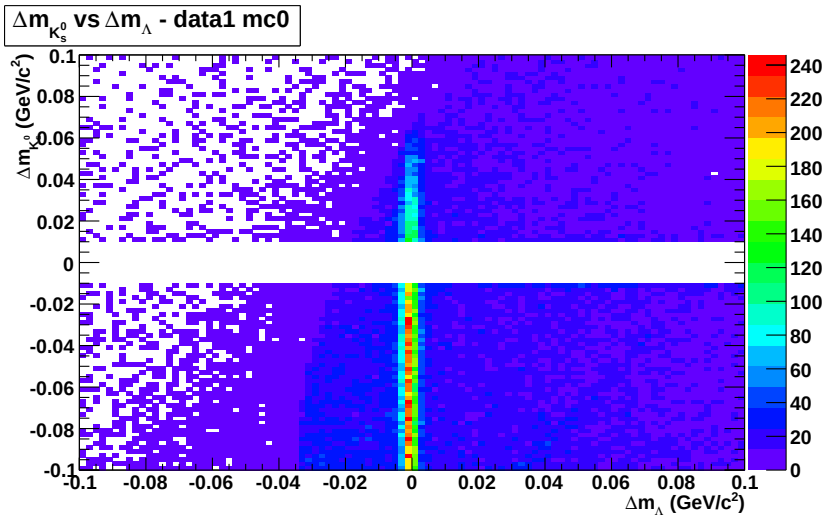

Figure 6.3: $\Delta m_{K_s^0}$ versus Δm_Λ for data with the mass cuts used for Λ, i.e. $|\Delta m_{K_s^0}| > 0.01$ GeV$/c^2$ and $\Delta m_\gamma > 0.1$ GeV$/c^2$, which is the first part of the exclusive mass cut.

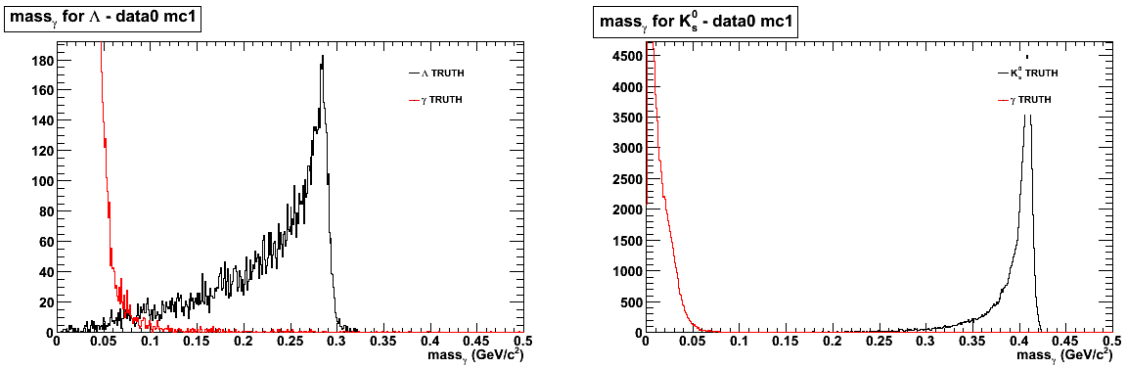

(a) Δm_γ, TRUTH$_{det}$: Λ. (b) Δm_γ, TRUTH$_{det}$: K^0_s.

Figure 6.4: The γ part of the exclusive mass cut.

6.3.6 The pointing angle cut

To reduce the background further, some more cuts need to be done. The pointing angle is the collinearity angle between the reconstructed V^0 momentum, associated to the V^0 candidate (calculated as the sum of the track momenta extrapolated to the position of the DCA [5]), and the direction from the V^0 to the decay vertex [6], see Fig. 6.1, i.e. the reconstructed V^0 momentum should point back to the primary vertex. Ideally, cosine of this angle should be 1, this would then mean that the reconstructed V^0 momentum vector is equal to the direction of the V^0 to the decay vertex, and that these two vectors overlap. This is however not true due to finite resolution, so a cut has to be made so that cosine of the pointing angle is close to 1. The cut used in the following analysis is $cos(\text{pointing angle}) > 0.99$ for all three V^0 particles.

In Fig. 6.5, the distribution of the cosine of the pointing angle can be seen, motivating the cut of $cos(\text{pointing angle}) > 0.99$. In Fig. 6.5(b) it is seen that if a cut of the $cos(\text{pointing angle})$ would be higher than 0.99, some of the low p_T tracks would have been cut away, and a p_T bias would have been introduced.

6.3.7 The distance of closest approach

The distance of closest approach (DCA_p) is the closest distance from the primary vertex to the daughter particle track, see Fig. 6.1. As seen in Fig. 6.6, there are several tracks with a DCA_p below 0.1 cm, which are cut away with the DCA_p cut, since these are too close to the primary vertex for being daughters of the V^0 particle.

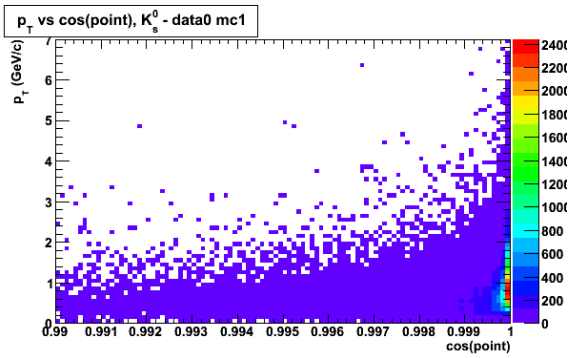

(a) p_T versus cos(pointing angle) for K_s^0, TRUTH$_{det}$.

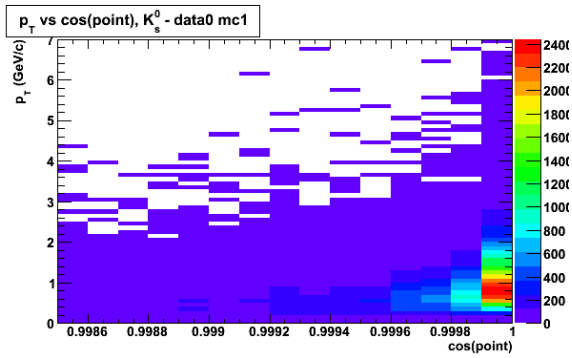

(b) p_T versus cos(pointing angle) for K_s^0, TRUTH$_{det}$.

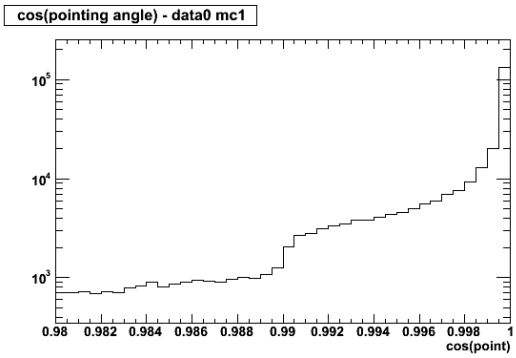

(c) cos(pointing angle) distribution for MC. Note the logarithmic scale.

Figure 6.5: The cos(pointing angle) distribution which motivates the cut of cos(pointing angle) > 0.99.

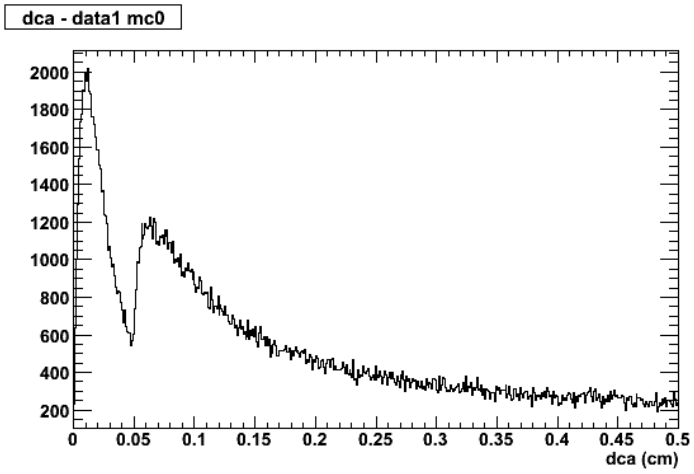

Figure 6.6: The DCA_p distribution which motivates the cut DCA_p>0.1 cm.

6.3.8 The Armenteros-Podolanski distribution

The Armenteros-Podolanski distribution (from now on called the *AP* distribution) is a kinematic way to select K^0_S, Λ and $\bar{\Lambda}$ from the V^0 daughters information, i.e. by looking at the kinematics of the decay, and by applying cuts in this topology, the V^0 particles can be distinguished. In an AP plot, the quantity p_T^{Arm}, which is the transverse momentum of one of the decay particles (as by conservation of momentum both are the same) relative to the V^0 momentum [6], is plotted versus α, defined as follows

$$\alpha = \frac{p_L^+ - p_L^-}{p_L^+ + p_L^-} \tag{6.7}$$

where p_L is the longitudinal component of the total momentum vector for the daughter particle relative to the direction of the V^0 momentum vector [5], i.e. α is the asymmetry of longitudinal momenta of both decay particles [6]. These variables can be seen in Fig. 6.7.

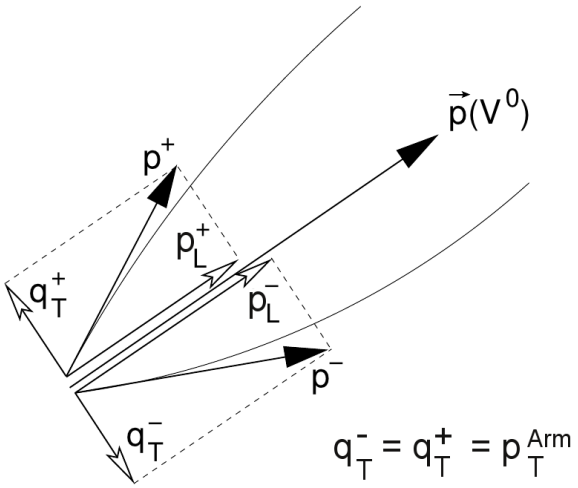

Figure 6.7: Variables for the AP distribution: the transverse and longitudinal momentum components of the positively and negatively charged track, with respect to the direction of the reconstructed V^0 momentum. Figure taken from [15].

The K^0_S, Λ, and $\bar{\Lambda}$ particles can be distinguished in the AP distribution since the signals from the different particles are divided up in bands forming an ellipse, see Fig. 6.8. The AP distribution is hence a method of analyzing the kinematics of the V^0 decays without identifying the daughter particles, and it is a convenient way of identifying these particles. In this analysis, the AP distribution is used for visualizing the cleanness of the samples after the cuts described earlier is applied. A cut in the AP distribution itself can also be done, but is not considered here since it is also contained in the mass cuts.

In Fig. 6.8, the different V^0 particle bands can be seen in the distribution, where the K^0_S band is located at high p_T^{Arm}, with the peak at $p_T^{Arm} = 0.206$ GeV/c since the maximum (derived below) can be reached if all the energy of the decay goes into the transverse momenta

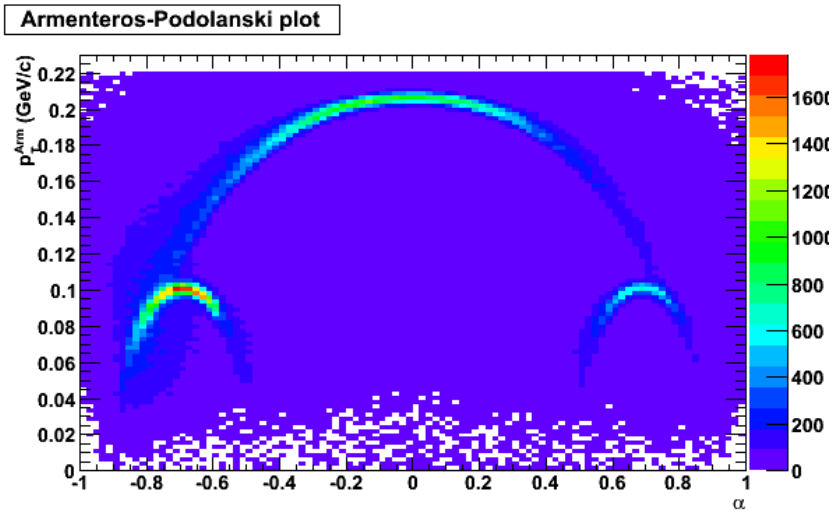

Figure 6.8: The AP distribution for data where K_S^0, Λ, and $\bar{\Lambda}$ particles can be distinguished. The K_S^0 band is located at high p_T^{Arm} and centered at $\alpha = 0$. The Λ and $\bar{\Lambda}$ bands have lower p_T^{Arm} and are centered around $\alpha = 0.691$ and $\alpha = -0.691$ respectively.

of the decay particles. In this case, it means that $p_T^{daughter} = p_T^{Arm}$, and that the daughters transverse momenta are equal to their momentum in the rest frame of the mother particle, which is derived below (and is hence also a derivation for the maximum p_T^{Arm}), where index 1 and 2 refers to the daughter particles, and M refers to the mother particle. The derivation starts by defining the four momentum:

$$p_1^2 = E_1^2 - \bar{p}_1^2 = m_1^2 \text{ and } p_2^2 = E_2^2 - \bar{p}_2^2 = m_2^2 \tag{6.8}$$

and since

$$p_2 = p_M - p_1 \;\rightarrow\; p_2^2 = p_M^2 + p_1^2 - 2p_M p_1 \tag{6.9}$$

where p is the four momentum, we have

$$m_2^2 = m_M^2 + m_1^2 - 2(E_1 E_M - \bar{p}_M^2 \bar{p}_1^2) \tag{6.10}$$

where E is the energy of the particle. Now, since we want to calculate this in the center of mass frame, the mother particle is at rest, meaning that $p_M = 0$ and $E_M = m_M$ and Eq. 6.10 becomes

$$m_2^2 = m_M^2 + m_1^2 - 2(E_1 m_M) \tag{6.11}$$

and thus

$$E_1 = \frac{m_M^2 + m_1^2 - m_2^2}{2m_M} \tag{6.12}$$

Inserting $E_1^2 = m_1^2 + \bar{p}_1^2$ and rearranging we obtain

$$|\bar{p}_1| = \frac{\sqrt{[m_M^2 - (m_1 + m_2)^2][m_M^2 - (m_1 - m_2)^2]}}{2m_M} = p_T^{Arm,max} \tag{6.13}$$

When inserting the values for the masses from Tab. 2.1, it is seen that

$$p_{T,K_s^0}^{Arm,max} = 0.206 GeV/c \tag{6.14}$$

$$p_{T,\Lambda}^{Arm,max} = 0.101 GeV/c \tag{6.15}$$

seen in Fig. 6.8. The K_S^0 band is centered at $\alpha = 0$ since the decay of K_S^0 is two equally heavy pions, and hence carries the same momenta.

The Λ and $\bar{\Lambda}$ bands have their maximum $p_T^{Arm} = 0.101$ GeV/c at lower values due to the lower Q-value, and the centers of the Λ and $\bar{\Lambda}$ bands are shifted to $\alpha = 0.691$ and $\alpha = -0.691$ respectively since the daughter particles have different mass; the (anti-)proton carries a higher momentum than the pion [15], due to the Lorentz boost. Generally, for a large value of α, one of the decay particles needs to have a large longitudinal momentum, resulting in a small value of p_T^{Arm}, which explains the shape of the bands.

As can be seen in the AP distributions is Fig. 6.9, there are not only K_S^0, Λ, and $\bar{\Lambda}$, but also a significant fraction of the reconstructed V^0 comes from γ conversion in the detector material (from e^+ and e^- pairs). This can clearly be seen in the Armenteros-Podolanski distribution. The γ conversions are located at very low p_T^{Arm}. This, and other background, is significantly reduced by applying the cuts described in Sec. 6.3.5, 6.3.6, and 6.3.7.

In Fig. 6.9 all V^0 particles, γ conversion electrons and background is shown in the AP distribution for data, MC, TRUTH$_{det}$, plotted with no inclusive mass selections or cuts. Fig. 6.9 demonstrates that, in fact, the background is not homogeneously distributed as it is slightly shifted to negative α. What causes this is unknown, but the effect is that it appears to be more $\bar{\Lambda}$'s that Λ's since the $\bar{\Lambda}$'s are riding on top of a larger background. Doing only an inclusive mass cut, i.e. selecting a mass window for the particle, will not reduce a lot of background, neither will it reduce the inhomogeneity of the background (Fig. 6.10 shows the distribution with inclusive mass selections on K_S^0 and Λ but no other cuts). This, however, is nothing that affects the analysis since it is also seen in MC and TRUTH$_{det}$, indicating that it is nothing special for the data. It will be even less of a problem since this effect is reduced significantly when performing the cuts.

In Fig. 6.10 it is also seen that the γ conversion electrons are removed for the K_S^0, but not for $\bar{\Lambda}$ and Λ, when applying the inclusive mass cut. This is explained by Fig. 6.4 shown earlier, i.e. for the $\bar{\Lambda}$ and Λ there is a region where they can have the same mass as reconstructed γ conversion electrons, but for the case of K_S^0 there is no such region. The γ conversion background is reduced by applying all cuts.

Fig. 6.11 shows the distribution for data, MC, and TRUTH$_{det}$ with the exclusive (which also includes the inclusive) mass cut, the pointing angle cut, and the DCA_s cut described earlier, i.e. all the cuts. When the three cuts are applied, they efficiently reduce the background and it is now more evenly distributed over the whole α region (even though the effect does not fully dissappear).

The figures discussed above is a first check of that the cuts are reasonable and that they take away only unwanted background, since the particle regions are restored after the cuts.

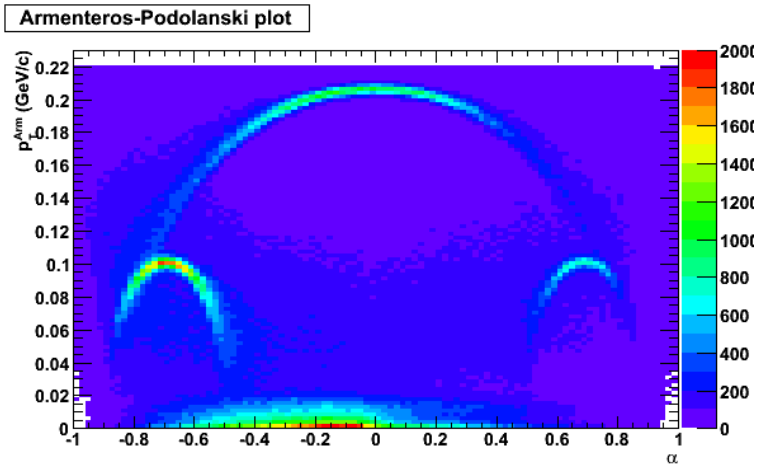

(a) Data.

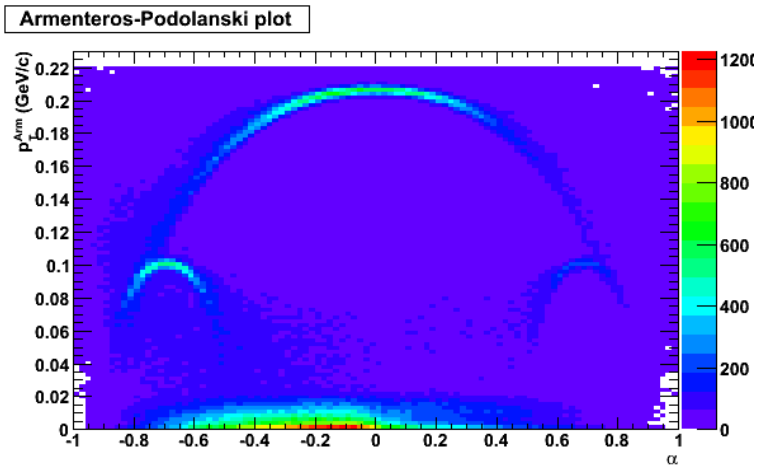

(b) MC.

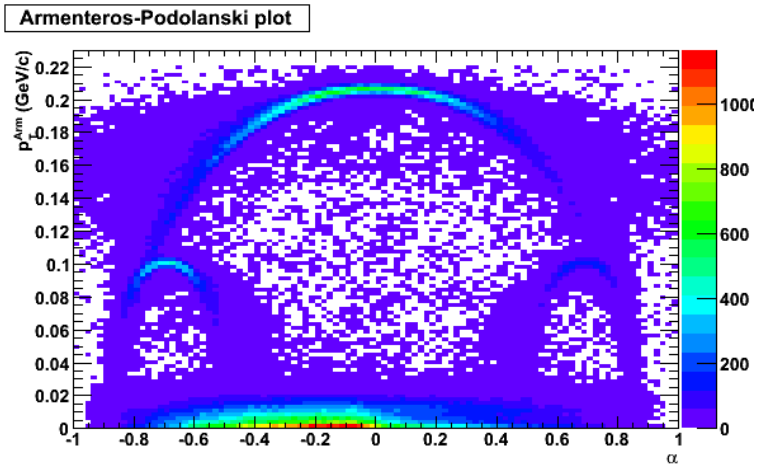

(c) TRUTH$_{det}$ Λ, $\bar{\Lambda}$, K_s^0, and γ particles.

Figure 6.9: No cuts or mass selection on K_s^0 or Λ: all V^0 particles, γ conversion electrons and background is shown.

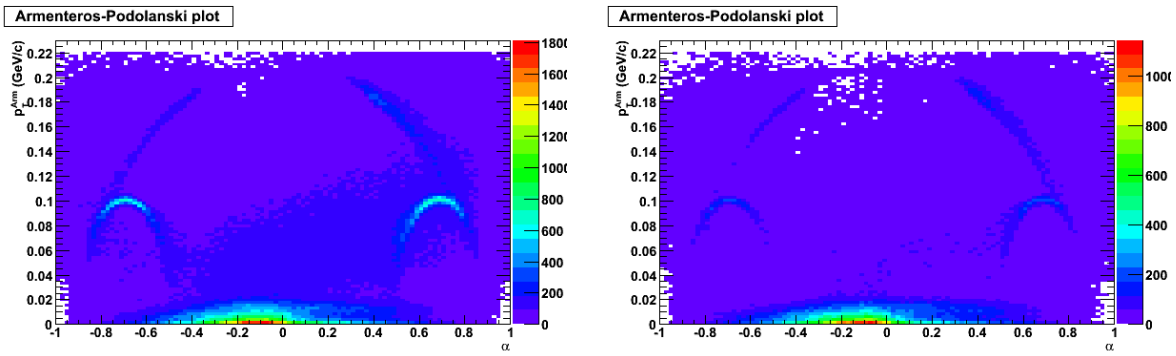

(a) Λ, data.

(b) Λ, MC.

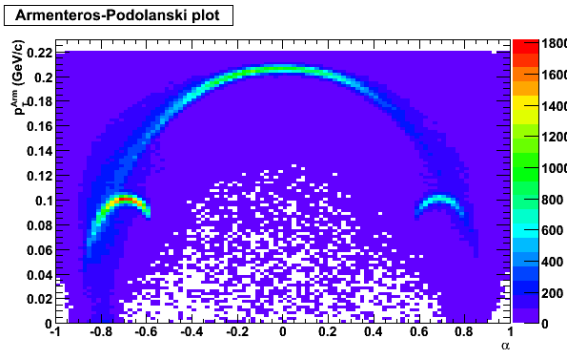

(c) K_s^0, data.

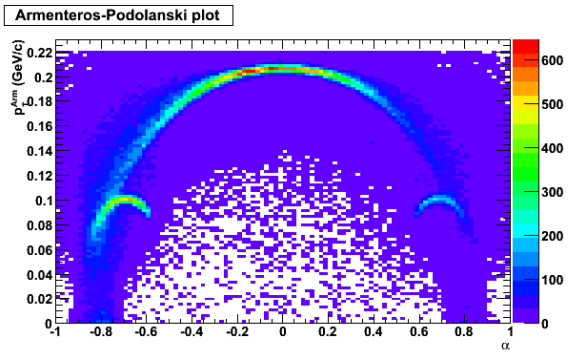

(d) K_s^0, MC.

Figure 6.10: Inclusive mass cut.

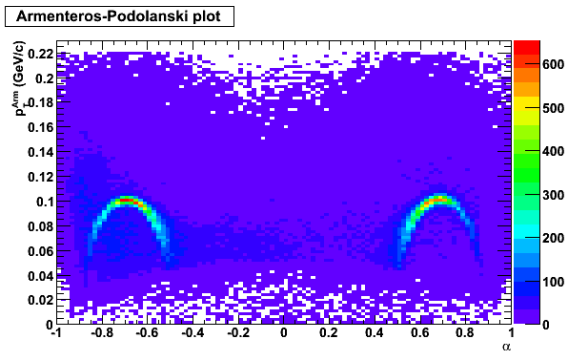

(a) Λ and $\bar{\Lambda}$, all cuts, data.

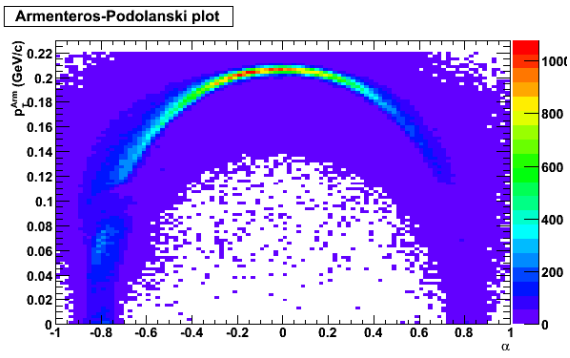

(b) K_s^0, all cuts, data.

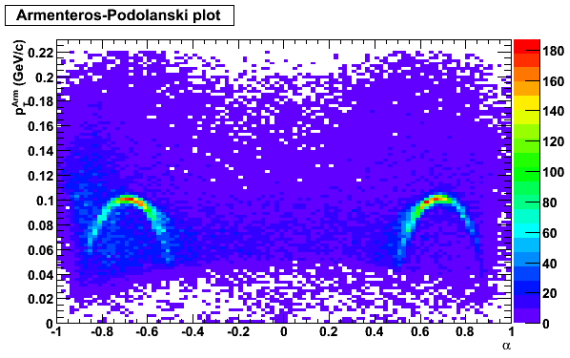

(c) Λ and $\bar{\Lambda}$, all cuts, MC.

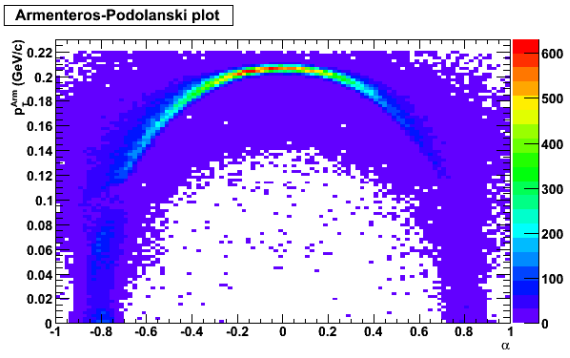

(d) K_s^0, all cuts, MC.

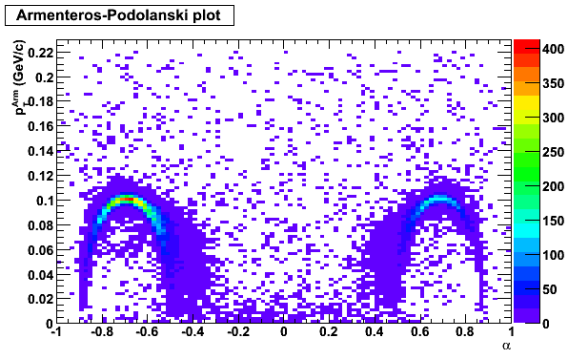

(e) TRUTH$_{det}$ Λ and $\bar{\Lambda}$ particles.

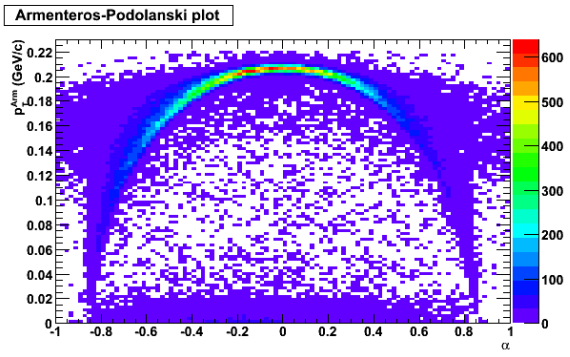

(f) TRUTH$_{det}$ K_s^0 particles.

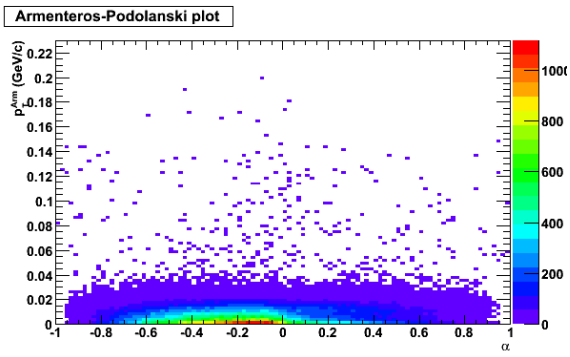

(g) TRUTH$_{det}$ reconstructed γ particles.

Figure 6.11: The AP distributions for clean particle samples.

6.3.9 The effect of the cuts on the invariant mass distribution

Another check to see if the three cuts have a good impact on the data, in the sense that it only reduces background, and do not decrease the statistics too much, is done in the following way.

In Fig. 6.12 and 6.13, an example is shown of the invariant mass distribution appearance for Λ and K_s^0 in the p_T bin 1.1-1.2 GeV/c for no cut (fig 6.12(a), 6.13(a)), mass cut (fig 6.12(b), 6.13(b)), pointing angle cut (fig 6.12(c), 6.13(c)), DCA_s cut (fig 6.12(d), 6.13(d)), and all three cuts together (fig 6.12(e), 6.13(e)), from now on referred to as *all cuts*. From the figures it is clear that these three cuts reduce the background and keep a reasonable high statistics. The same cuts are used for all three V^0 particles.

Other cuts that were studied but not taken into account are the decay length, decay radius, and the ncl. These turned out either to have no effect on the background, or too large loss in statistics.

It may be different for heavy ion data as the combinatorial background is more problematic which may lead to other optimizations in the cuts.

6.3.10 The lifetime distributions

To make a last quality check of the V^0 selections, and to see if Λ and K_s^0 can be separated by the described cuts, a lifetime distribution plot is done for MC, where all the selection criteria and cuts are used, as well as an additional momentum cut (1<p<6 GeV/c) of the mother particle. The distribution can be seen in Fig. 6.14, where $c\tau$ (given in cm) is defined as

$$t_{lab} = \frac{L_{decay}}{\beta} \tag{6.16}$$

since $L_{decay} = \beta t_{lab}$. Here, c is the speed of light, $\beta = v/c$ (where v is the particle speed), L_{decay} is the decay length (i.e. the distance between primary and V^0 vertex), and t_{lab} is the lifetime of the particle in the lab frame. To go from the lab to the center of mass (CM) frame, t_{lab} needs to be divided by $\gamma = 1/\sqrt{1-\beta^2}$

$$c\tau_{CM} = c\tau = \frac{t_{lab}}{\gamma} = \frac{L_{decay}}{\beta\gamma} = \frac{mL_{decay}}{p} \tag{6.17}$$

since $\beta\gamma = p/m$, where p is the momentum and m is the mass of the particle.

The distributions are fitted with exponential functions and $c\tau$ is extracted from the fit. The results show a $c\tau = 9.54$ cm for Λ and $c\tau = 2.84$ cm for K_s^0, where the PGD values are 7.89 cm and 2.68 cm respectively. The values are in the right order of magnitude (better for K_s^0 than for Λ, since Λ can come from Xi decays which makes the decay length looks longer since the Xi is not registered) – and since this is just a quality check – and since it is clearly seen that the V^0's can be separated in this way – this is enough.

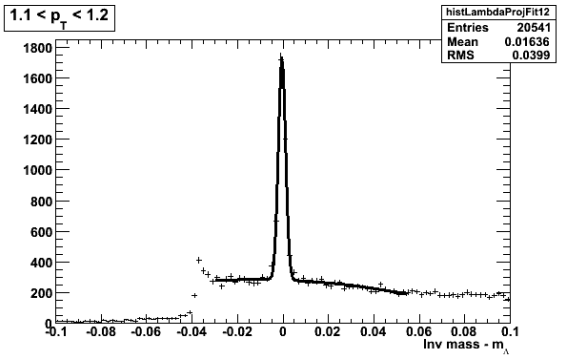

(a) Δm_Λ, no cut.

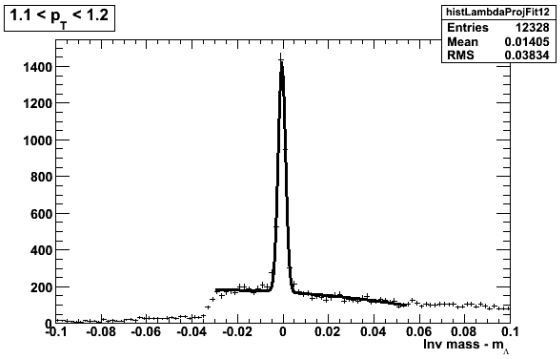

(b) Δm_Λ, mass cut.

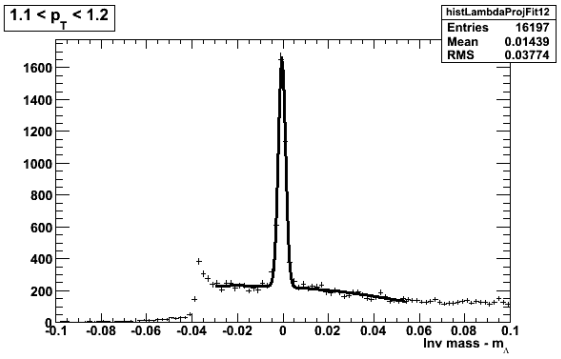

(c) Δm_Λ, pointing angle cut.

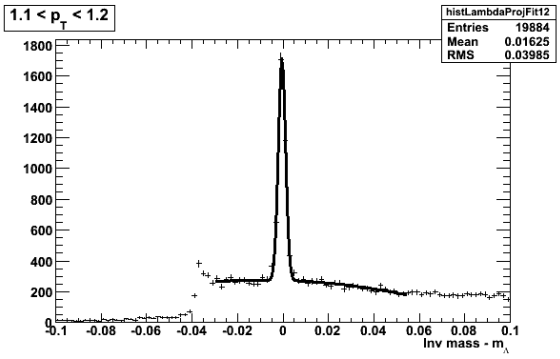

(d) Δm_Λ, dca of daughters cut.

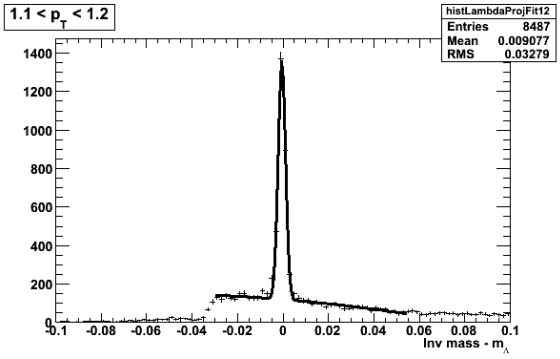

(e) Δm_Λ, all cuts.

Figure 6.12: The different cuts applied to the Λ invariant mass distribution for data in the p_T bin 1.1 - 1.2 GeV/c.

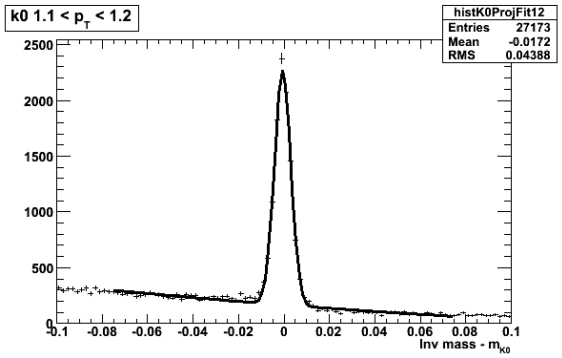

(a) $\Delta m_{K_s^0}$, no cut.

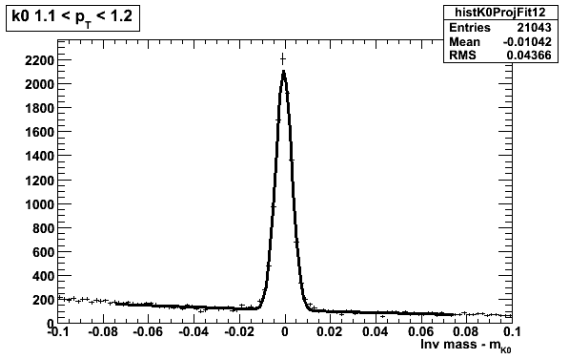

(b) $\Delta m_{K_s^0}$, mass cut.

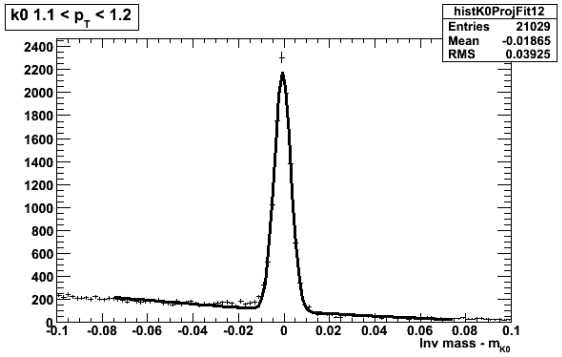

(c) $\Delta m_{K_s^0}$, pointing angle cut.

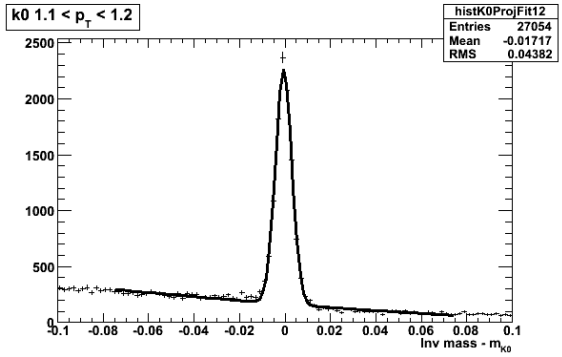

(d) $\Delta m_{K_s^0}$, DCA_s of daughters cut.

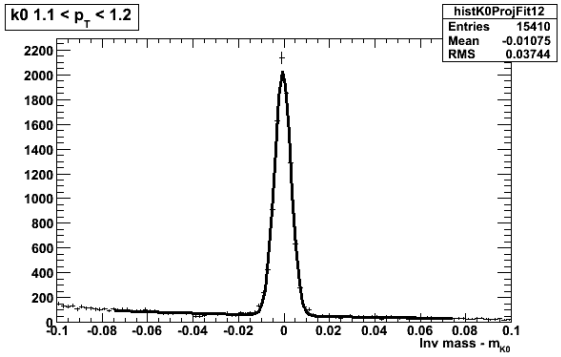

(e) $\Delta m_{K_s^0}$, all cuts.

Figure 6.13: The different cuts applied to the K_s^0 invariant mass distribution for data in the p_T bin 1.1 - 1.2 GeV/c.

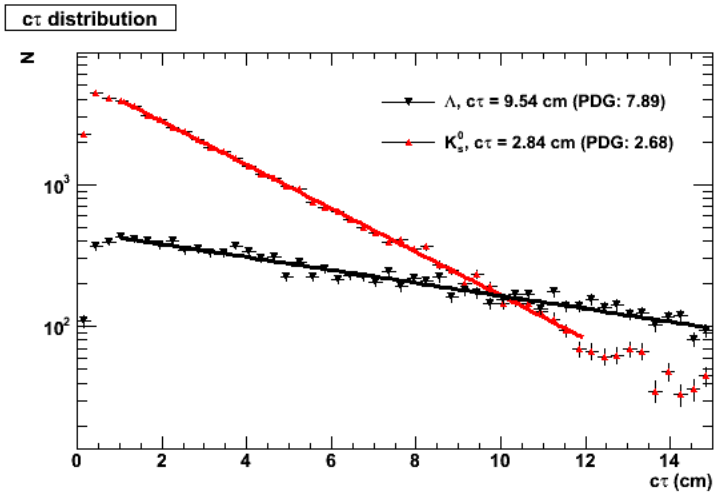

Figure 6.14: K_s^0 (red) and Λ (black) decay time distributions for MC. The values of the lifetimes, derived from a fit with an exponential function are shown in the legend along with the PDG value.

6.4 The analysis method

The purpose of the investigation is to produce the p_T spectra of Λ, $\bar{\Lambda}$, and K_s^0; this analysis focuses on the invariant mass distributions – which contain the energies and momenta of the two daughter particles (see equation 2.11) measured by the TPC.

The input to the analysis is two dimensional histograms of the invariant mass difference versus p_T for the V^0 particle. In Fig. 6.15(c) and 6.15(d), the invariant mass vs. p_T in MC is shown for Λ and K_s^0. The invariant mass distribution for $\bar{\Lambda}$ is similar to the Λ distribution, therefore this V^0 particle is left out when explaining the method.

Extraction of the number of V^0 particles is carried out by analyzing the distributions from the invariant mass histogram for each p_T bin independently. The p_T bins are made narrower at low values and broader at higher values due to less statistics at higher p_T. The mass peak is clearly visible on top of a background. The background is larger in the Λ and $\bar{\Lambda}$ case, than for the K_s^0, described in Sec. 6.3.3.

To subtract the background a fit is done to both the peak and the background with a function of one gauss (for the peak) and a second degree polynomial (for the background). This function is fitted to the invariant mass in a region around the peak. The background can then be removed by subtracting the background fit from the total distribution, see example for Λ in Fig. 6.15(e). To get a hint if this is the right procedure and the right fit, the peak fit is plotted on top of the TRUTH$_{det}$ invariant mass, and Fig. 6.15(f) demonstrate that this is indeed a very precise method.

From the integral of the fit to the peak, the number of V^0 particles is obtained and is used to make one histogram bin in the p_T spectrum, where the number of particles in a certain p_T- and η bin is plotted versus the p_T. But before this can be done, some corrections need to be done, as well as a more quantitative study of how reliable this method is.

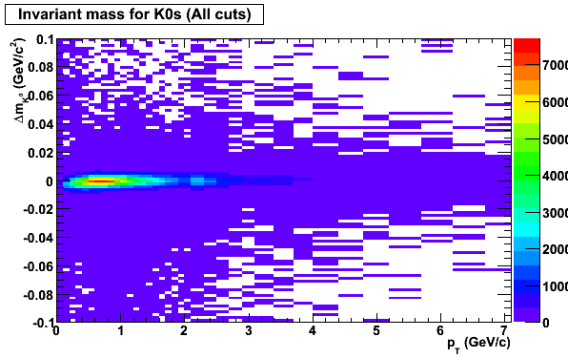

(a) p_T versus $\Delta m_{K^0_s}$, TRUTH$_{det}$.

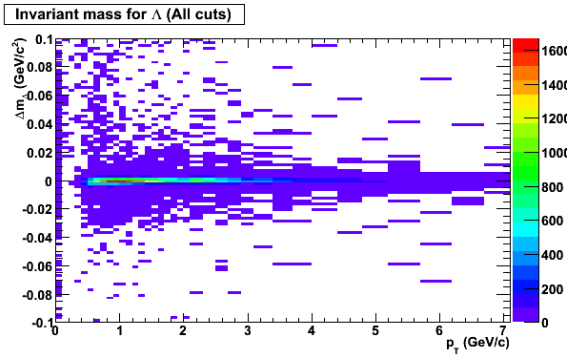

(b) p_T versus Δm_{Λ}, TRUTH$_{det}$.

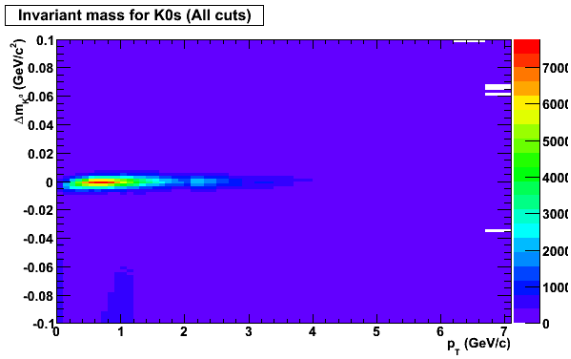

(c) p_T versus $\Delta m_{K^0_s}$, MC.

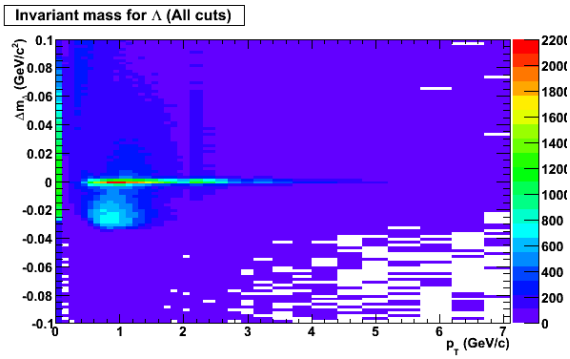

(d) p_T versus Δm_{Λ}, MC.

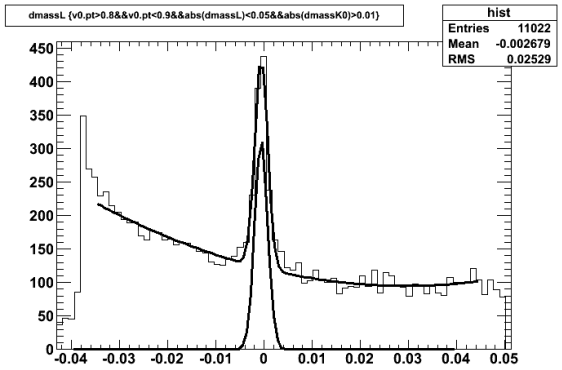

(e) Procedure, step 1: Δm_{Λ} MC distribution with fit.

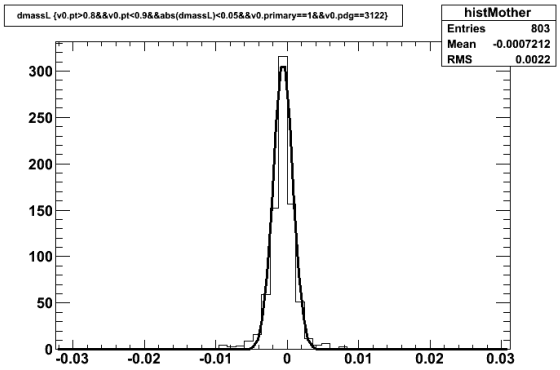

(f) Procedure, step 2: Δm_{Λ} TRUTH$_{det}$ distribution with the MC fit on top.

Figure 6.15: The analysis method: the input to the analysis is the 2D histograms of the invariant mass versus p_T. The number of V^0 particles is obtained by the distributions for each p_T bin independently, where a fit is made to the peak and background. The background is then subtracted and the integral of the fit to the peak is the number of V^0 particles.

6.5 Monte Carlo study

The method is now established and applied to MC data to see if it is a robust method. In this section, the MC data which has been treated the exact way as real data, is compared to TRUTH$_{det}$ data where the true results can be obtained, i.e. where the PID of the V^0's are known. Hence, the method is applied to MC and the number of V^0 particles obtained is compared with the true number of V^0 particles (from TRUTH$_{det}$).

6.5.1 The quality of the fits

The MC signal over TRUTH$_{det}$ signal ratio, i.e. the number of particles calculated from the integral of the MC fit divided by the number of true reconstructed MC particles, is plotted for Λ and K^0_s in Fig. 6.16(a), and for Λ and $\bar{\Lambda}$ in Fig. 6.16(b). This ratio hence indicates how good the fit is to the mass peak; if, in the ideal case, the ratio is 1, then the calculated number of particles are equal to the generated number of particles. As can be seen in the figures, the ratio for K^0_s is approximately 1, except for very high p_T. For the Λ and $\bar{\Lambda}$ the ratio is very similar to each other, and close to 1, with a small increase in MC particles compared to the TRUTH$_{det}$ particles at mid p_T, but still acceptable within statistical errors except for very high p_T.

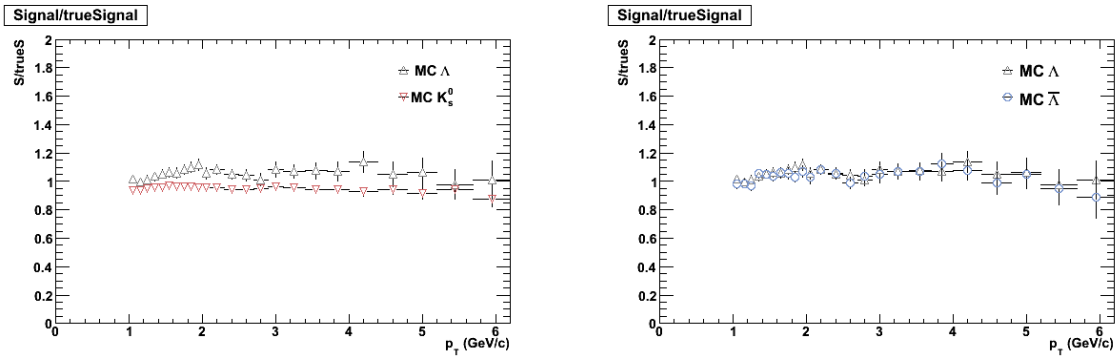

(a) Λ and K^s_S.

(b) Λ and $\bar{\Lambda}$.

Figure 6.16: MC signal over TRUTH$_{det}$ signal indicates how good the fit is to the mass peak.

6.5.2 Efficiency and other corrections

The efficiency of the V^0 particle detection is the number of reconstructed particles (from MC) divided by the number of generated particles (from TRUTH$_{gen}$). The efficiency for no cuts is shown in Fig. 6.17(a) with a value of 50% above $p_T = 2.5$ GeV/c, and for all cuts in Fig. 6.17(b) with a value of 40% above $p_T = 2.5$ GeV/c. As can be seen, the shape before and after the cuts are similar; the cuts hence mostly affect the background – another indication of correctly and efficiently done cutting. Fig. 6.17(d) shows similar behavior as the ones obtained here (note the different center of mass energy).

The decrease in efficiency is clear when these figures are compared[5]. The efficiency rises fast for small p_T, and is more slowly increasing for higher p_T. The fact that the efficiency is limited at low p is due to the larger opening angle of low p_T particle decays, and thus one daughter may be falling outside the η region of the TPC [8]. In Fig. 6.17(c) the inverse efficiency histograms are shown since this is the correction factor for the p_T spectra, and it is seen that for the low p_T region the correction is higher than the higher p_T region, where the efficiency is increasing. The efficiency increases with p_T, but is limited by the particle decay branching ratios which, in the Λ and $\bar{\Lambda}$ case is 63.9% for the $p + \pi^-$ resp. $\bar{p} + \pi^+$ channel, and 68.6% for the $\pi^+ + \pi^-$ channel of K^0_s decays.

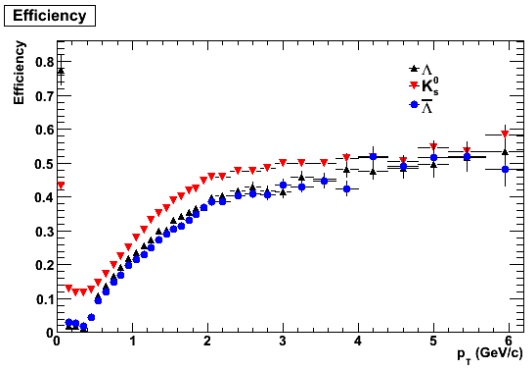

(a) Efficiency, no cut.

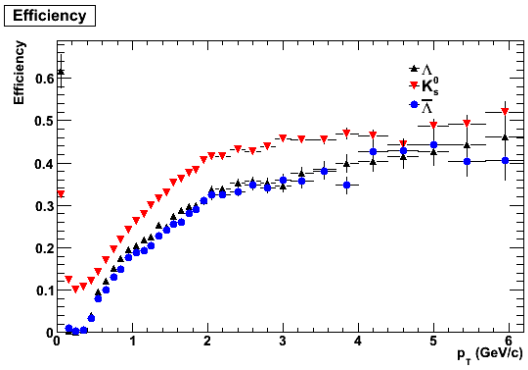

(b) Efficiency, all cuts.

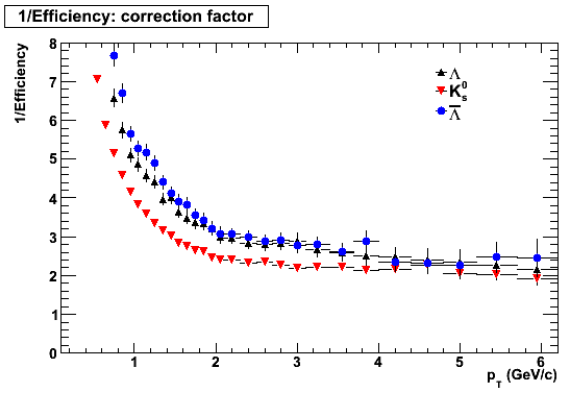

(c) Efficiency correction factor, all cuts.

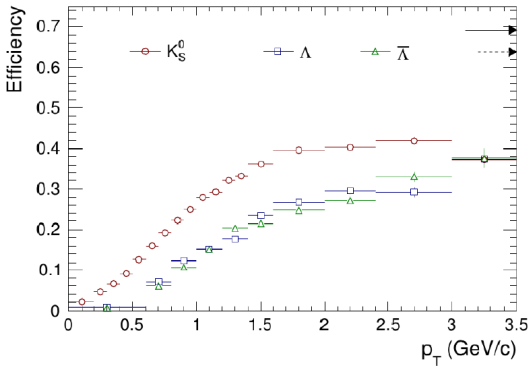

(d) The efficiency from ALICE strange particle production measurements in pp collisions at $\sqrt{s} = 0.9$ TeV [8].

Figure 6.17: Efficiency for different V^0 particles.

From the integral of the fit to the invariant mass distribution the raw number of particles in that specific p_T bin can be obtained. This number is then normalized to the bin width, the pseudo rapidity region, and the number of events, as well as the efficiency correction 1/efficiency.

[5]Note the different scales.

A correction for pseudorapidity, η, to rapidity, y, is also applied since the invariant yield, $d^2N/dydp_T$, is desired for the p_T spectra. Since η is a good approximation of y only at high p_T, see Fig. 6.18 where η for different y ($y = 1$ and $y = 2$), is plotted for MC data as a function of p_T for Λ and K^0_s, – and since the particle's η is what is measured – the transformation from η to y is necessary.

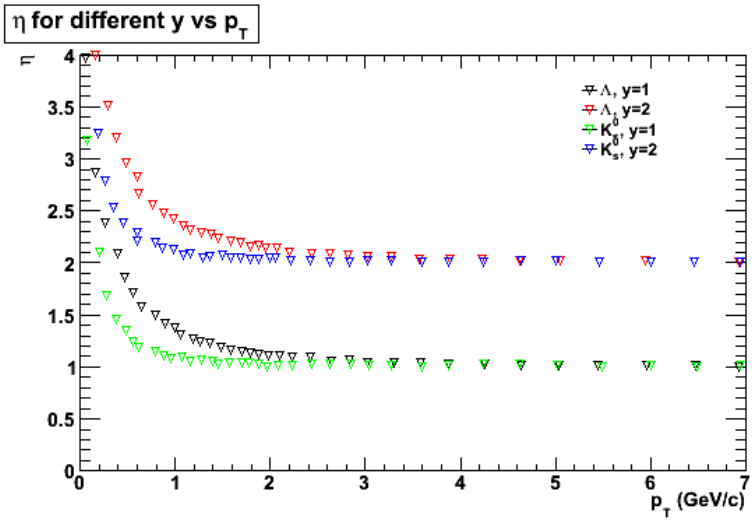

Figure 6.18: Pseudorapidity, η, for different rapidity, y, as a function of transverse momentum, p_T, for Λ and K^0_s. 7 TeV MC data.

This is derived in the following way:

$$p_z = m_T \cdot sinh(y) \text{ and } p_z = p_T \cdot sinh(\eta) \tag{6.18}$$

where

$$m_T = \sqrt{p_T^2 + m^2} \tag{6.19}$$

then

$$\Rightarrow m_T \cdot sinh(y) = p_T \cdot sinh(\eta) \tag{6.20}$$

and

$$\Rightarrow y = sinh^{-1}\left(\frac{p_T}{m_T} \cdot sinh(\eta)\right) \tag{6.21}$$

So for all p_T bin centers, the rapidity is calculated by Eq. 6.21 (with $eta = 0.8$), and the number of particles in that bin is divided by the rapidity to be able to have the yield per rapidity interval instead of pseudorapidity.

In Fig. 6.19, the uncorrected (regarding rapidity only) p_T spectra for MC Λ and K^0_s particles are shown. When comparing these spectra with the rapidity corrected spectra in Fig. 6.20, it is seen that the effect is stronger for Λ's, which is also confirmed by the theory represented in Fig. 6.18, where it is concluded that Λ particles needs to have higher p_T in order for the pseudorapidity to be comparable to the rapidity, compared to K^0_s particles – due the the fact that $m_\Lambda > m_{K^0_s}$.

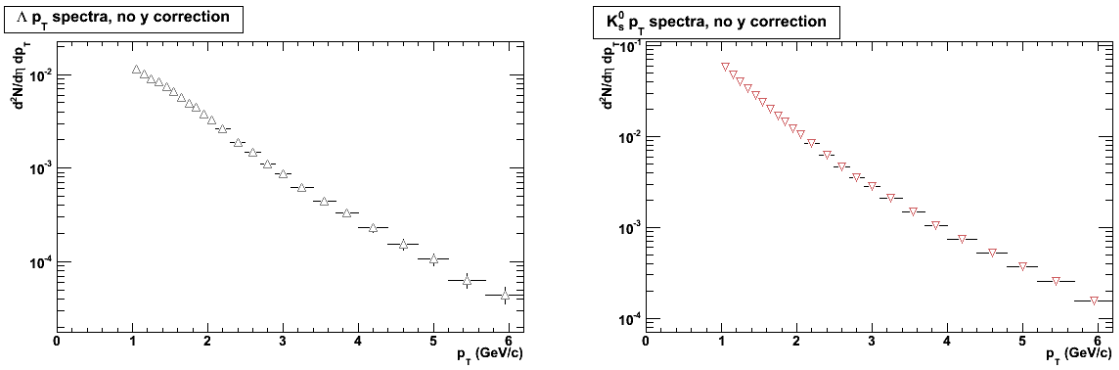

(a) p_T spectra Λ. (b) p_T spectra K^0_S.

Figure 6.19: MC p_T spectra without rapidity correction.

6.5.3 MC p_T spectra

The normalized number of particles is plotted versus p_T. These are the so called p_T spectra which can be seen for MC and TRUTH$_{gen}$ Λ, $\bar{\Lambda}$, and K^0_s particles in Fig. 6.20. The spectra show statistical uncertainties from signal extraction and efficiency correction, as well as feed down correction of Λ's created in the detector material, but not Λ's from e.g. Ξ decays.

These results demonstrate that there is excellent agreement between the TRUTH$_{gen}$ and the MC data treated as real data through the whole analysis procedure. There is hence very strong arguments to trust the method, the cuts and the corrections. The analysis can now be applied to real data with good confidence, and it is important to show that MC is realistic.

6.6 MC versus Data

6.6.1 Invariant mass distribution

The analysis starting point is in the invariant mass distribution, mentioned earlier. To be able to trust the data results, it is important to check if the data and MC coincide there, i.e. if the shape of the data distribution is similar to the MC distribution (which we, by now, know that the method *can* be applied to), to compare later results.

Fig. 6.21 shows the invariant mass distribution versus p_T for MC Λ's and K^0_s's. By eye, these seem similar, even the "cloud" of higher number of particles centered at $\Delta m_\Lambda = -0.02$ for low p_T is reproduced in MC (and is therefor – for all practical purposes – nothing to worry about, especially since the analysis carried out here does not consider $p_T < 1$ GeV/c) and can hence be considered as realistic.

A more quantitative comparison is demonstrated in Fig. 6.22-6.23, which shows the invariant mass distribution for Λ, $\bar{\Lambda}$, and K^0_s for three p_T bins, where $0.5 <$ low $p_T <$ 2.5 GeV/c, $2.5 <$ mid $p_T < 4.5$ GeV/c, and $4.5 <$ high $p_T < 6.5$ GeV/c. The fact that the data and MC have similar shape of the distributions indicates that they have equal properties, which supports the conclusions reached in the previous section, and suggests that background and signal are similar in data and MC.

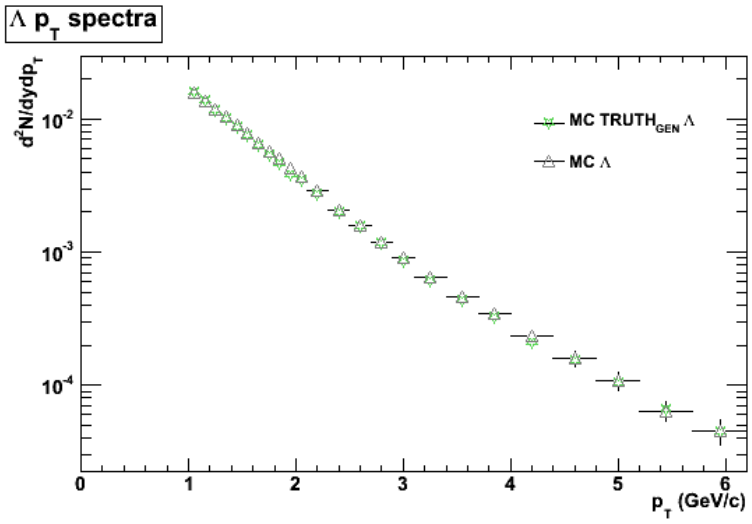

(a) p_T spectra Λ.

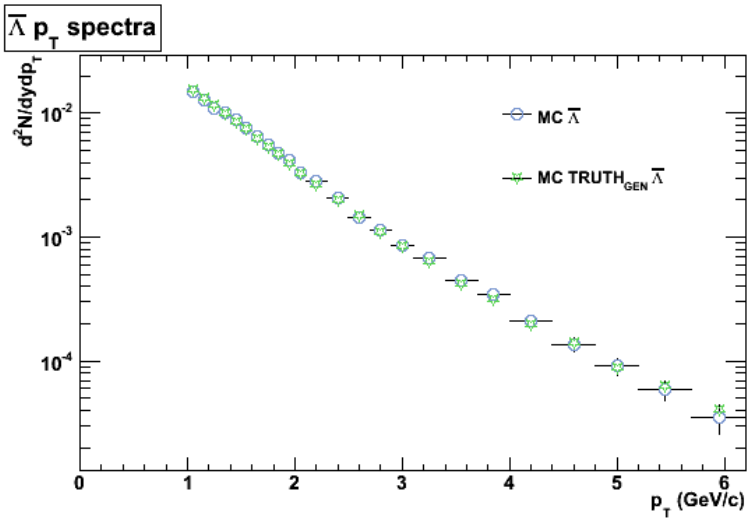

(b) p_T spectra $\bar{\Lambda}$.

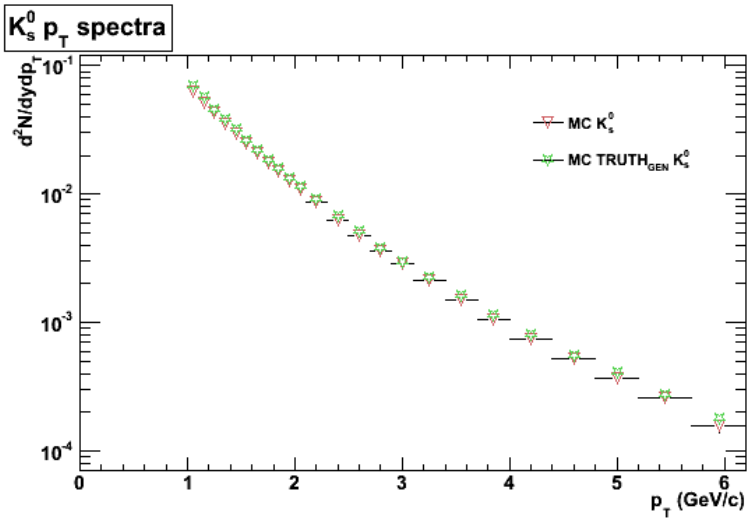

(c) p_T spectra K^0_S.

Figure 6.20: MC p_T spectra.

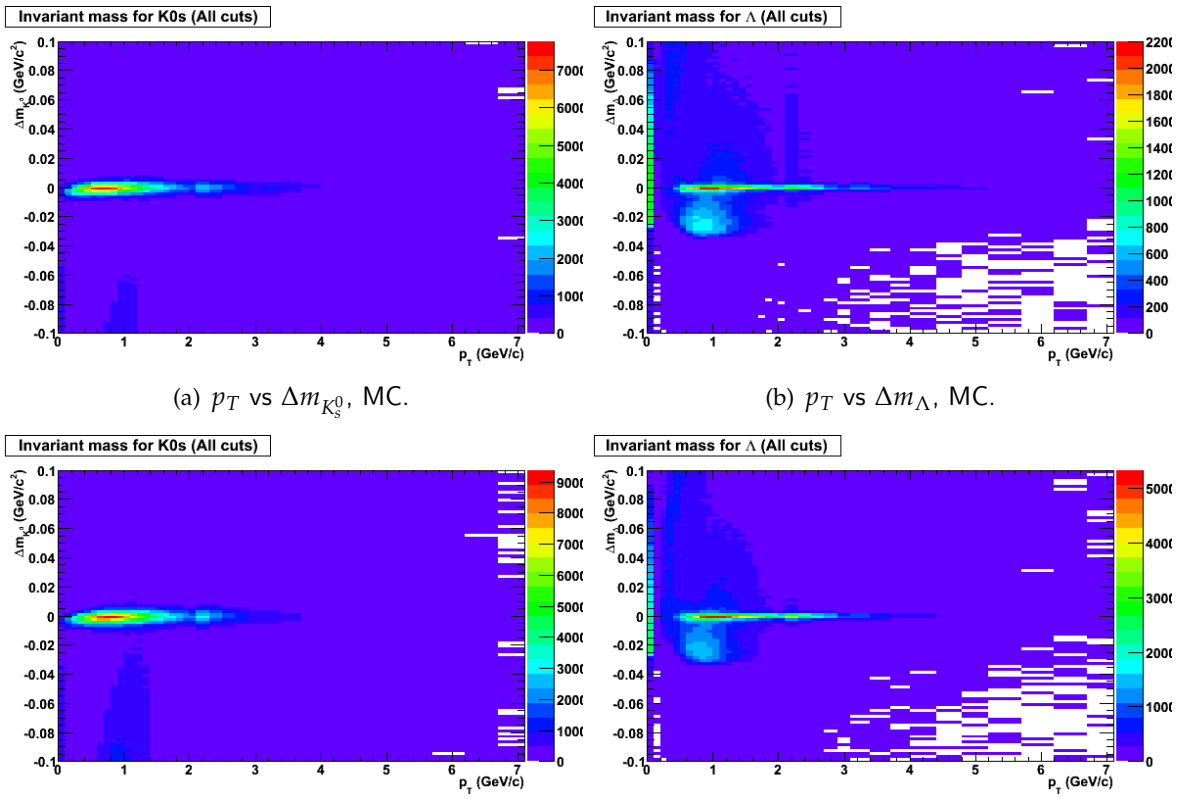

(a) p_T vs $\Delta m_{K_s^0}$, MC.

(b) p_T vs Δm_{Λ}, MC.

(c) p_T vs $\Delta m_{K_s^0}$, data.

(d) p_T vs Δm_{Λ}, data.

Figure 6.21: Input to the analysis.

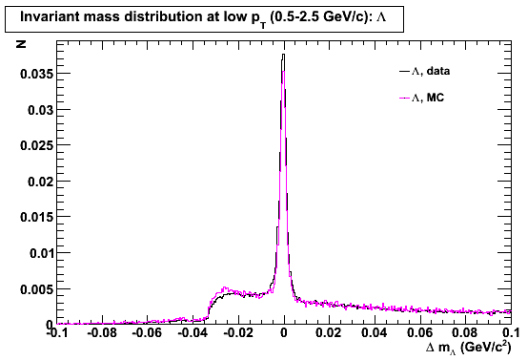

(a) Δm_{Λ} low p_T.

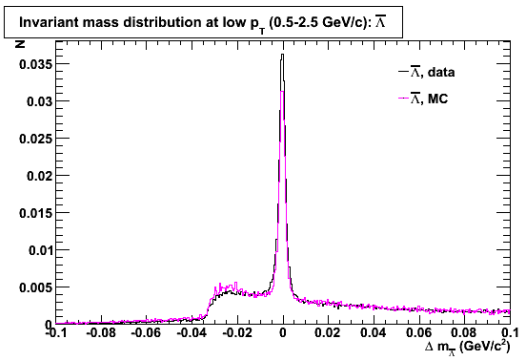

(b) $\Delta m_{\bar{\Lambda}}$ low p_T.

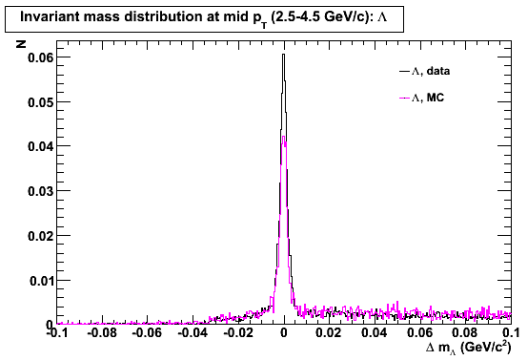

(c) Δm_{Λ} mid p_T.

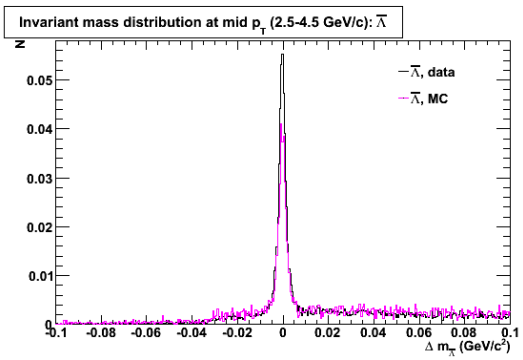

(d) $\Delta m_{\bar{\Lambda}}$ mid p_T.

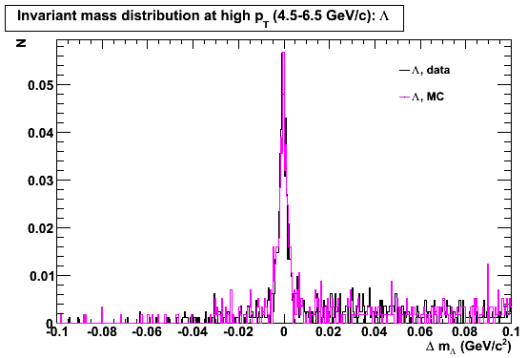

(e) Δm_{Λ} high p_T.

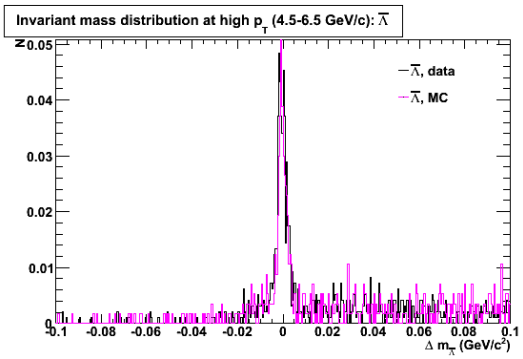

(f) $\Delta m_{\bar{\Lambda}}$ high p_T.

Figure 6.22: The invariant mass distribution in three different p_T bins: $0.5 <$ low $p_T <$ 2.5 GeV/c, $2.5 <$ mid $p_T < 4.5$ GeV/c, and $4.5 <$ high $p_T < 6.5$ GeV/c. The shape is the same for MC and data indicating that they have equal properties.

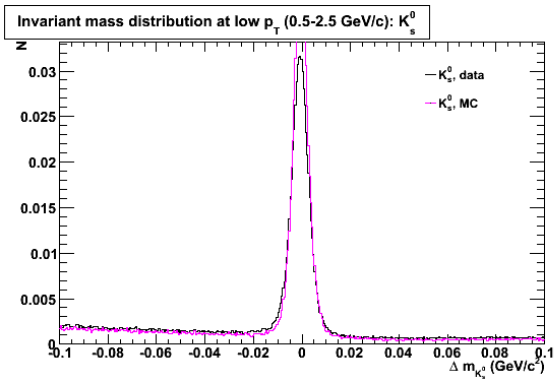

(a) $\Delta m_{K_s^0}$ low p_T.

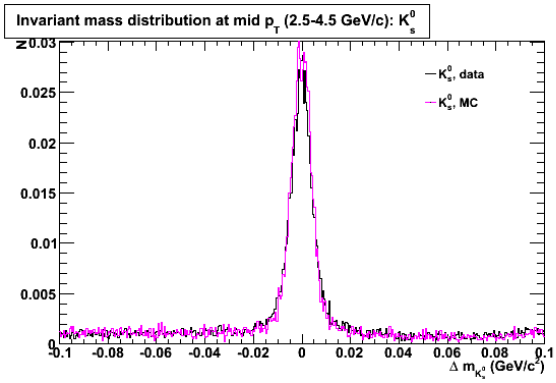

(b) $\Delta m_{K_s^0}$ mid p_T.

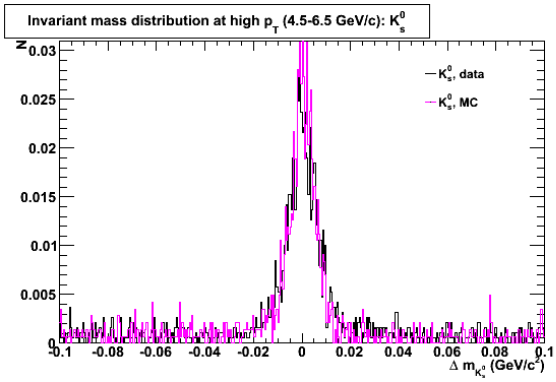

(c) $\Delta m_{K_s^0}$ high p_T.

Figure 6.23: The invariant mass distribution in three different p_T bins: $0.5 <$ low $p_T <$ 2.5 GeV/c, $2.5 <$ mid $p_T < 4.5$ GeV/c, and $4.5 <$ high $p_T < 6.5$ GeV/c. The shape is the same for MC and data indicating that they have equal properties.

The actual analysis is then carried out in narrower p_T bins. The invariant mass plots are shown in Appendix 1.

As mentioned earlier, it is the integral of the Gaussian fit to the peak that is used to obtain the raw number of particles. In the next section a detailed analysis of the fits is made. The invariant mass distribution and the fits are done for Λ, $\bar{\Lambda}$, and K^0_s.

6.6.2 Fit results

To get a quantitative analysis of the signal fits, different variables of the fit are plotted versus p_T, see Fig. 6.24-6.28. The figures below are again demonstrating that the method can be applied to data, since data and MC are comparable – and the robustness of the method for MC has been proved in the previous sections.

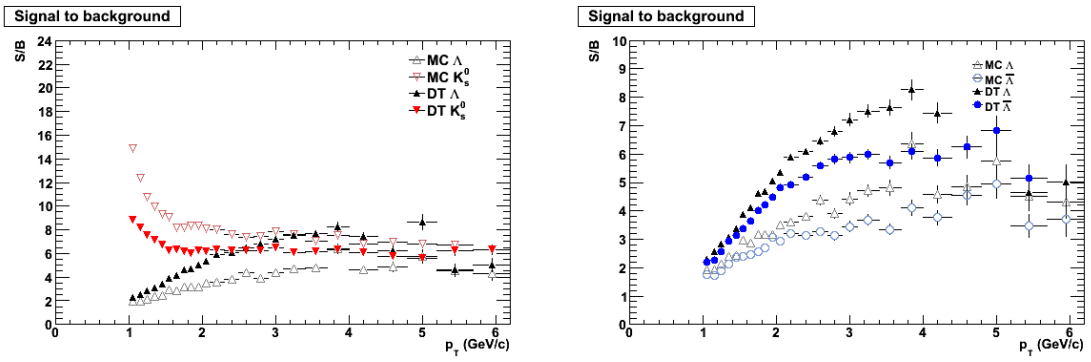

(a) Λ and K^0_s.

(b) Λ and $\bar{\Lambda}$.

Figure 6.24: Signal to background ratio: a measure of how large the signal is compared to the background. For K^0_s the signal is large compared to the background for p_T less than 1 GeV/c, and above 1 GeV/c the background becomes visible but still low. The Λ and $\bar{\Lambda}$ signal over background ratio starts out with a large background, but the signal enhances at higher p_T.

Fig. 6.24(a) and 6.24(b) shows the ratio signal over background, which is a measure of how large the signal is compared to the background, where the background region is defined as 3σ, i.e. three times the width of the peak.

The figures 6.25(a), 6.25(b), 6.26(a), and 6.26(b) show the mean and the width of the fitted Gaussian function, which all increases at higher p_T. Since the mean is lower than 0 at low p_T, the data is systematically off by this value. However, note that the offset is less than 1 MeV/c^2, verifying the magnetic field calibration and the alignment. Clearly these effects are correctly modeled in MC since the shift are seen also there.

The width is related to the momentum resolution. The slightly increasing width with p_T of the V^0 particle is due to the worse momentum resolution of large p_T, see Fig. 4.4.

The last figures in the fits result study, Fig. 6.27(a), 6.28(a), 6.27(b), and 6.28(b), show the quantity signal divided by signal + background in a region defined by 3σ of the peak, and tells us about the "purity" of the different particles where 1 is 100% pure (i.e. the background is negligibly small). In 6.27(a) and 6.28(a) there are no cuts on mass, pointing angle, or DCA_s,

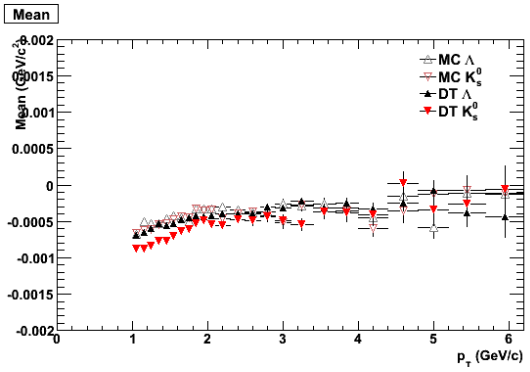

(a) Mean value for Λ and K^0_s.

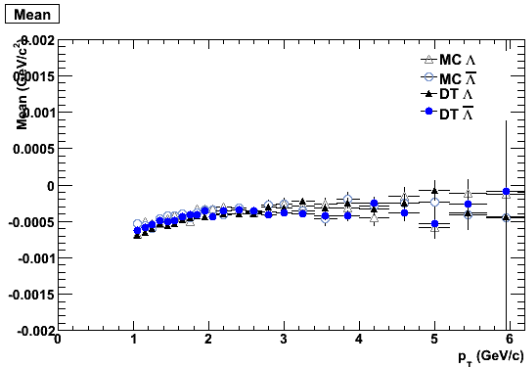

(b) Mean value for Λ and $\bar{\Lambda}$.

Figure 6.25: Mean value of signal fit.

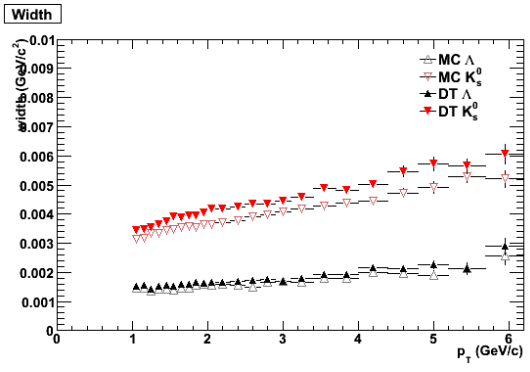

(a) Width for Λ and K^0_s.

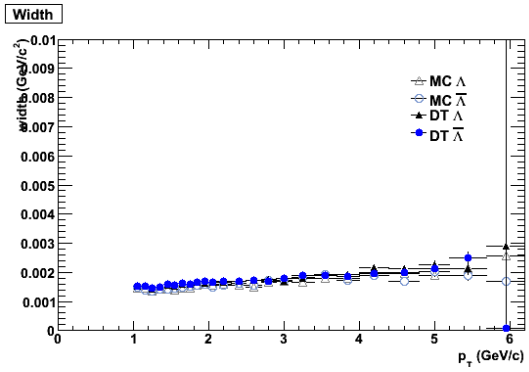

(b) Width for Λ and $\bar{\Lambda}$.

Figure 6.26: Width (σ of the Gaussian) of signal fit.

while for the other figure all the cuts are implemented. All particles increase their purity after the cuts, but especially K_s^0 since the purity goes from 65% for data with no cuts at mid and high p_T to 80% for data with cuts at mid and high p_T. Λ and $\bar{\Lambda}$ increase the purity with a few percent and land at 80% for data after the cuts at mid and high p_T.

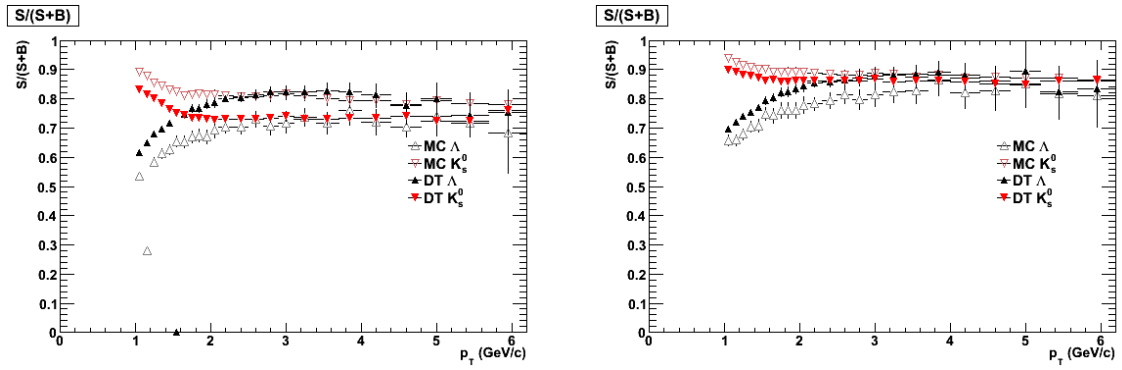

(a) No cuts. (b) All cuts.

Figure 6.27: Purity for Λ and K_s^0.

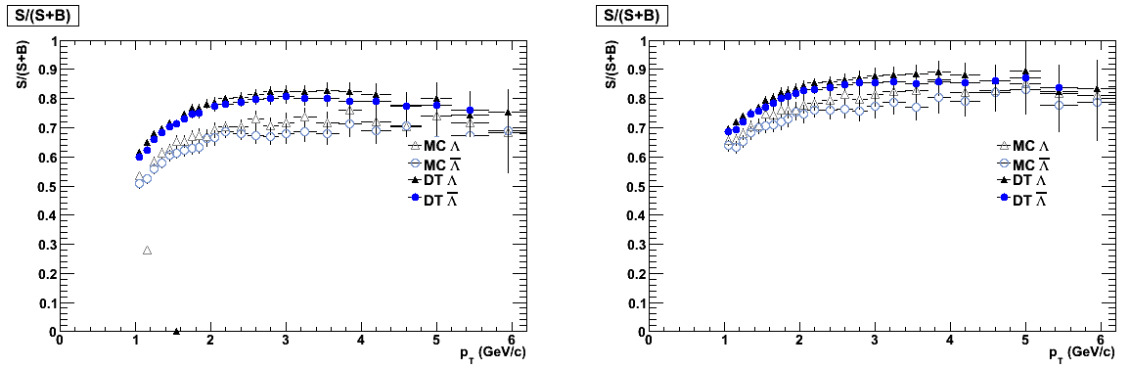

(a) No cuts. (b) All cuts.

Figure 6.28: Purity for Λ and $\bar{\Lambda}$.

Chapter 7

Results and conclusions: p_T spectra and Λ/K^0_S, $\bar{\Lambda}/\Lambda$ invariant yield ratios

As in the case for the MC study, the data analysis method is done in the same way; the background in the invariant mass distribution was significantly reduced by three well motivated cuts: the mass overlap cut, the pointing angle cut, and the cut in distance of closest approach. With these cuts the purity of the samples was increased, and by that a more detailed and accurate analysis could be performed.

From the integral of the invariant mass peak the number of particles in a p_T bin is obtained. All correction factors and normalizations described for the MC analysis are done also in the data analysis. Then the p_T spectra of the three V^0 particles are constructed, represented in Fig. 7.1 where the invariant yield, $d^2N/dydp_T$, is plotted as a function of p_T. In these spectra the data results are presented, but also MC, TRUTH$_{gen}$, and ALICE results which comes from an independent analysis are shown. As for the MC spectra, these spectra show statistical uncertainties from the signal extraction and the efficiency correction, and are not feed down corrected, see Sec. 6.5.3. The TRUTH$_{gen}$ has no uncertainty since it is the true number of particles.

There is a rapid decrease of the yield with increasing p_T. The error bars are relatively small, except for very large p_T. It is also seen that the shape of the MC and data is similar, but that the MC spectra are underestimated by a factor ~ 2 for K^0_s and a factor ~ 3 for Λ and $\bar{\Lambda}$. This is also seen in published results from an ALICE analysis of pp collisions at $\sqrt{s} = 0.9$ GeV (which can be found in reference [8]), and from a CMS analysis of pp collisions at $\sqrt{s} = 0.9$ GeV and $\sqrt{s} = 7$ GeV (found in reference [9]). The large underestimations of the MC yield is not only for the PYTHIA tune used in this analysis, but for several other tunes and MC PHOJET as well. Fig. 7.2(c) shows the MC spectra divided by spectra from data from the CMS analysis: the two upper plots is the interesting ones in this context, where it is seen that MC K^0_s and Λ are heavily underestimated. Fig. 7.2(a) and 7.2(b) shows the ALICE results when comparing different MC tunes, also demonstrating this difference. Nevertheless, as mentioned earlier, the shape of the data and MC spectra are similar, implying that PYTHIA reproduces the general features quite well, but differs in the details.

Fig. 7.3 shows the data analysis results from this study compared to other studies by ALICE and CMS. The CMS results from 7 TeV collisions (seen in Fig. 7.3(a) and 7.3(c)) coincide very well with the results carried out in here. The small discrepancy seen for the Λ's is probably a feed down correction effect. Also, the other ALICE analysis of 7 TeV data agrees remarkably well with this analysis, seen in the Λ and K^0_s spectra.

The ALICE results from 0.9 TeV collisions are below (seen in Fig. 7.3(a), 7.3(b), and 7.3(c)) the values obtained with the analysis in this thesis. This is due to the collision energy difference. It is, however, important to compare the results with ALICE 0.9 TeV since – when calculating the pp p_T spectra for PbPb reference purposes – an interpolation between 0.9 TeV and 7 TeV collisions will be done due to the fact that the PbPb data is taken at $\sqrt{s} = 2.76$ TeV.

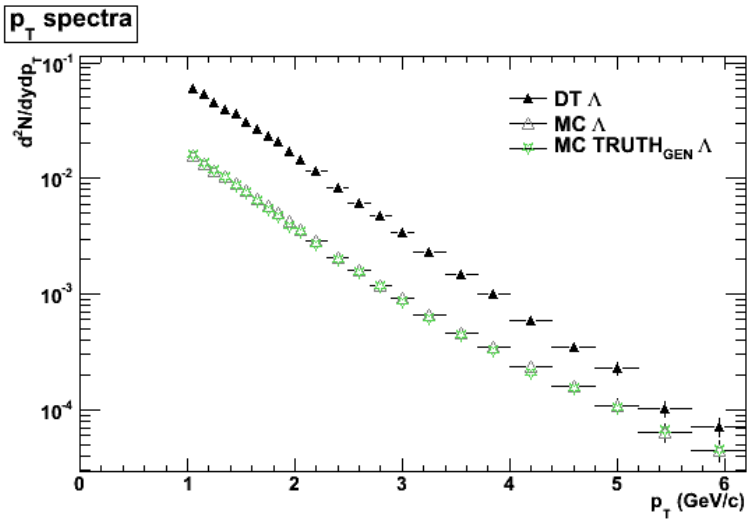

(a) p_T spectra Λ.

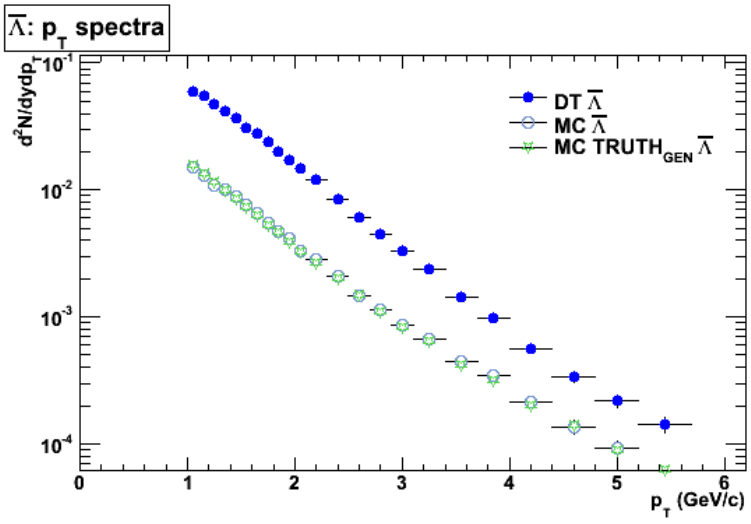

(b) p_T spectra $\bar{\Lambda}$.

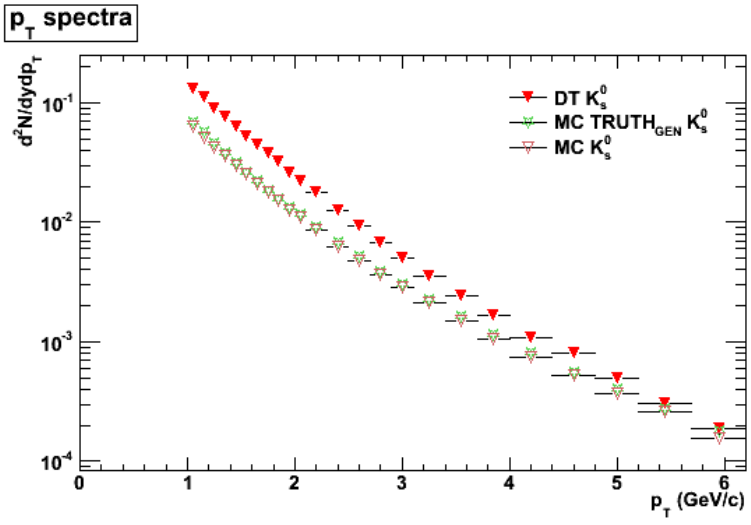

(c) p_T spectra K^0_S.

Figure 7.1: p_T spectra constructed from data compared to MC.

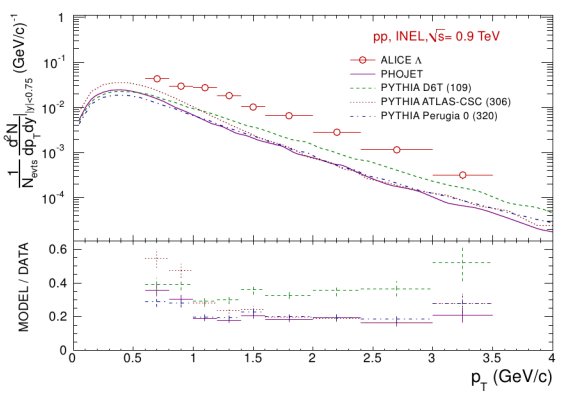

(a) Comparison of the yields for Λ in pp collisions with PHOJET and PYTHIA tunes 109, 306 and 320. Figure from [8].

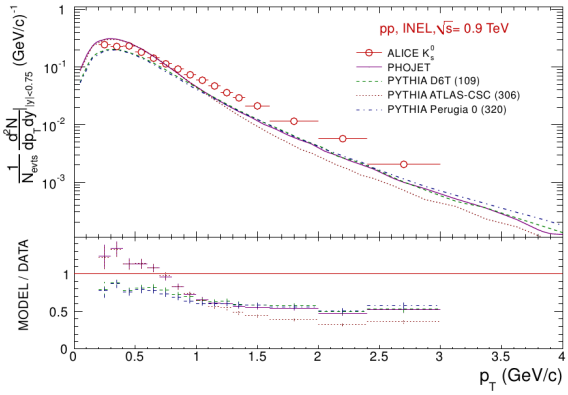

(b) Comparison of the yields for K_s^0 in pp collisions with PHOJET and PYTHIA tunes 109, 306 and 320. Figure from [8].

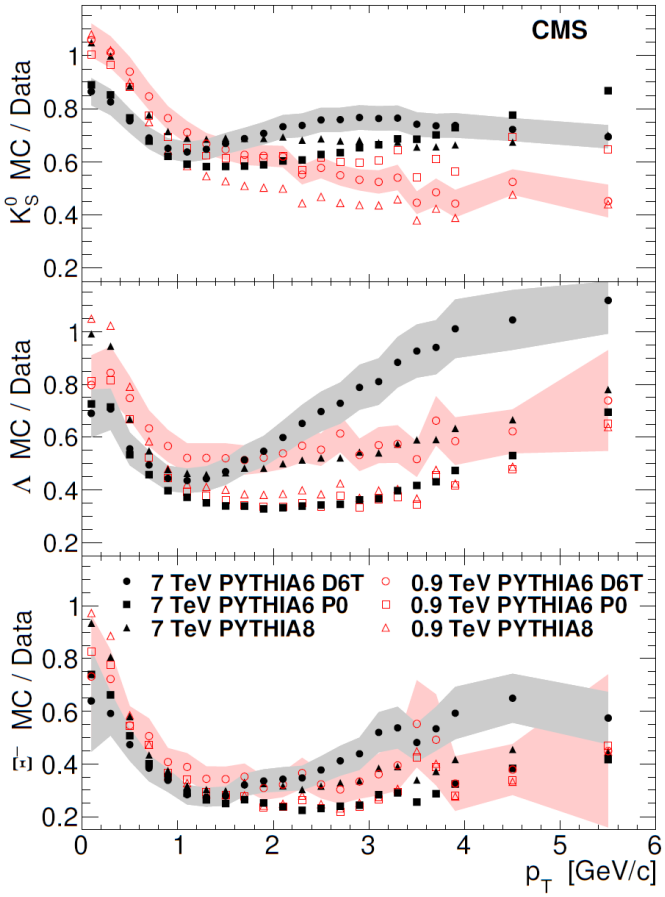

(c) CMS analysis of pp collisions at $\sqrt{s} = 0.9$ GeV and $\sqrt{s} = 7$ GeV showing the MC spectra divided by spectra from data for K_s^0 (upper), Λ (middle), and Ξ (lower, which is not interesting for my analysis). Figure from [9].

Figure 7.2: The yield difference in MC and data.

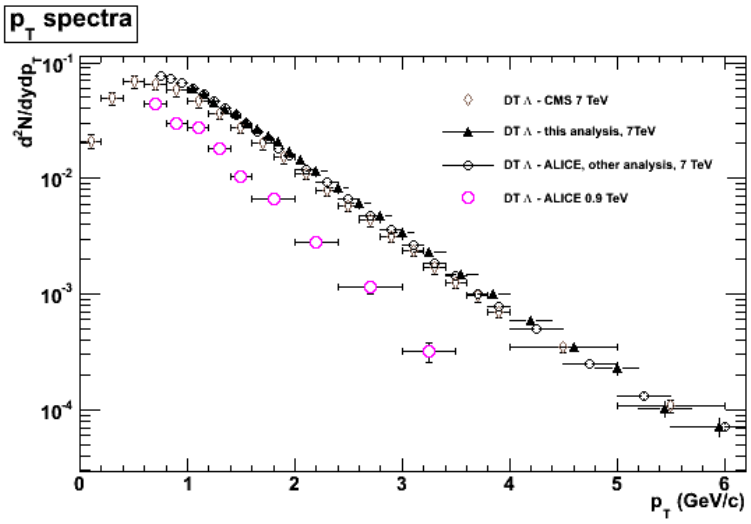

(a) p_T spectra Λ, data.

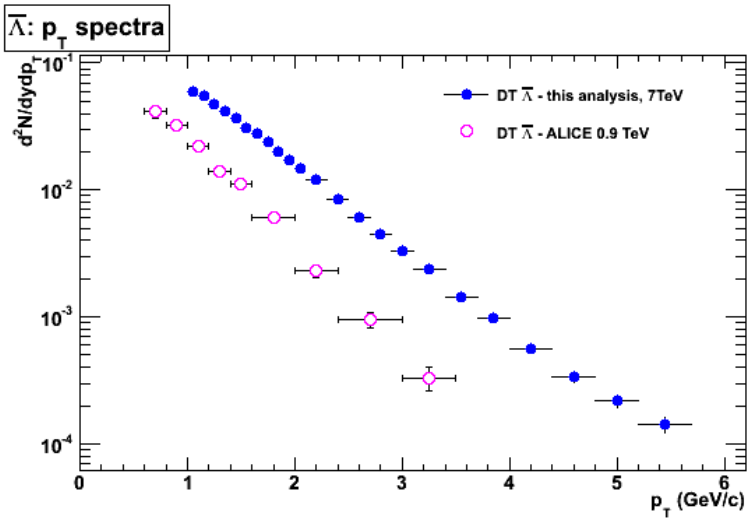

(b) p_T spectra $\bar{\Lambda}$, data.

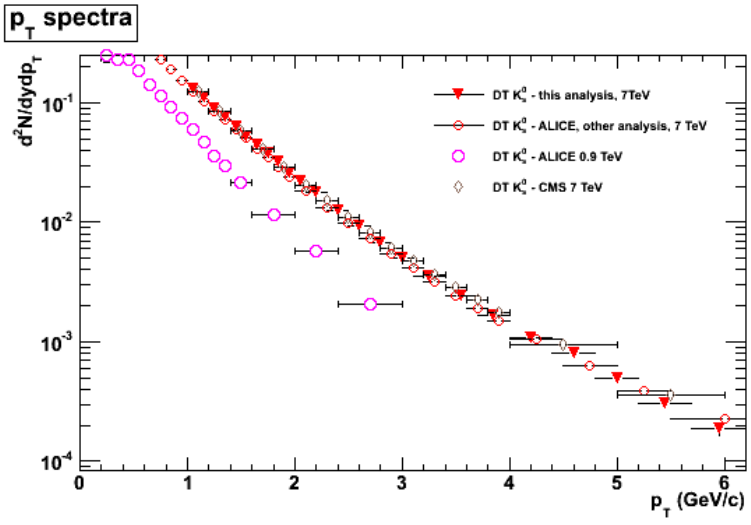

(c) p_T spectra K^0_S, data.

Figure 7.3: p_T spectra constructed from data compared to other analyses by ALICE and CMS.

If the ratio between the spectra is calculated, i.e. the invariant yield ratios, the $\Lambda/\bar{\Lambda}$ ratio and the Λ/K_s^0 ratio can be obtained as a function of p_T. This is done and shown in Fig. 7.4 and 7.5

The $\bar{\Lambda}/\Lambda$, i.e. the antibaryon/baryon ratio, is a measure of the matter-antimatter asymmetry. The strange antibaryon/baryon ratio in pp collisions is expected to be around 1. This is shown in Fig. 7.4 from this analysis for data, MC, and TRUTH$_{gen}$. Also seen in the figure is the STAR measurements of the same quantity, but with a center of mass energy of 200 GeV, with results slightly below 1, i.e. more baryons than antibaryons.

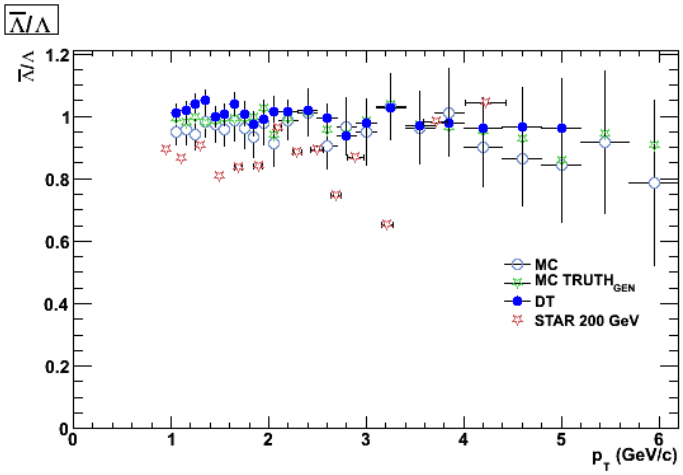

Figure 7.4: $\bar{\Lambda}/\Lambda$ ratio.

The Λ/K_s^0, i.e. the baryon/meson ratio for particles with a strange quark, in pp collisions (or peripheral PbPb collisions) is not expected to change much with p_T, and it is also expected to stay well below 1 since the production of Λ should not be enhanced compared to the production of K_s^0, which is consistent with the ratio obtained in this analysis, see Fig. 7.5 where the data, MC, and TRUTH$_{gen}$ results are presented. The Λ/K_s^0 results are compared with the CMS results at the same center of mass collision energy, whose values are slightly below the one presented in this thesis.

The goal of the study was to perform the Λ, $\bar{\Lambda}$, and K_s^0 spectra, and the ratios Λ/K_s^0 and $\bar{\Lambda}/\Lambda$, shown in this section. Results presented in an analysis like this is absolutely necessary to have before PbPb data can be analyzed in order to draw any conclusions about final state effect, i.e. how the produced medium in the collision modify the production of particles. With the starting point in analysis about the spectra, baryon/meson, and antiparticle/particle production in pp collisions – such as this one – we can, with good confidence, begin to analyze central PbPb events and use analysis like this as a reference, where we know that no QGP is created, to understand heavy ion collisions in terms of strangeness enhancement, particle spectra and ratios. The measurements presented here can also be used to tune PYTHIA and other models. Also, this analysis is an important ingredient when it comes to cross checks in the charged particle identification analysis based on dE/dx measurements since – by selecting Λ, $\bar{\Lambda}$, and K_s^0 particles – a clean sample of pions and protons can be obtained.

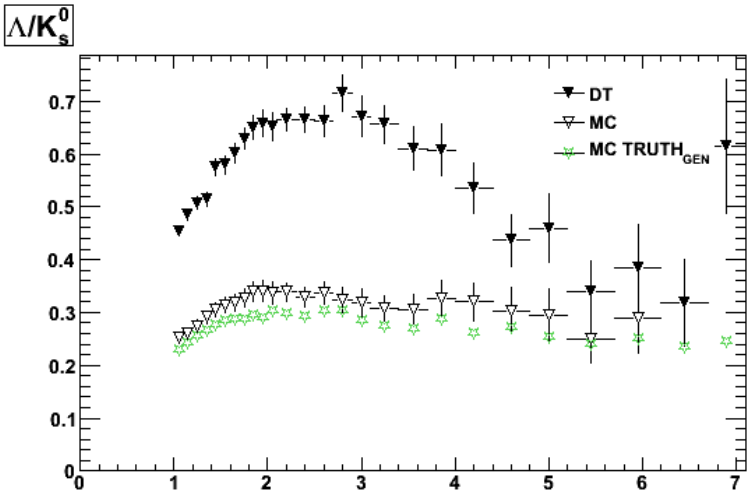

(a) Λ/K^0_S.

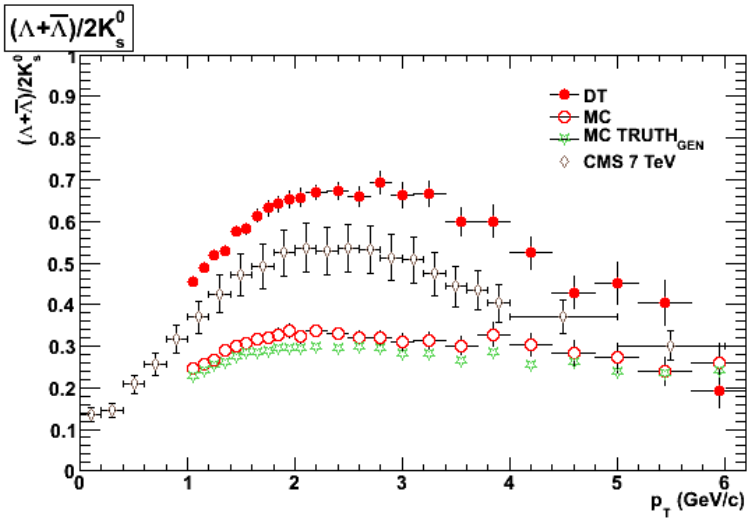

(b) $(\Lambda + \bar{\Lambda})/2K^0_S$

Figure 7.5: Particle ratios.

Chapter 8

References

1. J. Alme et al., *The ALICE TPC, a large 3-dimensional tracking device with fast readout for ultra-high multiplicity events*, (January 2010)

2. W. Blum, W. Riegler, L. Rolandi, *Particle Detection with Drift Chambers*, (2008)

3. ALICE Collaboration, *ALICE Technical Design Report of the Time Projection Chamber*, (7 January 2000)

4. Alexandru Florin Dobrin, Doctor's dissertation: *R-hadron Searches and Charged Pion Spectra at High Transverse Momentum in Proton-Proton Collisions at the LHC using the ALICE Detector*, (October 2010)

5. ALICE Collaboration, *Strange particle production in proton-proton collisions at* $\sqrt{s} = 0.9$ *TeV with ALICE at the LHC*, (December 2010), arXiv:1012.3257v2

6. Donghee Kang on behalf of the COMPASS collaboration, *Transverse lambda and anti-lambda polarization with a transveresly polarized proton target at COMPASS*, (), arXiv:

7. ALICE Collaboration, *Production of pions, kaons and protons in pp collisions at* $\sqrt{s} = 900$ *GeV with ALICE at the LHC*, (Jan 2011), arXiv:1101.4110

8. ALICE Collaboration, *Strange particle production in proton-proton collisions at* $\sqrt{s} = 0.9$ *TeV with ALICE at the LHC*, (Dec 2010), arXiv:1012.3257v2

9. CMS Collaboration, *Strange particle production in pp collisions at* $\sqrt{s} = 0.9$ *and 7 TeV*, (May 2011)

10. NA49 Collaboration, *Energy dependence of particle ratio fluctuations in central Pb+Pb collisions from* $\sqrt{s_{NN}} = 6.3$ *to 17.3 GeV*, (Jun 2009), arXiv:0808.1237v3

11. M. Ivanov, A. Kalweit, Y. Pachmayer, *ALICE Internal Note: ALICE-INT-2011-XXX Definitions of TPC related track properties*, (Feb 2011)

12. P. Gros, Doctors's dissertation: *Identifying charged hadrons on the relativistic rise using the ALICE TPC at LHC*, (June 2011)

13. L. Bryngemark, Master's dissertation: *Charged pion spectra at high pT in pp collisions at* $\sqrt{s} = 900$ *GeV, measured by the ALICE TPC*, (June 2011)

14. Iouri Belikov for the ALICE Collaboration, K^0_s *and* Λ *production in Pb–Pb collisions with the ALICE experiment*, Quark Matter Conference 2011, Annecy, proceedings, (June 2011)

15. Stephen Andrew Bull, *Strange Particle and Antiparticle Production in Proton-Beryllium Interactions at 40 GeV/c at the CERN NA57 Experiment*, Thesis submitted for the degree of Doctor of Philosophy, University of Birmingham, (May 2005)

16. B.R Martin and G. Shaw, *Particle Physics. third edition*, ISBN 978-0-470-03293-0, (2008)

17. M.A.C.Lamont et al, Eur. Phys. J C49, 39–55, (2007)

18. C. Lippmann, *Performance of the ALICE Time Projection Chamber*, approved presentation at TIPP conference, (2011), https://indico.cern.ch/contributionDisplay.py?contribId=290&sessionId=16&confId=102998

19. http://www.gauss-centre.eu/quarks/ (29 March, 2011)

20. http://en.wikipedia.org/wiki/Quark (4 August, 2011)

21. http://en.wikipedia.org/wiki/Fermion (4 August, 2011)

22. Private conversation with the ALICE Lund group

Chapter 9

Appendices

9.1 Appendix 1 - Invariant mass distributions

In Fig. 9.1 for Λ, Fig. 9.2 for $\bar{\Lambda}$, and 9.3 for K^0_s, the distribution is shown for smaller bins - first in step of 0.1 GeV/c and then a two-step increase towards higher p_T due to statistics. The fitted function to the distribution is also shown. For K^0_s, the fit is done in a region of 0.150 GeV/c^2 around $\Delta m_{K^0_s} = 0$ (from -0.075 GeV/c^2 to 0.075 GeV/c^2 from $\Delta m_{K^0_s} = 0$).

For the lower p_T bins, bins where $p_T < 1$ GeV/c, Λ and $\bar{\Lambda}$ invariant mass distribution is fitted in a region of 0.07 GeV/c^2 around $\Delta m_{K^0_s} = 0$ (from -0.015 GeV/c^2 to 0.055 GeV/c^2 from $\Delta m_{\Lambda} = 0$), since the background has a sharp edge around $\Delta m_{\Lambda} = -0.02$ GeV/c^2 which should be avoided. This sharp edge is not as distinct for $p_T < 1$ GeV/c, therefore the invariant mass distribution is fitted in a region of 85 MeV/c^2 around $\Delta m_{K^0_s} = 0$ (from -0.03 GeV/c^2 to 0.055 GeV/c^2 from $\Delta m_{\Lambda} = 0$). These arguments are done referring to Fig. 9.1 and 9.3, where the fit region can be seen graphically.

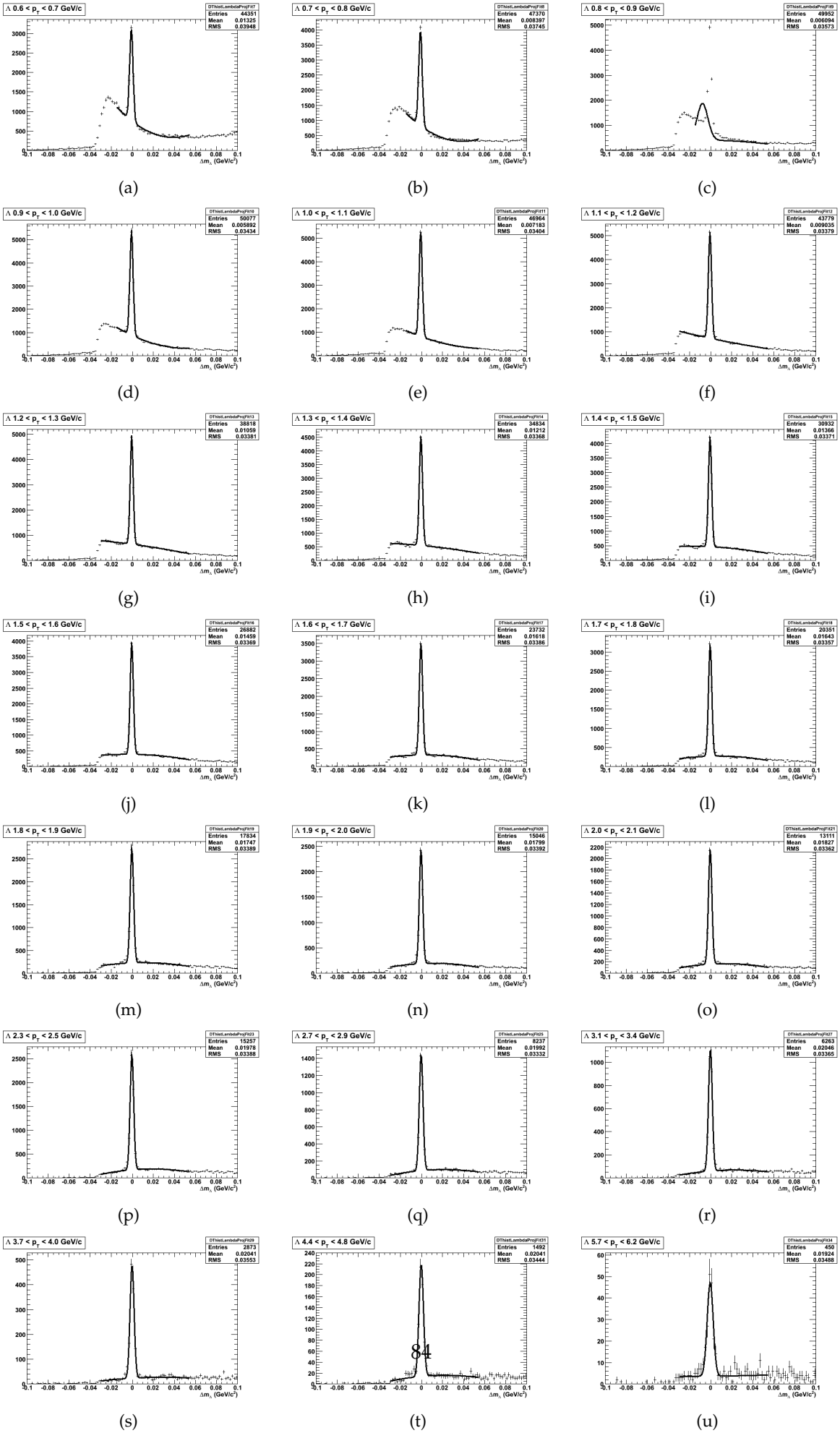

Figure 9.1: Λ: all cuts.

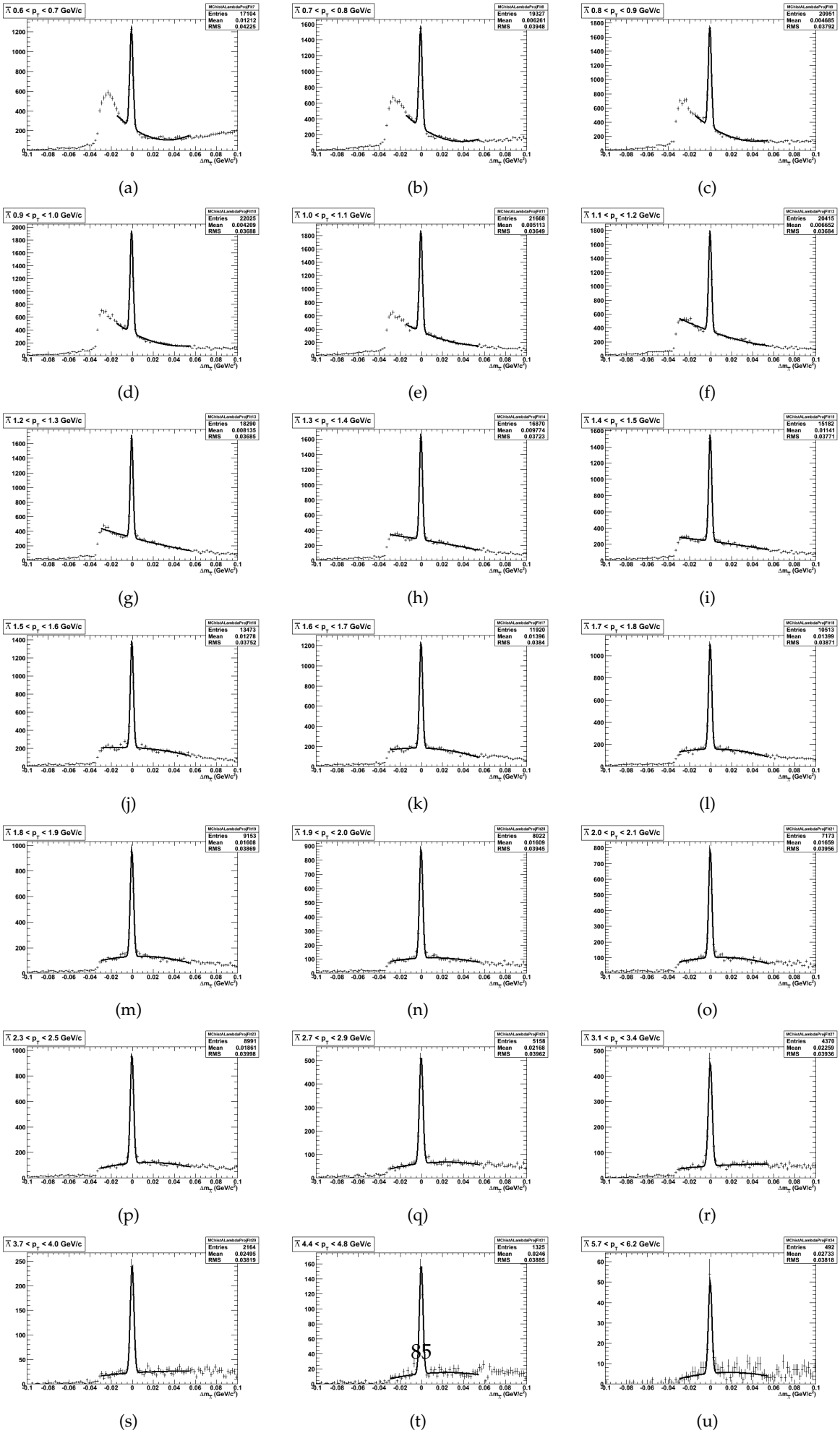

Figure 9.2: $\bar{\Lambda}$: all cuts.

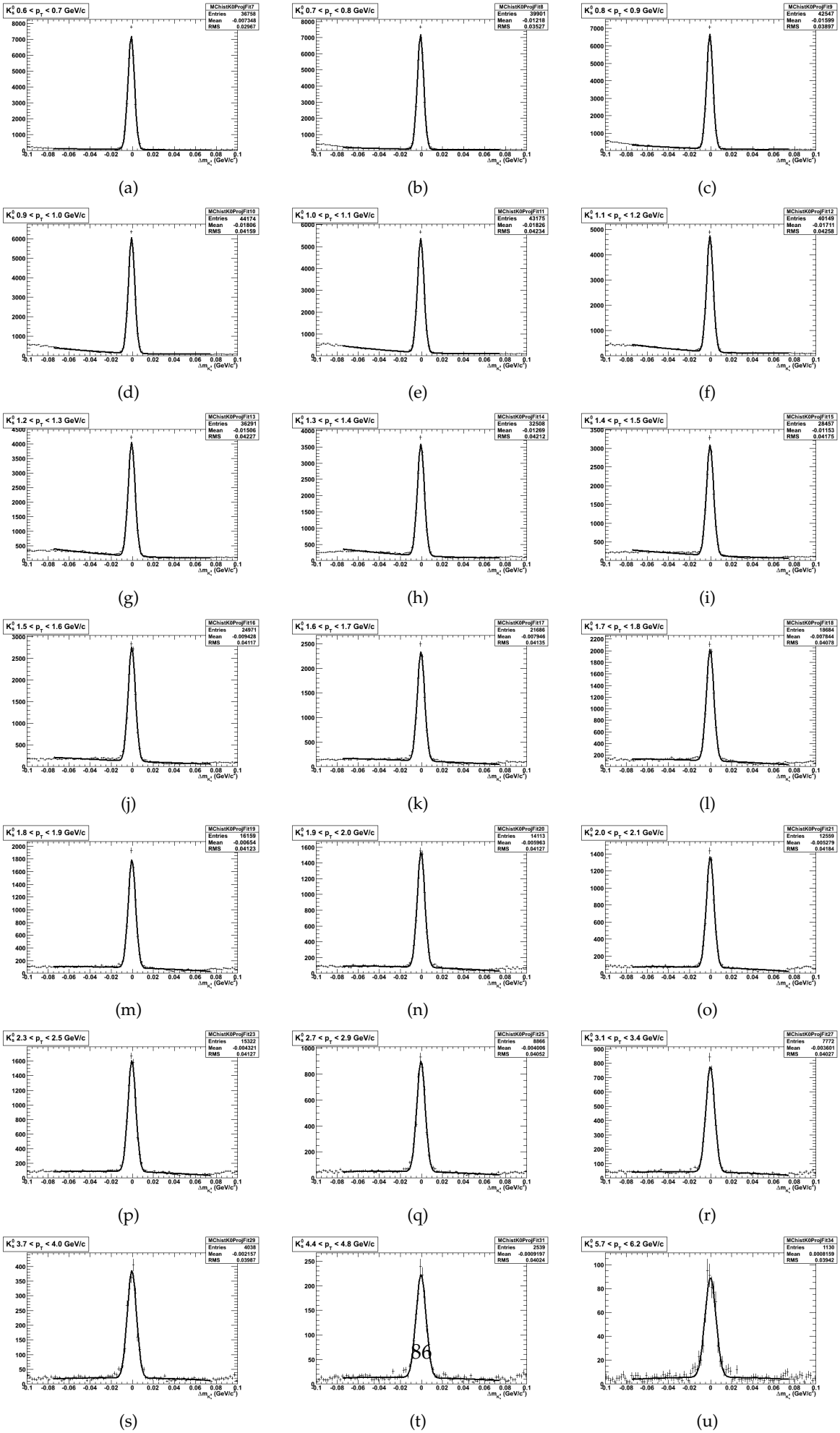

Figure 9.3: K0: all cuts.

9.2 Appendix 2 - Acronyms

AA: nucleus-nucleus collision
ADC: Analog to Digital Converter
ALICE: A Large Ion Collider Experiment
ALTRO: ALice Tpc Read Out
AOD: Analysis Object Data
AP: Armenteros-Podolanski plot
ATLAS: A Toroidal LHC ApparatuS
AuAu: gold-gold collisions
BB: Bethe-Bloch
BR: Branching Ratio
CERN: The European Organization for Nuclear Research
CM: Center of Mass frame
CMS: Compact
CTP: Central Trigger Processor
DAQ: Data AQuisition
DCA: Distance of Closest Approach
DT: Data
DQM: Data Quality Monitoring
EMCal: ElecroMagnetic Calorimeter
ESD: Event Summary Data
FEC: Front End Card
FEE: Front End Electronics
FMD: Forward Multiplicity Detector
GeV: Giga electron Volt
HMPID: High Momentum Particle Identification Detector
HV: High Voltage
IROC: Inner Read Out Chamber
ITS: Inner Tracking System
LHC: Large Hadron Collider
MeV: Mega electron Volt
MC: Monte Carlo
MIP: Minimum Ionizing Particle
MRPC: Multi-gap Resistive Plate Chambers
MWPC: Multi Wire Proportional Chamber
ncl: number of clusters
NN: nucleon-nucleon collision
OROC: Outer Read Out Chamber
pp: proton-proton collision
PASA: PreAmplifier ShAper
PbPb: lead-lead collision
PDG: Particle Data Group
PID: Particle IDentification
PS: Proton Synchrotron
PSB: Proton Synchrotron Booster
pQCD: pertubative Quantum Chromo Dynamics
RCU: Read out Control Unit
RHIC: Relativistiv Heavy Ion Collider
ROC: Read Out Chamber
SM: Standard Model
SPD: Silicon Pixel Detector
SPS: Super Proton Synchrotron
STAR: Solenoidal Tracker At RHIC
SUSY: SYper SYmmetric
TeV: Terra electron Volt
TOF: Time Of Flight
TPC: Time Projection Chamber
TRD: Transition Radiation Detector
QED: Quantum Electro Dynamics
QCD: Quantum Chromo Dynamics
QGP: Quark Gloun Plasma
ZIF: Zero Input Force